Quantitative studies of thin foils in the transmission electron microscope.

Rae, D. A.

Award date:
1982

Awarding institution:
University of Bath

QUANTITATIVE STUDIES OF THIN FOILS IN THE TRANSMISSION ELECTRON MICROSCOPE

submitted by

D.A.RAE, B.Sc.

For the degree of Ph.D. of the University of Bath 1982

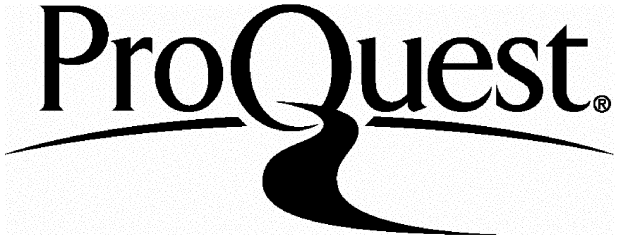

ABSTRACT

Several methods of measuring the thickness of foils used in transmission electron microscopy are described. The first method utilises available crystallographic features, such as slip plane traces, which are present in some materials. It is shown that by tilting the foil to align the defect plane parallel with the electron beam, very accurate values may be obtained for the foil thickness measured in the beam direction. The technique is not subject to errors which may be incurred when the foil surface orientation is not precisely known.

The second technique involves depositing contamination spots on top and bottom surfaces of the foil by electron irradiation. Tilting the foil through a known angle causes separation of the spots in the image plane from which the foil thickness may be calculated. The technique is shown to overestimate true metal thickness due to the presence of surface films and a contaminant aureole surrounding the spots which makes precise location of the spot-substrate interface difficult.

The convergent beam diffraction technique has been investigated and found to be accurate providing certain experimental conditions can be met. The results demonstrate that multiple beam diffraction and

absorption effects can limit the accuracy of the method and that such effects are most pronounced for low order planes.

The above techniques are compared and it is shown that the crystallographic and convergent beam techniques measure the thickness of metal in the beam direction.

A final method utilises x-ray measurements where the x-ray intensity is a function of beam current and foil thickness. The former dependency makes it difficult to correlate x-ray intensities with a particular value of foil thickness. Characteristic and continuum ratios may vary with thickness due to absorption and fluorescence effects and are independent of beam current. The observations indicate that a linear relationship between x-ray path length (and hence absorption) and foil thickness does not always occur. Fluorescence effects are found to be negligible in the 18.8 stainless steel foils studied.

One thickness technique was used to estimate precipitate populations in aluminium alloys aged to peak hardness. It is shown that the habit plane is a function of the foil's silver content and that the apparent precipitate population is a function of foil thickness. A model is given to explain this phenomenon.

ACKNOWLEDGEMENTS

I would like to thank my supervisors, Dr.V.D.Scott and Dr.G.Love for the considerable advice and assistance given throughout this work. I am also indebted to the staff and technicians of the School of Materials Science, especially Mr.H.Perrott and Mr.J.Forsdyke of the Electron Optics section.

I wish to acknowledge Dr.G.Rose and Dr.A.Clifford, AUWE, Portland for their assistance and co-operation in this project.

Finally I wish to thank my wife Gina for her considerable support and encouragement throughout the period of this work.

CONTENTS PAGE

1. INTRODUCTION 1

1.1 The need for accurate foil thickness measurements 1

1.2 Methods available for measuring foil thickness 2

1.2.1 Extinction contour, bend contour and convergent beam diffraction 2

1.2.2 Crystallographic techniques 10

1.2.3 Surface artefact techniques 14

1.2.4 Methods requiring calibration 16

1.3 Summary of available methods 28

1.4 Scope of the investigation 32

2. THE ANALYTICAL TRANSMISSION ELECTRON MICROSCOPE 34

2.1 Transmission electron microscopy (TEM) 35

2.1.1 Resolution 35

2.1.2 Depth of field and focus 38

2.1.3 Diffraction 39

2.1.4 Image production and contrast 41

2.2 Scanning transmission electron microscopy (STEM) and Secondary electron microscopy (SEM) 44

2.3 The energy dispersive spectrometer 46

3. THE USE OF CRYSTALLOGRAPHIC FEATURES IN DETERMINING THICKNESS 49

3.1 Preparation of specimens for TEM examination 49

3.2 Crystallographic analysis 51

3.3 Fault tilting method 56

4. THE CONTAMINATION SPOT METHOD 61

4.1 Preparation of specimens 61

4.1.1 Thin foils 61

4.1.2 Thin evaporated films 61

4.1.2.1 Production 61

4.1.2.2 Measurement of thickness 63

4.2 Effect of deposition conditions on contamination spot morphology 68

4.2.1 Specimen current 69

4.2.2 Deposition time 71

4.3 The comparison of the contamination spot technique and tilting fault method 72

4.3.1 Contamination spot versus tilted fault in stainless steel 72

4.3.2 Influence of pre-existing films 74

4.3.3 Surface film growth in the TEM 75

4.4 Analysis of uncertainties in the contamination spot method 77

4.4.1 Effect of spot profile 79

4.4.2 Effect of spot size 80

4.4.3 Effect of different foil materials 81

4.5 Discussion 83

5. CONVERGENT BEAM DIFFRACTION 86

5.1 Preparation of specimens 86

5.2 Convergent beam diffraction measurements 86

5.2.1 Production of convergent beam diffraction patterns 86

5.2.2 Analysis of convergent beam diffraction patterns and treatment of results 89

5.2.3 Discussion 92

5.3 Comparison of the convergent beam technique with other methods 98

5.3.1 Contamination spot method 98

5.3.2 Tilting fault technique 99

6. X-RAY MEASUREMENTS 101

6.1 X-ray theory relevant to the present study 101

6.1.1 X-ray generation 101

6.1.2 Depth distributuion of generated x-rays 104

6.1.3 Intensity of generated x-rays in a thin film 105

6.1.4 X-ray emission and correction procedures 106

6.1.5 X-ray detection 110

6.2 Preparation of specimens 110

6.3 Production and processing of x-ray data 111

6.4 Reproducibility of x-ray measurements 116

6.4.1 Variable analysis positions 116

6.4.2 Variable analysis conditions 117

6.5 Effect of foil thickness on the x-ray yield from a copper specimen 118

6.6 Absorption effects in copper and their potential use in establishing foil thickness 120

6.7 Fluorescence effects in thin stainless steel foils 123

6.8 Surface film effects in a Cu 4%-Al alloy 125

7. THE APPLICATION OF THE CONTAMINATION SPOT METHOD TO PRECIPITATE MEASUREMENTS IN Al-ALLOYS 128

7.1 Materials, specimen preparation and examination 128

7.2 Examination of an Al-alloy with a high Ag:Cu ratio 129

8. CONCLUSIONS AND FURTHER WORK 133

REFERENCES

1. INTRODUCTION

1.1 The need for accurate foil thickness measurements

It has long been realised by metallurgists and materials scientists that the properties of materials are dependent on structure. This in turn is largely determined by material composition and production history. To facilitate the design of new materials and to optimise the properties of those already in existence requires an insight into these relationships. An understanding of both composition and microstructure at the highest possible degree of resolution is necessary for the confident interpretation of structure related properties.

The modern transmission electron microscope (TEM) provides the facility for both physical and, with certain attachments, chemical analysis with very high resolution. The state of the science is such that thin films from a great variety of materials can be prepared for examination and observed at magnifications capable of resolving features on an atomic scale. Such capabilities have been utilised in many areas of research with this proliferation continuing to expand ever more rapidly.

The growth of TEM studies has been accompanied by an increasing desire and need to provide fully quantitative information about materials structure and composition. However, the image formed by a TEM is a magnified two dimensional projection of the object. For a more complete knowledge of physical structure and specimen composition the local foil thickness requires accurate determination. The very thin and tapering nature of most TEM foils

poses many problems to the elucidation of this parameter.

A variety of techniques have been adopted by various workers for measuring the thickness of a thin foil, some methods being more accurate and flexible in use than others. Many use different physical phenomena as a basis for their measurements and therefore it is possible that not all measure precisely the same parameter. The choice of method may therefore be important as the interpretation of results may depend on which measurement is defined as thickness.

In the next part of this section the current methods available for determining foil thickness are critically reviewed, the aim being to select those techniques that are worthy of further study. The main criteria for the selection of a method are that it be (i) accurate (ii) flexible, i.e. in situ measurements can be performed in any region of interest, and (iii) practicable, i.e. the technique should be capable of being applied to a wide range of materials and materials problems.

The methods studied will possess the above mentioned qualities in various amounts and the relative merits of each technique will be discussed prior to its selection (or rejection) for further study.

1.2 Methods available for measuring foil thickness

1.2.1 Extinction contour, bend contour and convergent beam methods

As an electron beam propagates through a crystalline specimen its amplitude varies both with depth and with

the angle which the beam makes with the specimen's atomic planes. Such a variation can be monitored and related to the thickness of the specimen.

For a specimen illuminated by a parallel beam of electrons, the amplitude variation with depth produces a series of light and dark fringes corresponding to different foil thicknesses. If a small area of specimen is illuminated by a convergent electron beam, light and dark fringes may be observed in the diffracted discs, these too being a function of the local specimen thickness. Both instances are best explained by reference to the two beam dynamical theory of diffraction for a perfect crystal.

The theory describes the amplitudes of the transmitted and diffracted beams, ϕ_o and ϕ_g respectively, in an element dz, at a depth z, in a small column of material present in a thin foil of thickness t, see Fig.1. It allows that the diffracted beam may be high in intensity compared with the transmitted beam, that electrons may be rediffracted back into the transmitted beam and that absorption of electrons within the specimen may occur. Further stipulations, known collectively as the column approximation, are also made which assume that:

A. the column is wide enough to contain both the transmitted and diffracted rays but is narrower than the final image;

B. there is no loss or gain between those waves within the column and the surrounding material;

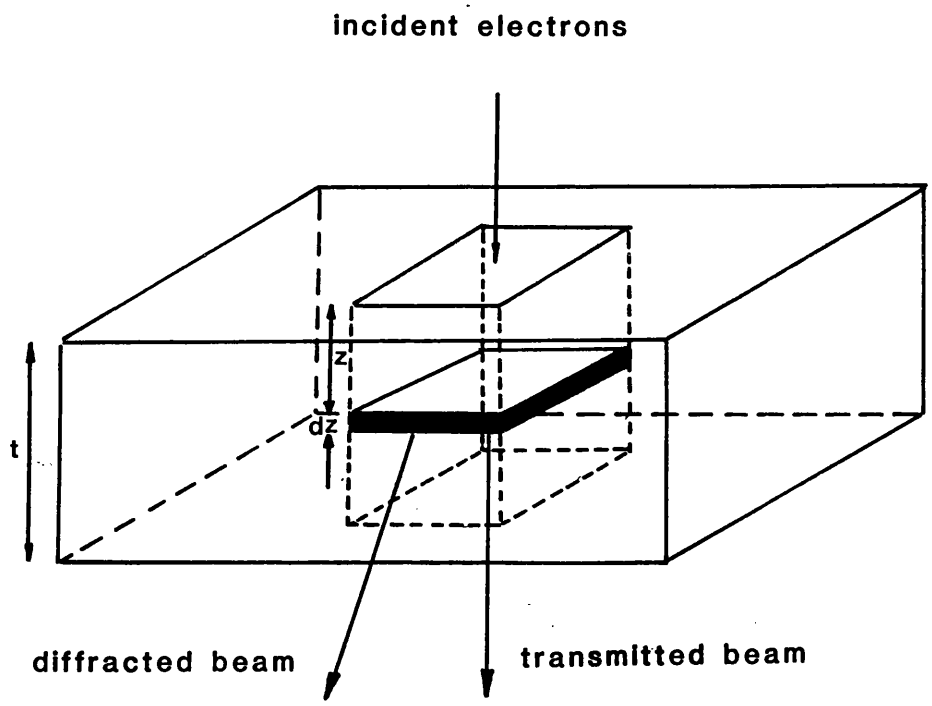

Fig. 1 The column approximation used in the two beam dynamical theory.

C. any defects present may cause distortion down, but not across the column;

D. only plane waves exist in the column;

E. only one diffracted beam exists i.e. there are perfect 2-beam conditions.

As the transmitted wave propagates through the specimen its amplitude, ϕ_o, will be depleted while that of the diffracted wave, ϕ_g, increases correspondingly. The changes are described in the equations given by Darwin, Howie and Whelan (Hirsch, Howie, Nicholson, Pashley and Whelan, 1965).

Viz:

$$\frac{d\phi_o}{dz} = \frac{i\pi}{\xi_o}\phi_o + \frac{i\pi}{\xi_g}\phi_g \exp(2\pi isz) \qquad 1.1(a)$$

$$\frac{d\phi_g}{dz} = \frac{i\pi}{\xi_o}\phi_o \exp(-2\pi isz) + \frac{i\pi\phi_g}{\xi_g} \qquad 1.1(b)$$

where s is the deviation from the exact Bragg position and ξ_o and ξ_g are constants for the material. ξ_g is a critical distance in the perfect crystal between points where the transmitted intensity is a minimum and is known as the extinction distance. The amplitudes of the waves will also vary as a result of two absorption processes within the specimen. Uniform absorption leads to an overall decrease in intensity with depth while anomalous absorption involves selective absorption of some electrons and is due to the differential properties of the Bloch waves associated with diffraction (Hirsch et al p.215). Absorption is allowed for by introducing imaginary extinction distance components viz:

$$\frac{1}{\xi_g} \rightarrow \frac{1}{\xi_g} + \frac{i}{\xi'_g} \qquad 1.2(a)$$

$$\frac{1}{\xi_o} \rightarrow \frac{1}{\xi_o} + \frac{i}{\xi'_o} \qquad 1.2(b)$$

The term ξ_o/ξ'_o is the uniform absorption parameter and influences the whole background intensity while ξ_g/ξ'_g is the anomalous absorption parameter, responsible for many of the detailed features of diffraction contrast images.

Integration of 1.1(a) and (b) leads to a relationship for the diffracted and transmitted intensities viz:

$$|\phi_g|^2 = \frac{\pi^2}{\xi_g^2} \frac{\sin^2(\pi t s_{eff})}{(\pi s_{eff})^2} \qquad 1.3(a)$$

and $$|\phi_o|^2 = (1 - |\phi_g|^2) \qquad 1.3(b)$$

where s_{eff}, the effective deviation parameter = $(s^2+\xi_g^{-2})^{\frac{1}{2}}$.

It can be seen from equation 1.3 that the intensity of both rays is a function of t and s. For a parallel beam of electrons incident on a tapering foil, light and dark fringes parallel to the foil edge will be observed. If the exact Bragg orientation is obtained for the two beam conditions (s=0), the dark fringes will occur for t equal to $\frac{1}{2}\xi_g$, $1\frac{1}{2}\xi_g$, $2\frac{1}{2}\xi_g$ etc, see Fig. 2. This is the basis of the extinction thickness fringe method for determining foil thickness. Tables of extinction distances are available, which have been calculated from theory (Hirsch et al p102). The method is accurate when only two beams are operating and s = 0 i.e. no deviation from the Bragg angle. The precision is limited only by the accuracy

Fig. 2

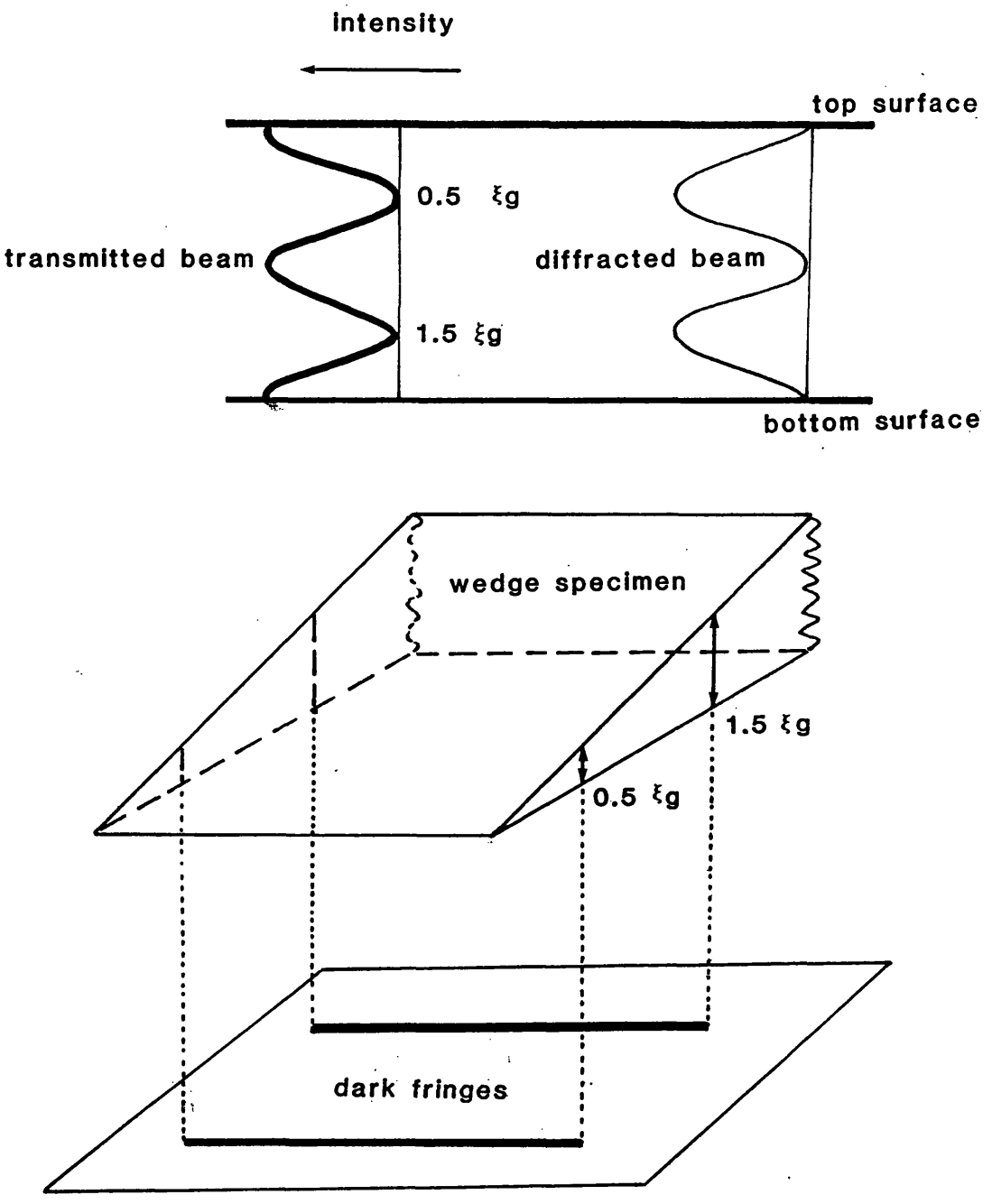

Fig. 2 Electron intensity distribution for a crystal at the exact Bragg orientation

attached to the extinction distance values ($\approx 5\%$). When these ideal diffraction conditions are absent much larger errors can be introduced. Small deviations from the $s = 0$ position result in a lower value of extinction distance according to

$$\xi_{g\ effective} = \xi_g/(1 + s^2\xi_g)^{\frac{1}{2}} \qquad 1.4$$

This will always result in an overestimate of foil thickness which may be as high as 2 or 3 times the actual value. Careful setting up on the diffraction conditions can largely eliminate this error but another error is almost impossible to remove. In reality, rigid 2-beam conditions are very difficult to achieve. Almost inevitably some extra systematic reflections occur. This reduces the value of $\xi_{g_{effective}}$ leading to further overestimations in foil thickness. Other limitations of the method arise from the anomalous absorption effect. This damps out the fringes in thicker foil regions, effectively reducing the upper thickness limit to $\approx 5\xi_g$ and therefore restricting its use to thin areas near the edge of tapering foils.

The restrictions of the extinction contour method severely limit its applications. The convergent beam diffraction method (CBD) utilises the same diffraction theory to provide foil thickness values but overcomes many of the difficulties and restrictions encountered in the thickness contour technique.

Equation 1.3 shows that if s is constant the intensity of the transmitted and diffracted rays will

vary with t, (the basis of the extinction contour method) and conversely for a given value of t, variation of the deviation parameter s will cause the intensity to oscillate. This relationship is described graphically in Fig. 3(a). Two points are worth noting. The intensity is plotted as a function of $s\xi_g$, this being because ξ_g effective is itself a function of s. Secondly the transmitted ray's intensity oscillation is asymmetric about s = 0 while that of the diffracted ray is symmetric. In the two-beam case anomalous absorption affects only the transmitted beam resulting in anomalous absorption for negative s values and anomalous transmission for positive s values. For a convergent beam impinging on a specimen aligned for two-beam diffraction, a range of values of 's' is produced. This is shown in Fig. 3(b), the Ewald Sphere construction for such a situation. The central diffracted ray, which is at the exact Bragg angle, has a deviation parameter, s, of zero and the intensity of the diffracted beam is a maximum. The deviation parameter becomes increasingly negative to one side of this position and increasingly positive on the other side. This results in an intensity oscillation governed by equation 1.3 and similar in profile to that shown in Fig. 3(a).

Equation 1.3 relates $|\phi_g|^2$ to t in a way which is easy to appreciate but difficult to use in practice. By differentiating the equation with respect to the deviation parameter MacGillavry (1940) obtained essentially:

$$(s_i^2 + \frac{1}{\xi_g^2})t^2 = n_i^2 \qquad 1.5$$

Fig. 3

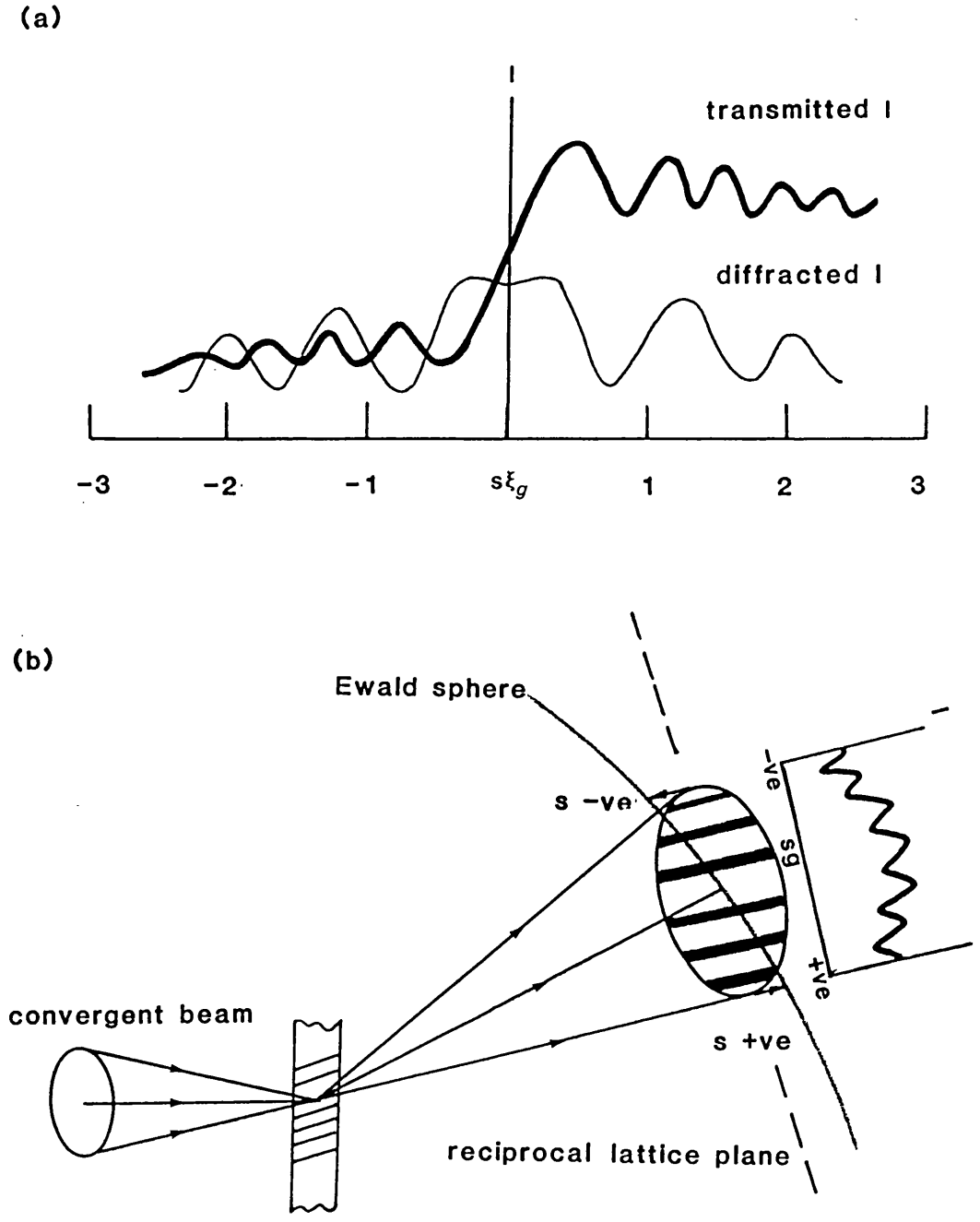

Fig. 3 (a) Electron intensity variation with deviation parameter and (b) the effect of such a variation on the profile of an expanded diffraction spot.

where s_i is the deviation parameter of the ith minimum and n_i is an integer. By plotting a graph of s_i^2 against n_i^2, Ackermann (1948) was able to determine the specimen thickness and extinction distance of crystalline specimens from the curve gradient and ordinate intercept respectively. These workers performed their experiments in special diffraction cameras and therefore did not have the advantage of high magnification image formation available in the TEM. In an analogous situation, Siems, Delavignette and Amelinckx (1962) determined thicknesses from the contours displayed by a uniformly bent foil. In this instance the beam of electrons was collimated and the uniformly bent foil provided the continuous range of incident angles. A similarly derived equation was used to determine 't' from the subsidiary bend contour positions, this being:

$$t = \sqrt{2}\ (s_1^2 + s_3^2 - 2s_2^2)^{\frac{1}{2}} \qquad 1.6$$

where s_1, s_2 and s_3 are the deviation parameters for three successive minima. They also showed that the maxima could be used in the analysis. Bell and Thomas (1969), in contrast to previous workers who used specially designed diffraction cameras, caused a TEM to behave in a convergent beam mode by fully focussing the condenser lens system so that the diffracted spots became magnified images of the condenser aperture. They then used equation 1.6 to calculate the thickness values.

Goodman and Lehmpfuhl (1967), and Cockayne, Goodman, Mills and Moodie (1967), with the aid of specialised diffraction cameras determined the thickness of flat MgO

crystals by comparing the intensity profiles of the diffracted discs with computed theoretical curves.

All the methods mentioned so far have disadvantages when considered for the in situ measurement of foil thickness. Electron diffraction cameras, without high magnification imaging facilities, are confined to measuring the thickness of flat, parallel sided crystals. The method of Siems et al requires specimens to be uniformly bent, an ideal difficult to achieve in practice, while it also suffers from anomalous absorption effects in thicker regions, as discussed by Kelly, Jostsons Blake and Napier (1975a). Equation 1.6, used by Siems et al and some later workers, is subject to error for thick specimens. With many parallel fringes appearing in the diffracted discs of such specimens, the minima corresponding to s_1, s_2 and s_3 can become tightly bunched and difficult to measure. Kelly et al (1975a) describe the errors associated with the other convergent beam methods. Ackermans approach, for instance, is regarded as being subject to small absorption errors when measuring thick regions. This, it is argued, is because Ackermans thickness values are derived from the gradients of s_i^2 versus n_i^2 plots. These plots are greatly influenced by the deviation parameter value of the first minima and as will be seen later, the s_1 values are most prone to measurement error. They are also increased in value for strongly absorbing crystals.

Kelly et al (1975a) make use of the highly convergent probe available in a modern scanning transmission electron

microscope (STEM). The resultant fringe patterns are analysed graphically using a rearranged form of McGillavry's equation, which may be written for convenience as

$$\left(\frac{s_i}{n_i}\right)^2 = -\left(\frac{1}{\xi_g^2}\right)\left(\frac{1}{n_i^2}\right) + \frac{1}{t^2} \qquad 1.7$$

This when correctly plotted as $\left(\frac{s_i}{n_i}\right)^2$ versus $\left(\frac{1}{n^2}\right)$ is linear with a gradient of $-\left(\frac{1}{\xi_g^2}\right)$ and an intercept on the $\left(\frac{s_i}{n_i}\right)^2$ axis equal in magnitude to $\frac{1}{t^2}$.

1.2.2 Crystallographic techniques

Defects present in a crystalline solid may be used to determine its specimen thickness provided that, (i) they are visible, (ii) they intersect top and bottom surface of the foil and (iii) their precise orientation can be determined. Among the many different features used in such studies have been slip traces, (Vigeholm and Lindbo 1969) stacking faults (Hall and Vander Sande 1975) twin and grain boundaries (Thompson & Chen 1979), dislocations (Formby 1966) and overaged precipitates (Von Heimendahl 1964). The ideal geometrical situation is shown schematically in Fig. 4. The thickness of the specimen is related to the crystallographic feature by the equation:

$$t = W.\cot\theta \qquad 1.8$$

The projected width of the defect, W, is easily obtained from an electron micrograph of the foil.

Fig. 4

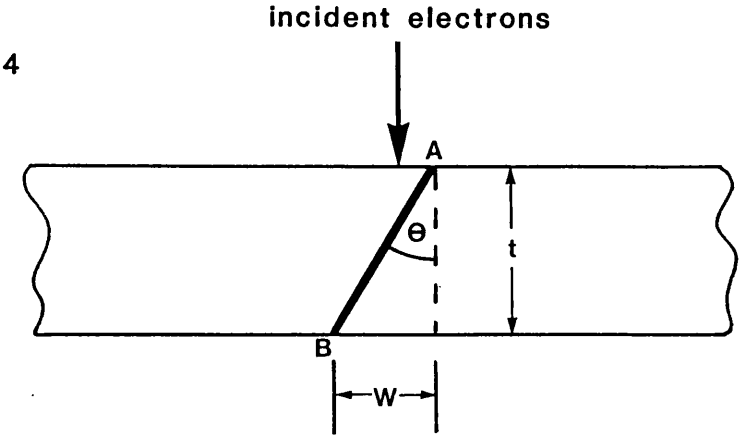

$t = W \cot \Theta$

Fig. 5

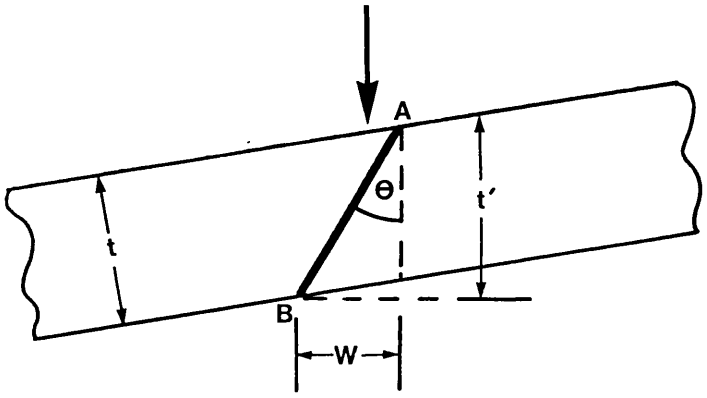

$t' = W \cot \Theta$

Fig. 4 Ideal foil and fault geometry for thickness determination.

Fig. 5 effect of foil surface ambiguity on the thickness determination.

The angle θ in equation 1.8 may be determined by one of two general methods. The first technique requires prior knowledge of the defect habit plane type. Stacking faults and slip traces, for example are known to occupy {111} planes in face-centred-cubic metals. The precise orientation of the specific habit plane can then be determined from a diffraction pattern of the relevant area. The second general technique involves recording the projected width of a defect at various tilt angles. The relationship between these two parameters can then be used to determine the defect orientation. In the review that follows, the various techniques described will fall into one of these two broad categories.

A problem common to both techniques concerns the errors that arise as a result of the beam and foil normal not being parallel. This can occur as a result of intentional specimen tilting or may be due to thin regions of the foil bending during preparation or examination. The latter is the more serious as the magnitude of the effect, or even its very presence, may remain unsuspected. Figure 5 shows that errors in foil thickness arising from such uncertainties can be appreciable.

Hirsch et al (1965) predicted that errors of up to 50% could occur in thickness calculations if the foil was inclined only 15^{o} from its ideal position. It was proposed by these workers that the angle θ in equation 1.6 be replaced by a new quantity θ' given by

$$\theta' = \theta + \cos^{-1}\left[\frac{\cos\psi}{(1-\cos^2\omega\sin^2\psi)^2}\right] \qquad 1.9$$

where ψ is the angle of tilt of the foil relative to its ideal position perpendicular to the beam and ω is the angle between the tilt axis and the projected length of the object in study. Kelly (1975b) argues that equation 1.9 probably underestimates the potential errors. His alternative, in the same notation as before, reads:

$$t = \dot{\omega}\{\cos\psi\,[\tan^2\theta - \cos^2\omega\,\tan^2\psi]^{\frac{1}{2}} - \sin\psi\,\sin\omega\} \quad 1.10$$

Even larger errors (greater than a factor 2) are predicted by this equation for cases where θ is small. For steeply inclined traces where θ is large the errors are much smaller.

It can be seen that a knowledge of the angle ψ would be useful in order to reduce potential errors, but this is difficult to determine in practice. Hirsch for instance mentions that a single crystal film grown epitaxially will have a known crystal plane parallel to its surface, a situation that does not commonly arise however. Otte, Dash and Schaake (1964) present two methods for uniquely defining the foil inclination. One is based on the presence, in a thin foil containing stacking faults, of rel spikes in the diffraction pattern due both to the foil 'thinness' and also the stacking faults. For a tilted foil these spikes will be inclined to the image plane and by a long and tedious process the inclination of the rel spikes and hence the foil surface can be determined.

The other method mentioned in the paper requires the presence of three slip traces from different planes to

uniquely define the surface orientation. Similar techniques relying on the presence of intersecting slip traces have been outlined by other workers, e.g. Skalicky and Degischer (1968), Drazin and Otte (1963), Crocker and Bevis (1964), Kawanishi et al (1973) & Von Heimendahl (1964.) Crocker and Bevis point out that to obtain a unique solution for t at least three and somtimes four intersecting traces must be visible in the image.

The experimental requirements of the above techniques make then impracticable in most studies. Vingsbo (1970) suggested that stereo pairs of defect photographs taken at two different tilt angles would remove the necessity for determining the exact defect orientation with respect to the foil surface. Figure 6 shows how the angle between the defect and the foil surface can be eliminated. However the orientation of the foil surface with respect to the beam remains ambiguous and the resultant uncertainty in thickness may therefore be large. Vingsbo's treatment neglects possible errors from this source but still finds that the uncertainty in thickness may be as high as 1000Å when using this method. The use of the technique is therefore extremely limited. To minimise thickness errors arising from the non incidence of foil normal and electron beam only steeply inclined defects should be used but one of the advantages claimed for the method is that fault orientation need not be determined!

Thompson and Chen (1979) also devised a method of determining t which required tilting a sample through known angles. In this method a defect, intersecting top

Fig. 6

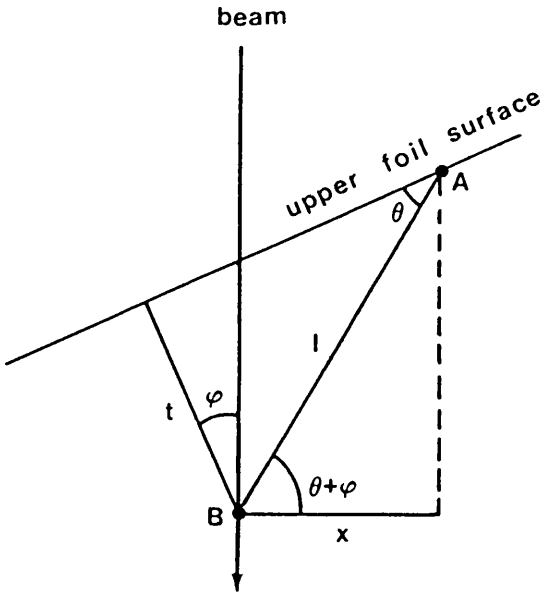

Figure 6. (after Vingsbo 1970). Section of a specimen

t = foil thickness
l = length of fault AB which itersects top and bottom surfaces of foil @ A and B
x = projection of fault length l onto image plane
θ = angle between AB and foil surface
φ = specimen tilt angle

We have $t = l. \sin\theta$ and $x = x(\varphi) = l. \cos(\theta + \varphi)$

Eliminating l gives $t(\varphi) = \dfrac{x \sin\theta}{\cos(\theta+\varphi)}$

By finding two angles φ_1 and φ_2 of good contrast conditions, giving the projections x_1 and x_2, θ can be eliminated and

$$t = \frac{x_1 \cos\varphi_2 - x_2 \cos\varphi_1}{\sin(\varphi_2 - \varphi_1)} \qquad 1.11$$

and bottom surfaces of the foil, was positioned such that its trace lay perpendicular to the tilt axis. The projected width of the defect, was plotted as a function of tilt angle. The result obtained by the authors was a linear relationship; the intercepts on the various axes giving the inclination angle of the fault and its width at zero tilt. This method, however, takes no account of the possible non incidence of the foil normal and beam direction, with the potentially large errors that could occur as a result.

1.2.3 Surface artefact techniques

It was shown in the previous section that crystallographic features intersecting top and bottom surfaces of a foil could be used to obtain thickness values; the image width of the fault being the projected distance between the points of intersection of the defect and the specimen surfaces. An alternative approach is to produce artefacts on top and bottom surfaces and relate the projected distance between these objects to thickness.

Von Heimendahl (1973) used tiny latex spheres (diameter 234 ± 2.6nm) as his surface artefacts. These were applied to the foil surface by dipping the specimen into an alcoholic suspension of the spheres. For latex spheres on either side of a foil, a tilt in one direction causes them to apparently converge whilst tilting in the opposite sense will result in further separation in the image plane. Figure 7(a) and (b) show the changing view resulting from such a tilt, as it

Fig. 7

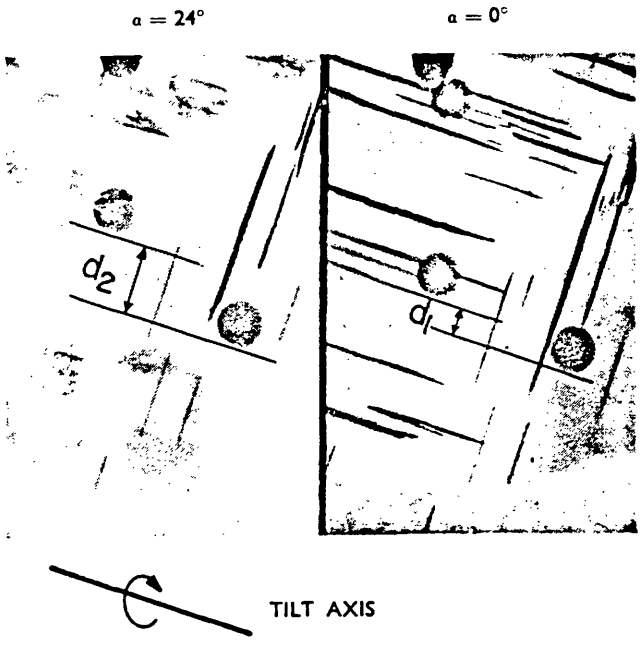

(a) Electrolytically thinned specimen of an Al-4%Cu alloy with applied latex balls. t = 324nm ± 4%. ×25,600.

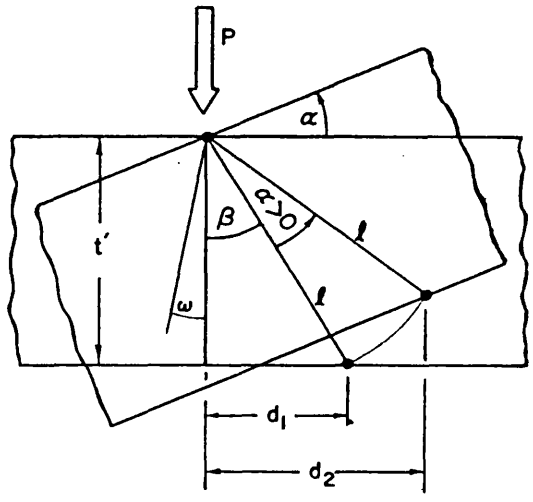

(b) Cross section through a hypothetical foil of thickness t' (= real foil thickness t + diameter D of latex balls). Tilt axis perpendicular to drawing plane. α, tilt angle; l, projection of ball distance upon drawing plane; d_1 and d_2, projections of l on the plate before resp. after tilt; P, primary electron beam; ω, see text.

Fig. 7 Latex ball technique, after Von Heimendahl (1973).

appears on the micrograph and also in cross-section. The thickness of the foil in such a case is given by:

$$t = \frac{d_2 - d_1 \cos\alpha}{\sin\alpha} - D \qquad 1.12(a)$$

where α is the angle tilted through and D is the latex sphere diameter (Fig. 7b). Tilting in the opposite sense causes the projected width to become smaller and is denoted as d_3 after tilting for better distinction. If again the tilt is denoted as α we have:

$$t = \frac{d_1 \cos\alpha - d_3}{\sin\alpha} - D \qquad 1.12(b)$$

The author assumes that the foil and beam are perpendicular in the first instance and that no unintentional tilt due to foil buckling is present. Incorporating a 10^{o} uncertainty into the foil inclination results in errors of up to 28.6% for a thin (0.3μ) foil when the angle β is 40^{o}. This angle is analogous to the angle of inclination of crystalline defects in Section 1.2.2, and just as erors were smaller for steeply inclined traces, here too the errors are found to be minimised when β is small. The precision of the method can be improved by taking readings at several tilt angles, but the potential errors in accuracy remain.

Lorimer, Cliff and Clark (1976) devised a novel way of producing artefacts within the electron microscope. They found that when focussing a fine electron probe upon a specimen a needle of contaminant rapidly grew on the top and bottom surfaces in the immediate vicinity of the

beam. Subsequent tilting of the specimen produced separation of the two 'needles' on the viewing screen. This is shown schematically in Fig. 8. From the image of the separated spots a thickness value could be calculated. The advantage of the contamination spot method, just described, is its potential for in-situ measurement of foil thickness at any point of interest on the foil. Another point in its favour is that the parameter measured is the thickness of the foil in the beam direction. This is the measurement required for many materials investigations, precipitate counting for example. Any mis-alignment of the foil normal and beam direction does not affect this parameter.

1.2.4 Methods requiring calibration

The methods in the previous sections can all be used independently to provide values of foil thickness. Other methods require calibration prior to their use. These non absolute techniques measure a parameter which varies proportionately with thickness, the constant of proportionality being determined experimentally.

Electron Backscattering

One such technique is the electron backscattering technique, thoroughly investigated by Niedrig (1978). When electrons impinge on a material a variety of interactions occur, Fig. 9. The incident electron may be elastically scattered with no subsequent loss of energy; inelastically scattered causing the emission of

Fig. 8

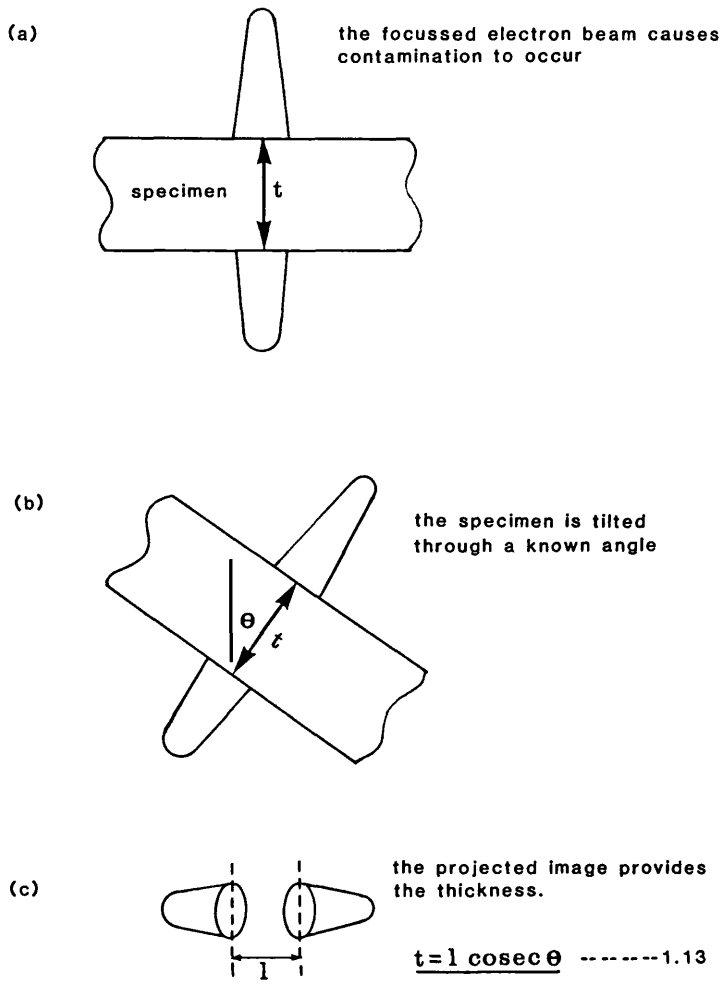

Fig. 8 The contamination spot technique.

Fig. 9

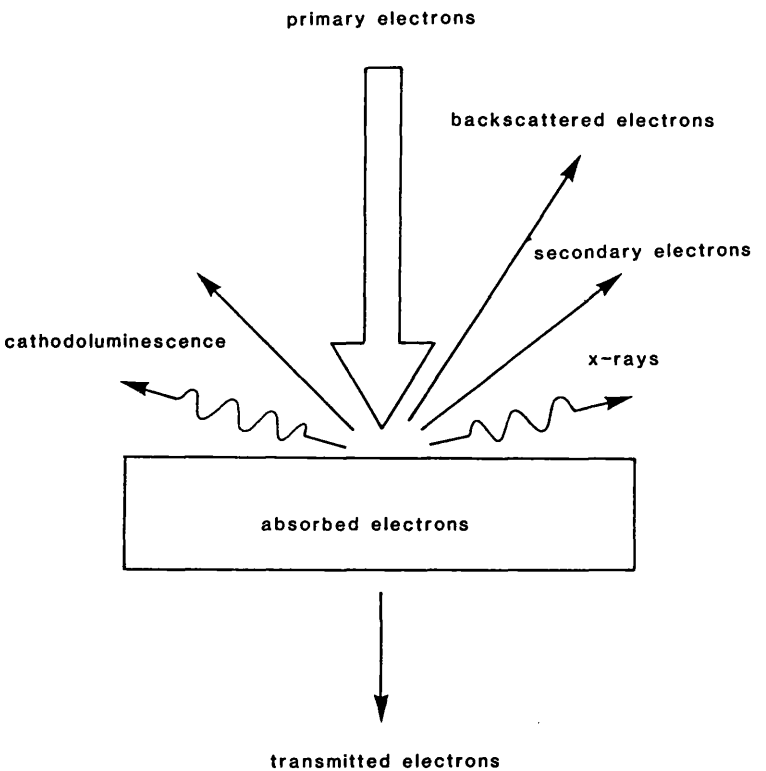

Fig. 9 Phenomena associated with electron-specimen interaction.

another electron and losing energy in the process, or it may undergo a combination of these processes.

The inelastic collisions leave atoms in an excited state. The subsequent return to their ground state is accompanied by the emission of x-rays, Auger electrons or light. The electrons scattered in such a manner are usually deviated through a small angle. In contrast some electrons are elastically scattered by the Coulomb potential of the scattering nucleus. The angle through which these electrons are deviated may be large enough for them to re-emerge from the specimen surface. They are then referred to as reflected or backscattered electrons.

Niedrig defines the backscattering ratio from a thin film as

$$\eta = I_r/I_o \qquad 1.14$$

with I_r being the intensity of the backscattered electrons and I_o the incident intensity. Neidrig found that η initially increased in an approximately linear mode with the thickness of evaporated films, this being measured by an interferometry or quartz crystal oscillatory technique. It reached a saturation value at a thickness which was approximately equal to half the range of the electrons in the solid ($\approx$600nm for Al at 20 keV and $\approx$ 75nm for Au at 20keV). The initial increase and the saturation value of η depends on the atomic number of the film material. The saturation value which is always less than 1, is found to be identical to bulk material

backscattering ratios.

The shape of the backscatter curve, shown for Al and Au in Fig. 10, led Niedrig to assume a single scattering process. However equations based on this assumption gave theoretical values of η which underestimated the experimentally obtained values by a factor of two to three times. Therefore multiple scattering must be taken into account but as Niedrig states, a theory for multiple large angle scattering does not at present exist.

In his experimental work Niedrig found that the backscattering ratio was independent of the probe size and was relatively insensitive to variations of crystal size, crystal orientation and crystal temperature. The incident and backscattered electron intensities were measured using Faraday cages. The construction of the cartridge containing these cages is given by Kindt and Niedrig (1974).

Electron Absorption

Medved and Poppa (1962) and later Joy and Maher (1975) used a technique based on Lambert's law for absorption viz

$$I = I_o \, e^{-\mu t} \qquad 1.15$$

where I_o and I are the incident and transmitted electron beam intensities, μ is the mass absorption coefficient of the specimen and t its thickness. Mass absorption coefficients were not available for all materials and hence a calibration was performed using films which had previously been measured by multiple beam interferometry. A Faraday cage within the TEM measured the intensity

(current) of the incident electrons. The specimen was then inserted into the path of the electron beam and the transmitted current measured. The mass absorption coefficient for the material could then be found from the Lambert equation and used in any future work to determine thickness values. The dissimilarity in density of evaporated and bulk thinned films could introduce errors into the experimentally determined absorption coefficients. Additionally, anomalous absorption effects may cause a marked variation of the transmitted intensity with specimen orientation. Joy and Maher advocate using set diffraction conditions during the experiment, measuring the intensity of one diffracted ray only. This would improve the reproducibility of results by standardising the uncertain effects of anomalous absorption and transmission.

The above effects could also be reduced by employing highly convergent electron probes but even in this case the presence of any diffraction contrast would have to be avoided. The rapid build up of contamination in a convergent beam situation could lead to increased electron scattering, reflecting itself in a time dependent value of I and hence thickness.

Energy loss Spectroscopy

The Coulomb interaction between incident electrons and those of the crystal is long range. Thus in addition to suffering inelastic collisions with individual electrons in the crystal, the incident electron can cause an excitation of the whole valence electron cloud.

These 'plasma oscillations' or plasmons have a characteristic excitation energy which is usually in the 3eV to 30eV range. Evidence that plasmons are excited is provided by the energy loss spectra of many materials which peak at definite values of frequency i.e. 0, hw, 2hw etc., where h is Planks constant and w is the plasmon frequency. The probability for n separate inelastic collisions involving such a process is given by a Poisson distribution (Roussouw and Whelan1978)

$$P_n = \frac{1}{n!} \left(\frac{t_e}{\lambda_p}\right)^n \exp \left(\frac{t_e}{\lambda_p}\right) \qquad 1.16$$

where t_e is the distance travelled by the electron in passing through the foil, effectively the foil thickness, and λ_p is the mean free path length for plasmon excitation.

Rossouw and Whelan (1978) investigated the relationship between the plasmon excitation and thickness for foils of Aluminium Nitride and Graphite. They used a specialised energy selecting electron microscope fitted with a detector capable of resolving energy spectra. The analysis yielded accurate mean free path lengths which subsequently enabled local thickness determinations to be made.

The areas under the loss peak, I_1, and the zero loss peak, I_o, are related to t_e by

$$t_e = \lambda_p(\alpha,\Delta E) \frac{I_1}{I_o} \qquad 1.17$$

where λ_p is a function of the collection semi angle (α)

of the electron spectrometer and the energy window ΔE. The path length λ_p was calculated by Rossouw and Whelan using both a simple plasmon theory given by Howie (1963) and Egerton (1975) and a theory corrected for relativity, Hirsch and Humphreys (1968).

For a specific experimental apparatus the above equation is more conveniently expressed as

$$t_e = c(\alpha, E_1) \frac{h_1}{h_o} \qquad 1.18$$

where c is a calibration constant and h_1/h_o the relative height of the loss peak and zero loss peak. The procedure was calibrated by reference to an absolute technique, namely the bend extinction contour method referred to in section 1.2.1. The energy loss method is, unfortunately, not available to most TEM users, the specialised hardware employed not being in general use.

X-ray techniques

Included in the number of interactions that occur when energetic electrons impinge on a solid target is the generation and emission of x-rays. The x-ray spectrum of all materials consists of a number of characteristic lines superimposed on a background or continuum, see Fig. 11. The characteristic lines are a function of the elements present and their position on the energy spectrum is fixed, regardless of the chemical nature or bonding of each element. These x-rays are produced by the inner shell atomic excitations which are a result of inelastic collisions between the incident electrons and atomic nuclei. The background radiation is produced by the

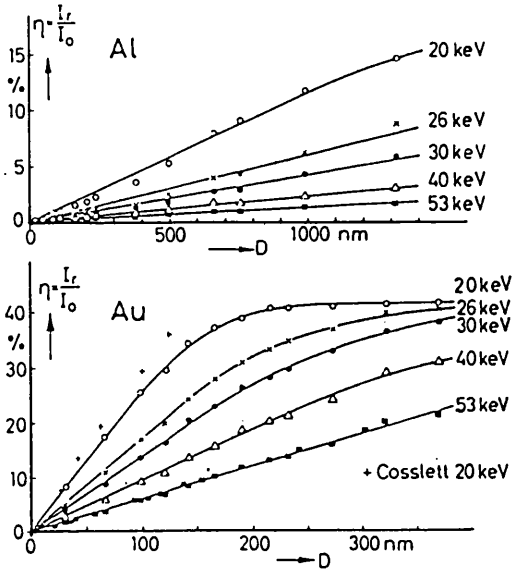

Experimental values of the backscattering ratio versus film thickness for aluminium and gold. Normal incidence. Parameter: energy of the incident electrons

Fig. 10 Electron backscattering curves for aluminium and gold,(after Niedrig 1978).

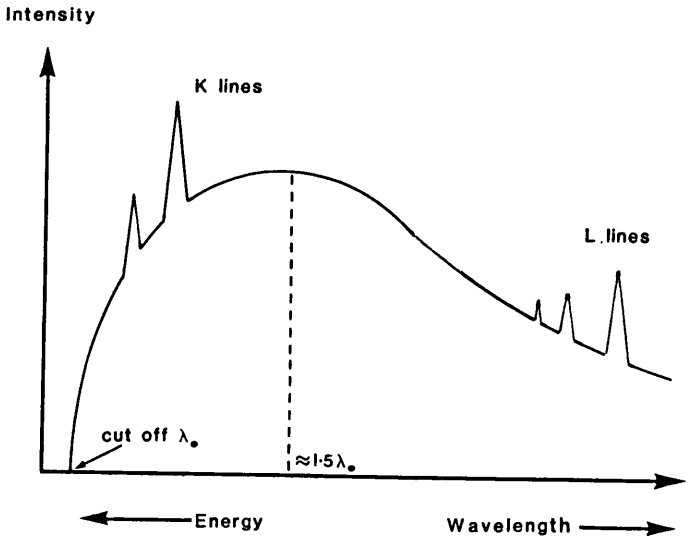

Fig. 11 Typical x-ray spectrum (schematic).

deceleration that accompanies the inelastic interaction between incident electrons and the electron cloud of the target. The nature of these phenomena is dealt with more fully in section 6 which also includes a full treatment of the many interactions which x-rays themselves may undergo before being counted.

The distribution of generated x-rays in a sample is partly limited by the penetrating power of the incident electrons. In a bulk sample, where no electrons are transmitted, the intensity of generated x-rays is insensitive to dimensional changes in the target. The collected x-rays are mainly a function of the target composition, with some correction factors being required to account for the efficiency of x-ray production, attenuation of x-rays in the target and detector, and the efficiency of detection of the various x-rays.

If a thin target is irradiated with electrons a large proportion of them may be transmitted. These transmitted electrons are 'dead' in the sense that they may no longer excite x-rays from the target. The likelihood of an x-ray being generated depends on the presence of an energetic electron. Thus in a very thin sample, where the mean path length of electrons is small, the probability of an x-ray generation is also small. As the thickness of the sample is increased so too are the number of generated x-rays. A saturation level is reached when bulk dimensions are approached. It can therefore be appreciated that within a 'thin film limit' the x-radiation intensity will be a function of thickness.

As electrons and x-rays are scattered less in thin films the 'spatial resolution' of thin film x-ray analysis exceeds that of bulk specimens. This means that much finer particles can be analysed when using thin films.

The variation of the spectra with thickness is an inconvenience to analysts who wish to obtain information on specimen composition. However these shortcomings may be advantageous in other respects, the relationship between x-ray spectra and target thickness being itself potentially useful as a foil thickness measuring device.

Most of the thin film work to data has been done from the analytical standpoint, the idea being to examine the effects of thickness on analytical data and to correct for, or negate such effects when they occur.

The intensity of individual characteristic lines is a function of the amount of each element present in a sample. It is also a function of beam current, the more electrons striking the target the greater the number of excitations and x-ray emissions. Cliff & Lorimer (1972), in an attempt to eliminate current and thickness variables, introduced the concept of characteristic ratios. For a thin film containing elements A and B, the relative concentrations could be found from

$$C_A/C_B = K_{AB}\ I_A/I_B \qquad 1.19$$

The constant K_{AB} is said to be independent of beam current, specimen thickness and composition, and as such could be experimentally determined from materials of similar known composition. I_A and I_B are the simultaneously measured intensities of A and B. The thickness independence of K_{AB} was based on the assumptions that absorption and fluorescence would be negligible in thin foils.

Jacobs and Baborovska (1972) examined the variation of the Cu/Au ratio with thickness in foils of Cu - 75.5% Au. These workers used the continuum intensity, previously calibrated against twin boundary traces, as their thickness measuring device. They found that various intensity ratios behaved differently over the range of thicknesses studied (0-0.3μm). For 100kV electrons the ratio $I_{Au\ M\alpha}/I_{CuK\alpha}$ decreased with increasing thickness due to preferential absorption of the AuMα x-rays in the specimen. At the same operating voltage the $I_{AuL\alpha}/I_{CuK\alpha}$ remained constant up to the maximum thickness measured but at a 40kV operating voltage, when the foil appeared opaque, this same ratio decreased with increasing thickness. This, the workers concluded, was not an absorption phenomenon, but due to a proportion of electrons losing energy on their journey through the foil. These less energetic electrons are more capable of generating the CuKα x-rays than the AuLα, hence the changing ratio with thickness.

Lorimer, Cliff and Clark (1976) substituted the element silicon for element B in equation 1.19 and

experimentally determined K_{Asi} or K values for a number of elements. In the same paper they also discuss the increasing CuKα/AlKα ratio observed in thinner regions of an Al-$CuAl_2$ eutectic foil. This was regarded as being due to the preferential absorption of Alkα x-rays in the carbon contamination that builds up during analysis. This effect was noticed in NiAl foils by Zaluzec and Frazer (1978) who also attributed it to preferential absorption of the Al characteristic line in carbon contamination. However, in the geometrical TEM configuration the x-ray detector is not aligned with the electron beam and x-rays reaching it do not, therefore, have to travel through the thick contamination cones that build up. Also the low absorption of AlKα rays in carbon (mass absorption coefficient, $\mu = 557.2\ cm^2g^{-1}$) would require a contamination layer 1400nm thick to reduce its intensity by 10%. It is more likely that these workers analysed samples which were covered in a thin film, excessively rich in Cu (Lorimer et al) or Ni (Zaluzec & Frazer.) This has been investigated by other workers and is discussed later in the section. Lorimer's thickness values were obtained using the contamination spot technique.

Using the ratio technique', Bender Williams and Notis (1980) found no preferential absorption in carbon contamination when they studied foils of MgO-10mol% NiO, despite the high (relative to Ni) absorption coefficient of Mg in carbon. They did however observe that the Ni/Mg x-ray intensity ratio increased quite markedly

with thickness (as measured by the contamination spot method). This, they calculated, was entirely due to the preferential absorption of Mg characteristic lines in both Ni and the surface oxide. When the results were fully corrected for these effects a thickness independent value of the ratio was found. Lorimer, Al-Salman and Cliff (1977) observed that the K value for a Fe-2wt%Si alloy was not independent of thickness, with the apparent Si composition falling with increasing thickness due to the preferential absorption of the Si characteristic line. They also noted fluorescence effects in Cr-Fe samples giving an enhancement of the Cr characteristic line. This is most pronounced in low Cr content foils, increases with thickness, and is due to the fluorescence of Cr x-rays by the more energetic Fe x-rays.

The presence of what appears to be thin surface films have been noticed on a number of foils by various workers. The surface film appears richer (or depleted) in one of the bulk elements. When using the ratio technique the apparent concentration of the 'surface rich' element is enhanced in very thin regions. Various works have shown the apparent enrichment of Cu in Al-Cu alloys, Morris Davies and Treverton (1977), Thompson , Doig, Edington and Flewitt (1977), Pountney and Loretto (1980), Jones and Loretto 1981; Ag in Al-Ag alloys, Morris et al (1977), Sawley, Cliff and Haworth (1977); Zn in Zn-Al alloys, Doig and Flewitt (1977); Ni in Ni-Fe

alloys, Morris and Lamb (1978); and Si in Si-Fe systems, Russ (1977). Such variations in the ratio of two elements may be useful in thickness determinations for the systems mentioned.

In a number of instances, the variation in x-ray spectra with thickness has been used to measure this parameter. As mentioned previously, Jacobs and Barborovska (1972) correlated the intensity of a portion of the continuum radiation with foil thickness. This had been previously investigated by Hall (1971), who was concerned with measuring microtomed biological sections. However, the low counts of the continuum gave rise to large statistical uncertainty in their measurements. Bentley and Kenik (1976), in a study of several metals, reported that characteristic x-radiation intensities varied in a linear fashion with foil thickness (measured using thickness fringes). They conclude from their results that absorption of x-rays in the foils is not important, even for low energy x-rays in high Z materials. This conclusion does not apply to all systems, as earlier revealed by the work of Bender et al.

Morris (1979) and later Statham and Ball (1980) obtained spectra from a single analysis point for different specimen tilt angles. This produced a series of data with known relative path lengths. From the relationship between the relative path lengths and the spectra intensity (or ratio variation if two or more elements are present) the absolute path length of the

x-rays could be determined and the thickness calculated. An alternative approach by Morris (1979), for systems containing at least one element with detectable K and L lines, was to obtain the intensities of the two characteristic lines from one element and, from a knowledge of K_B^A factors, adopt a value of path length which would give a concentration ratio $C_A(\text{line } 1)/C_A(\text{line } 2 = 1$. In the former method, Statham and Ball found that despite the application of absorption correction procedures, elemental ratios still varied with foil thickness. They concluded that ambiguity in the exact specimen geometry was probably the major source of the associated errors.

1.3 Summary of available methods

The ideal method for determining foil thicknesses must be capable of providing accurate and precise in situ measurements over a wide range of thicknesses on a wide range of materials. The regions of interest to be measured should be determined by the operator and not be restricted to areas where a particular thickness related phenomenon occurs. The methods mentioned previously possess these qualities in varying degrees. Their potential is here briefly reassessed.

Methods utilizing extinction contrast, whether it be thickness fringes or bend contours, are inflexible. The presence of such effects is not guaranteed and when present they are often not in the area of interest. Thickness contours are only present in the thinner regions of foil but the accuracy of the method depends

on exact Bragg orientation, this being determined using Kikuchi lines in thicker regions of foil. The possibility of some ambiguity of foil orientation in the area of the fringes is therefore a real one. The convergent beam method, while relying on the same diffraction contrast mechanisms, overcomes many of the limitations inherent in the fringe methods. The position of each measurement is determined by the operator. Some adjustment to the specimen orientation to obtain two-beam conditions may be required and this could impose a limitation on the technique's flexibility. The dimension measured using this method is the thickness of the sample in the beam direction.

Static crystallographic techniques requiring diffraction data to ascertain the precise fault orientation may produce large errors in thickness if the exact inclination of the foil surface is unknown. The uncertainty from this factor is removed when several intersecting traces are used in the analysis. The probability of such intersections in the area of interest is however small. In addition, the tedious computation required in the analysis does not always produce a unique thickness value.

The tilting methods of Vingsbo (1970) and Thompson and Chen (1979) are promising, although the first has a poor level of accuracy and both include errors arising from uncertainty in the foil surface inclination. The averaging of data at several tilt angles will reduce

errors that are associated with single readings.

Surface artefact techniques are perhaps the most important methods available for measuring foil thickness. The lack of restrictions on their use give them a flexibility unknown in other techniques. Materials to be examined need contain no large defects and the qualification of crystallinity, needed for materials measured by the convergent beam technique, need not apply. The contamination spot technique is completely operator controlled whereas the presence of latex spheres in an area of specific interest is rather fortuitous.

Of the methods requiring calibration, energy loss spectroscopy requires much specialised equipment. It has been proposed by Cundy (1967) and Radi (1968) that the level of the energy loss may be dependent on the degree and sign of the crystal deviation from the Bragg angle, i.e. anomalous transmission and absorption effects. Bragg diffraction will also affect the energy loss spectrum as each diffracted ray will act as a new source. These Bragg rays will contribute to the spectrum when the semi-angle of collection, α, is greater than the Bragg angle. If α is less than θ_B some diffracted rays will not contribute to the final spectrum. These effects may be minimised by kinematical diffraction conditions where the total diffracted intensity is much less than that of the transmitted beam. This however, effectively reduces the application of the method to measuring the thickness of thin areas of weakly scattering materials (low Z).

Electron absorption is a simple technique in concept but several variables other than specimen thickness can influence the level of absorption. In crystalline materials anomalous absorption or transmission may reduce or enhance the transmitted intensity. Under dynamical conditions of diffraction some high order diffracted rays may miss being detected altogether. This calls into question its use in measuring the thickness of crystalline films. The method is initially calibrated using evaporated films of known thickness which may not be of the same density, and therefore not have the same absorption coefficient, as bulk thinned material. Other calibration procedures would have to be applied to this method to enable its use for alloy systems.

Electron backscattering techniques preserve the advantages of the absorption method, i.e. localised direct thickness determination and good adaption to the TEM, while the disadvantages mentioned above are avoided. The backscattered intensity, according to Niedrig (1978), is proportional to the film thickness within a large range of thicknesses and is insensitive to crystal size or orientation. This, it is argued, is because a single atom within the crystal acts as the collision partner and not the whole crystal lattice. Dynamical interference effects are therefore less important than in the forward transmission of elecrons.

The dependence of x-ray intensities on foil thickness is difficult to ascertain in isolation. Workers have determined empirical relationships between the characteristic or continuum intensity and foil thickness. Variations in beam current will affect the intensity readings and any resultant thickness values will consequently be in error. Ratios of simultaneously obtained characteristic or continuum spectra will be insensitive to such deviations in beam current. They may however, still be related to the foil thickness due to absorption and fluorescence effects in the foil or the presence of thin surface films.

1.4 Scope of the investigation

The reader will by now be aware that the usefulness of any thickness measuring device depends upon the situation in which it is required to operate. Some techniques are particularly restrictive in their application. The main purpose of this work is to investigate in detail thickness measuring techniques which, in view of the criteria given in 1.3, possess the greatest potential. The assessment of the accuracy and precision present in each method will be examined together with an appraisal of possible sources of error.

Where possible, direct comparisons will be made of different methods. This will determine if each method is measuring the same parameter of 'thickness'. Such comparisons will be deduced indirectly when a direct approach is not feasible.

When, during the course of study, a method is found to be inadequate in some respect, modifications may be applied to remedy the situation. It is expected during the course of the study that the applicability and flexibility of each technique will be determined. At the end of the investigation either a single method will present itself as being universally capable of providing accurate thickness values in any situation, or a number of techniques will be recommended for use in different areas of study.

The methods chosen for initial study are: the contamination spot technique, convergent beam diffraction, crystallographic analysis and calibrated x-ray methods. Crystallographic techniques, although suffering from inflexibility in their application, were designated for use as a 'yard stick' (almost literally) by which to assess the other techniques. Electron backscattering and Energy Loss Spectroscopy were not chosen for two main reasons. The equipment needed for such analyses was not readily available for the investigation and is still not available to a majority of TEM users. Secondly, these techniques have been well investigated by other workers to a degree which renders their inclusion unnecessary in this investigation. Other techniques mentioned in the previous section fulfil too little of the criteria required and/or have been fully investigated elsewhere.

2. THE ANALYTICAL TRANSMISSION ELECTRON MICROSCOPE

The modern transmission electron microscope cannot solely be considered as a powerful microscope. In addition to its conventional role the instrument may be employed to provide a variety of different images, each yielding information which provides a more complete 'picture' than hitherto available. X-ray analysis, scanning transmission electron microscopy, secondary and backscattered electron imaging together with micro-diffraction techniques are just some of the extra capabilities incorporated in the modern instrument. With such facilities for high resolution observation, crystal structure determination and compositional data acquisition, the electron microscope becomes almost an analytical laboratory.

To appreciate the capabilities of the instrument some discussion of the various aspects of TEM is necessary. This will mainly be an appreciation of the different instrument modes that are encountered elsewhere in the investigation but will also include some fundamental aspects of relevant theory. The reader is referred to any one of the excellent books and reviews mentioned in the bibliography for a more comprehensive approach to general electron optical theory.

2.1 Transmission electron microscopy (TEM)

TEM is analogous to ordinary optical transmission microscopy, with electrons rather than light being used to form the image. Instead of glass for the lenses and air for the transmission medium, the electron microscope uses a series of electro-magnetic coils to focus a beam of highly accelerated electrons through the specimen in vacuo. Fig. 12 shows the main features of such an electron microscope. The electron source is commonly an electrically heated tungsten filament set at a selected negative potential in the 20-100kV range and mounted on an insulator behind a Wehnelt cylinder. This is slightly negative with respect to the filament and the thermionically emitted electrons are therefore forced through the cylinder on their journey to earth. During this journey they are focussed by a double condenser lens (only one is shown in Fig. 12 for simplicity) onto the specimen. The transmitted electrons form an image which is focussed with the objective lens and magnified by a number of intermediate and projector lenses to form a final image on a fluorescent screen.

2.1.1 Resolution

Operating at a typical 100kV potential, an electron wavelength of 0.037Å is obtained. The theoretical resolution is obtained from the Rayleigh Criterion. This gives the closest approach distance of two points for which they are still resolvable as two points.

Fig. 12

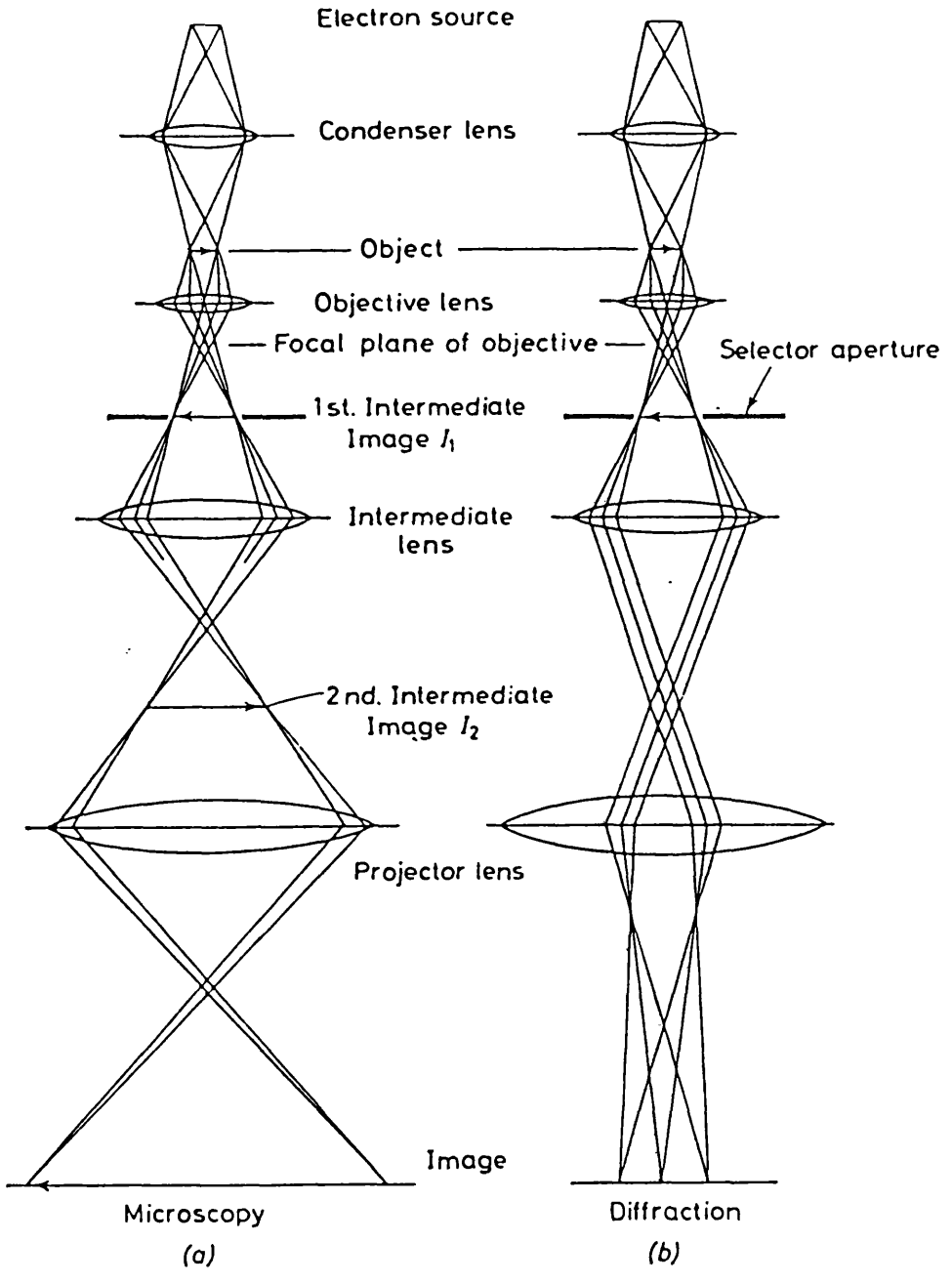

Fig. 12 Ray paths in the electron microscope

(a) imaging conditions and

(b) diffraction conditions (after Hirsch et al 1965).

The Rayleigh equation is

$$R = \frac{0.61\,\lambda}{\alpha} \qquad 2.1$$

where R is the size of the resolved object, α is the maximum angle of electron scattering - equal to the effective aperture of the objective lens and λ is the electron wavelength.

The effective aperture of the objective lens in electron microscopy and hence the resolution is limited by a number of factors, the most important of which is spherical aberration of the objective lens. This occurs as a result of the differential focussing of rays passing through the centre of the lens and those towards the periphery, the effective focal length of the latter being slightly less. This error can be expressed as a function of α and is given by

$$\Delta S = C_s\,\alpha^3 \qquad 2.2$$

where ΔS is the radius of a disc, the image of a point in the object plane (see Fig. 13a) and C_s is the spherical aberration constant of the objective lens. As can be seen from equations 2.1 and 2.2, conditions of best resolution are subject to an optimum value for α which will yield high resolution while keeping spherical aberration values low. The following equations have been derived to give these values.

$$\alpha_{OPT} = A(\lambda^{\frac{1}{4}})C_s^{-\frac{1}{4}} \qquad 2.3$$

Fig. 13

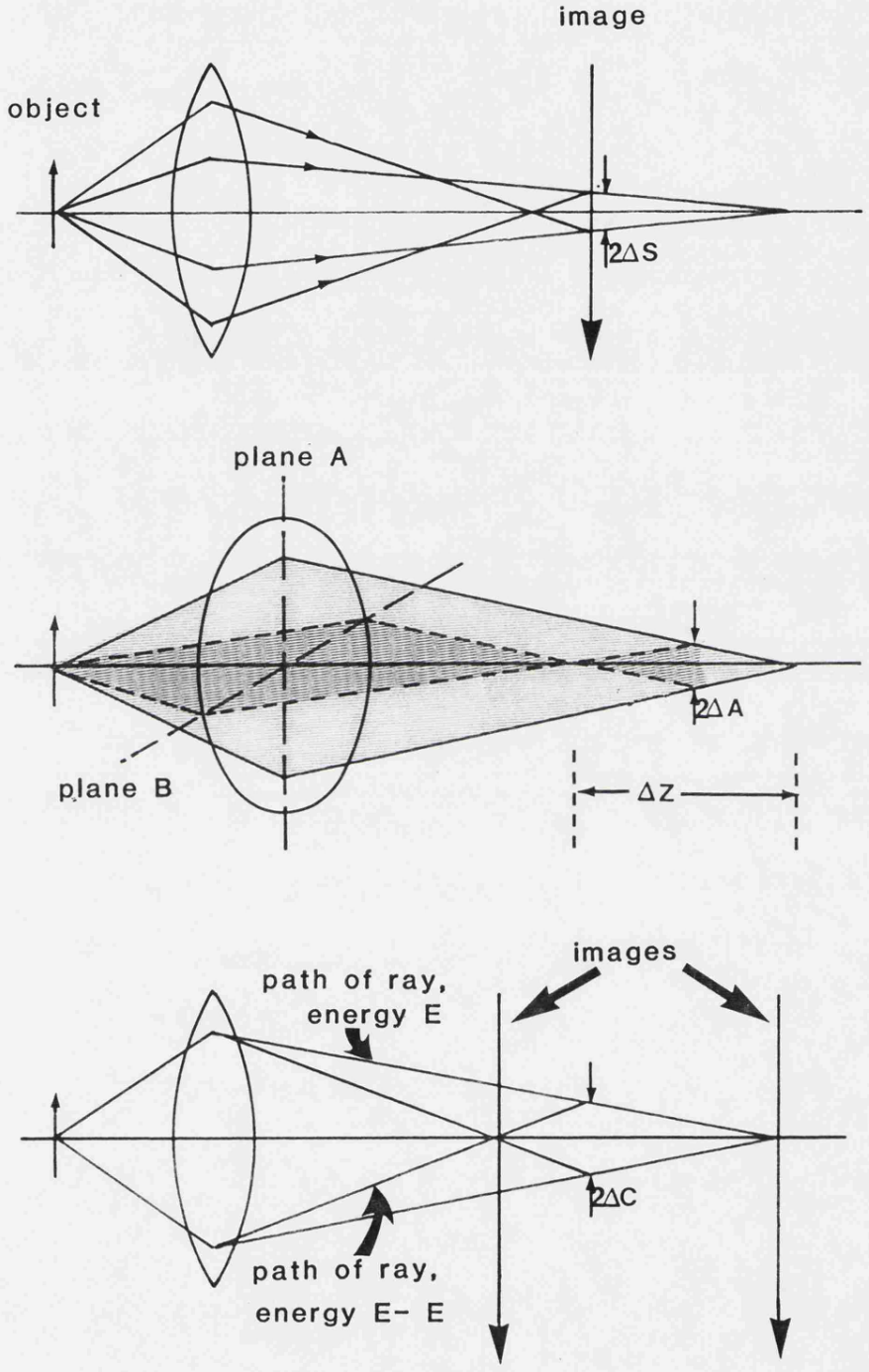

Fig. 13 Aberrations of the objective lens (a) spherical (b) astigmatism (c) chromatic

$$\Delta R_{MIN} = B(\lambda^{\frac{3}{4}})C_s^{\frac{1}{4}} \qquad 2.4$$

ΔR_{MIN} is the minimum radius of confusion for a point source and A and B are constants approximating to unity. With the present state of lens technology resolutions of 3-4 $\mathring{A}$ may be obtained with a 100KV instrument.

Other factors that degrade resolution, but to a lesser extent, include astigmatism and chromatic aberration. The former aberration arises from defects in the machining of the lens pole-pieces. The lens effectively has different focal lengths for paraxial rays in the two principle planes of asymmetry but can easily be corrected for by the application of compensating magnetic fields. The equation governing the astigmatic error is given as:

$$\Delta A = (\Delta Z)\,\alpha \qquad 2.5$$

where ΔA is the radius of the disc of confusion and ΔZ is the distance between the two line foci arising because of the astigmatism, (see Fig. 13b).

Chromatic aberration, due to electrons losing various amounts of energy to the system and specimen, results in electron rays being focussed at different points along the principle axis (Fig. 13c). This error is calculated from the equation:

$$\Delta C = C_c \alpha \frac{\Delta E}{E} \qquad 2.6$$

with ΔC being the radius of the disc of confusion and C_c the chromatic aberration coefficient. It can be seen that increasing the voltage E will decrease this

aberration.

The size of the disc of confusion i.e. the minimum spot size that can be obtained in TEM is given by:

$$R_{aber}^2 = R^2 + \Delta S^2 + \Delta C^2 + \Delta A^2 \qquad 2.7$$

Typically at 100KV point to point resolutions of about 3-4 Å can be obtained after optimising the above conditions.

2.1.2 Depth of field and focus

The depth of field obtained in an electron microscope, D, is extremely large in comparison with a light microscope. This is a result of the very small wavelength of the electrons and small angular apertures of the imaging system. The depth of field is given by

$$D = \frac{R}{\alpha} \qquad 2.8$$

for small values of α.

Employing values of 10Å for the resolution and 2×10^{-3} rad, for the angle α results in a depth of field of 5000 Å. Since most thin film regions examined are of this order of thickness or less, all features are in focus simultaneously.

The depth of focus for the image, D_F is related to D by the equation

$$D_F = DM^2 \qquad 2.9$$

which for magnification values, M, of 50,000 results in depth of focus of 1.25 kilometres! Hence it is quite practical to situate photographic equipment at some

distance below the viewing screen.

2.1 3 Diffraction

Contrast in the TEM formed image depends on the distribution of the electrons that emerge from the bottom surface of the specimen. Highly ordered crystalline materials, such as metals, where the interplanar distances are typically two orders of magnitude greater than the accelerated electrons wavelength result in the production of diffraction effects.

As a collimated beam of electrons pass through such a crystalline specimen scattering occurs with emergent rays having a path difference according to Braggs Law i.e.

$$n\lambda = 2d \sin \theta \qquad 2.10$$

where θ is the angle between the incident ray and the diffracting plane and d is the interplanar distance. The small angle scattered beams ($\simeq$ 1 or 2^{o}) may be focussed by the objective lens to form a diffraction pattern, or information from one or more of the diffracted rays may be used to obtain an image of the specimen.

The diffraction pattern is the Fourier transform of the specimen and is essentially a reciprocal picture of the atomic structure.

The requirements for electron diffraction are illustrated in Fig. 14. Monochromatic electron waves are considered to be reflected from planes of atoms

rather than scattered by individual atoms. This Bragg model gives the path difference between waves ABC and DEF as PEQ = 2d sin θ. For these waves to interfere constructively PEQ must equal an integral number of wavelengths i.e. nλ = 2d sin θ.

From this diagram it can be seen that the relative positioning of the focussed diffracted and transmitted rays is a function of the interplanar spacing d where

$$R = \frac{\lambda L}{d} \qquad 2.11$$

L is the effective distance of the specimen from the diffraction pattern, often called the camera length. Principally the reciprocal lattice consists of points, each of which corresponds to a plane in the real lattice and therefore may be indexed accordingly.

Conditions for diffraction can be obtained from the relationship between the reciprocal lattice and the Ewald Sphere. This is a sphere of radius $\frac{1}{\lambda}$ drawn through the origin of the reciprocal lattice (at 0 on the plane AB in Fig. 15), such that it intersects the reciprocal lattice point of plane AB (shown as C in Fig. 15). The incident beam is a diameter of the sphere and impinges on plane AB at O. The reciprocal lattice vector for plane AB is g_{hkl} and in this situation

$$\sin \theta_{hkl} = g_{hkl} \frac{\lambda}{2} = \frac{\lambda}{2d_{hkl}} \qquad 2.12$$

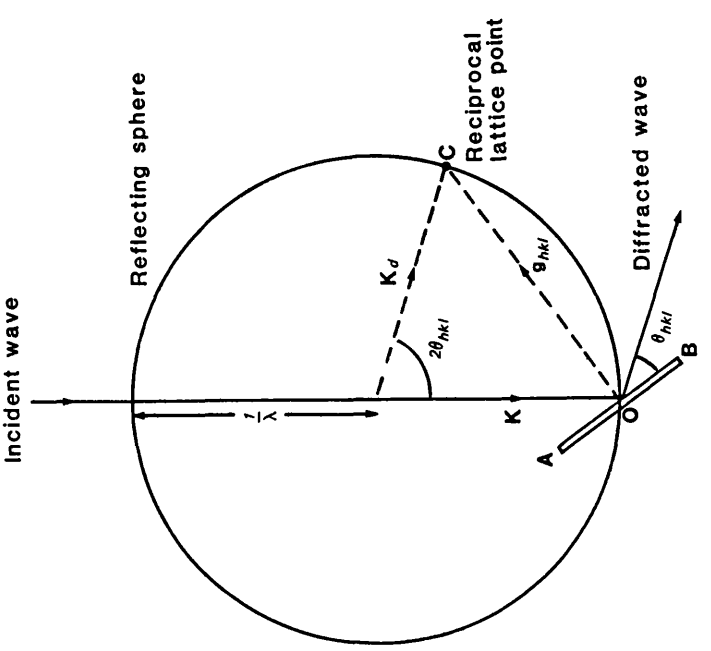

Fig. 15 Reciprocal lattice construction employing the Ewald Sphere.

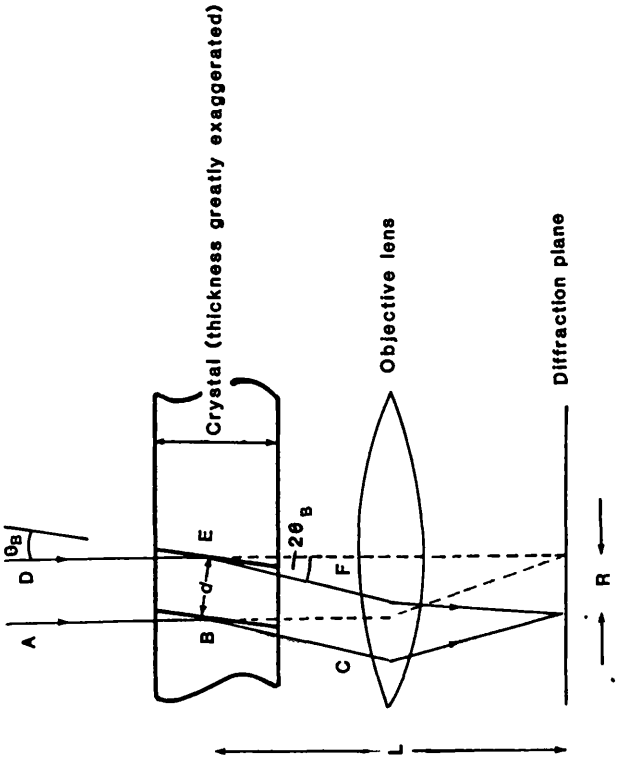

Fig. 14 Schematic representation of Bragg reflection from planes in a thin crystal (after Grundy and Jones 1976).

thus satisfying the Bragg equation. Strong diffraction effects will therefore only occur for reciprocal lattice points that intersect the Ewald Sphere. The wavelength of electrons accelerated through 100KV is ≈ 0.037 Å resulting in an Ewald sphere radius of 27 $Å^{-1}$ while typical reciprocal lattice points are of the order of 0.5 $Å^{-1}$ apart. The reflecting sphere therefore approximates to a plane with respect to these points. The diffraction pattern, which is a two dimensional projection of the reciprocal lattice, thus contains many spots. This for example, is in contrast to x-ray diffraction where, due to a smaller Ewald sphere ($\sim 1 Å^{-1}$ radius), fewer diffraction spots occur.

2.1.4 Image production and contrast

As previously stated, contrast in the TEM depends on the distribution of electrons emerging from the lower surface of the foil. These electrons are focussed by microscope lenses to form an image produced either from the recombination of two or more electron rays (phase contrast imaging), or more usually from only one beam. This latter method is termed amplitude contrast imaging or deficiency contrast due to the practice of stopping all but one beam from forming the final image.

The ray diagram for a TEM in its deficiency contrast mode can be seen in Fig. 12a and 16a. In this particular mode of operation only the directly

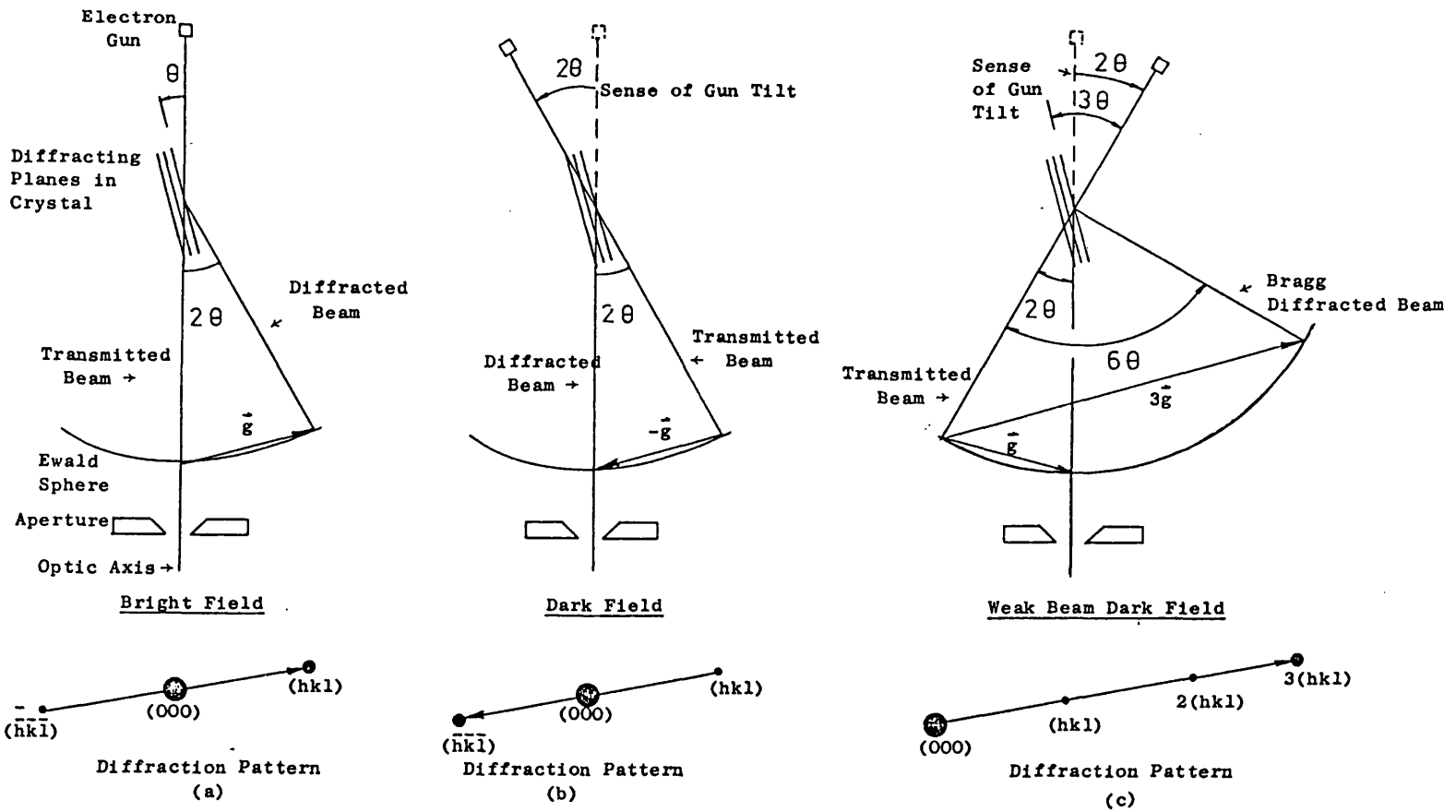

FIG. 16 Diffraction conditions for (a) bright field, (b) dark field, and (c) weak beam dark field. (after Thomas and Goringe 1976)

transmitted beam is used in the image formation. All diffracted rays are stopped by the insertion of an aperture below the objective lens. This is termed bright field operation (B.F.). The cathodic electron gun produces electrons which are accelerated by the anode (zero potential) and collimated by the condenser lens to form an almost parallel illuminating beam. Scattering processes occur as a result of the interaction of these electrons with the specimen and the different rays are brought to focus by the objective lens to produce a diffraction pattern in its back focal plane. The insertion of an aperture at this stage precludes all but the directly transmitted rays from forming the final image. The low magnification image formed by the objective lens is subsequently magnified by intermediate and projector lenses to form the final image on the viewing screen, the contrast being produced by differences in intensity of electrons scattered into Bragg reflections from various parts of the specimen. From a completely random specimen no such contrast would be expected as all areas of the sample would scatter randomly. Most amorphous materials do in practice however show some improvement in contrast when an objective aperture is inserted as they are not completely random in structure.

The image produced on the screen is focussed by adjusting the focal length of the objective lens while alterations in the excitation of the projector lens

changes the magnification.

The diffraction pattern that is produced in the back focal plane of the objective can be projected onto the viewing screen by adjusting the intermediate and projector lenses, see Fig. 12b. The objective aperture must of course be withdrawn for the full diffraction pattern to appear. The insertion of the intermediate aperture enables diffraction patterns to be obtained from selected areas of the specimen thus facilitating a direct correlation between morphological and crystallographic information.

In a similar manner to the BF technique an image may be produced using a diffracted rather than directly transmitted ray, Fig. 16b. For this to occur either the objective aperture must be moved or the electron beam tilted electromagnetically to allow the passage of a diffracted ray. The former method produces large spherical aberration errors as the diffracted beam lies at an angle to the objective axis, and hence the tilted beam method is generally preferred. The resultant dark field image, (DF), differs in contrast to the BF image and provides useful complimentary information in characterising microstructures.

To obtain a beam tilted DF image the specimen is oriented for two beam conditions giving a strong reflection. The beam is then tilted such that the diffraction conditions remain unchanged. This in practice entails tilting the beam such that the weakly excited spot moves to the centre of the viewing screen.

Opposite tilting will disturb the diffraction conditions and produce a weak beam image of very low intensity on the viewing screen Fig. 16c.

Another method of imaging that finds application in high resolution studies, such as lattice imaging, is that of phase contrast. In diffraction contrast any information of atomic arrangement is lost. This is because details from periodic structures can only be obtained by the interference of the directly transmitted beam and one or more of those undergoing diffraction. In phase contrast several such beams are recombined to produce, in the case of a crystalline specimen, periodic fringes on the viewing screen. These fringes correspond to the planes responsible for the diffraction. This technique together with weak beam imaging are specialised in their application and are discussed more fully elsewhere. (Thomas and Ḡoringe 1976).

2.2 Scanning transmission electron microscopy (STEM) and Secondary electron microscopy (SEM)

In contrast to the essentially parallel beam used in conventional TEM, in STEM and SEM the electron beam is focussed to a fine probe which is then scanned over the specimen by electro-magnetic coils.

In SEM the detector is placed above and to one side of the specimen and detects secondary electrons. These are electrons of atoms in the specimen, emitted

from its surface due to excitation by the primary incident electrons. They have very low energy, typically 0 - 50eV and only those from the immediate surface layers avoid absorption and are counted. The image is therefore of the specimen surface and is very sensitive to topographical changes. The collector has a slightly positive bias enabling it to selectively detect only low energy electrons. The more energetic backscattered electrons are not collected by the device. The electron signal reaching the detector at any instant is a function of the rastering probe position. This signal is electrically amplified and a second set of scanning coils, operating in tandem with the probe scanner, positions the signal on a cathode ray tube (CRT) to provide the picture.

STEM is similar to SEM in many respects, the important difference being that transmitted rather than reflected electrons are used in forming the image. The detector is usually found below the fluorescent screen used for normal TEM observations and detected electrons are processed in a similar manner to that described for SEM.

A comparison of the optical systems of STEM and TEM in Fig. 17 shows that a reciprocal arrangement exists between the two. It is not therefore surprising that the images formed by the two systems are similar in many respects. The lack of lenses below the specimen in STEM reduces aberration errors in the final image. Chromatic aberration, especially when

Fig. 17

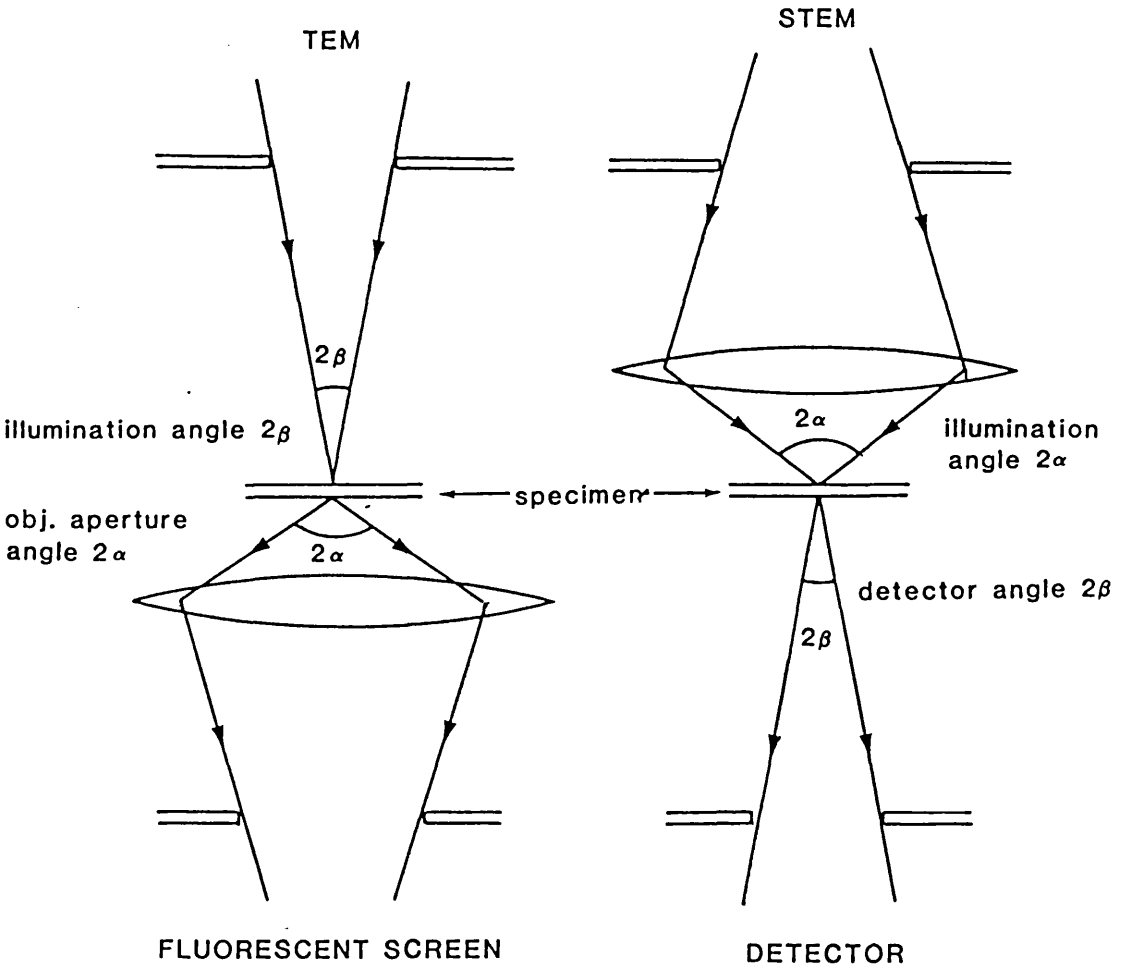

Fig. 17 Reciprocal arrangement of TEM and STEM.

observing thick specimens, is less of a problem and it has been claimed (Seller and Cowley 1973) that for a given resolution, contrast could be up to four times better for STEM. However, contradictory results have been found which suggest that this is not so, these reports being reviewed more fully by Easterling (1977).

The resolution in STEM is determined by the electron probe diameter which has been estimated as being $\sim$ 30 Å for a microscope at 100kV using a tungsten filament gun to produce electrons. This of course is not as good as the 3-4 Å available in TEM.

A major advantage of STEM is that the very fine probes may be used to obtain microanalysis data from very small areas. The probe is held stationary in these instances and selected areas of 0.02μm diameter may be examined. Diffraction patterns can therefore be obtained from small areas (precipitates etc) or x-ray analysis with high spatial resolution may be performed.

2.3 The energy dispersive spectrometer

The electron microscope is easily adapted for x-ray production and analysis as it already possesses a system for directing energetic electrons at a specimen target. Using the fine probe available in STEM mode enables very small areas of sample to be quickly and easily analysed. The system in operation

within the electron microscope contrasts with the conventional electron microprobe analyser. In this instrument bulk materials are analysed and the theories of quantitative analysis include various correction factors for processes such as absorption and fluorescence (Salter 1970).

Once the x-rays have been produced from the specimen they are analysed using a lithium drifted silicon detector. This detector is a semiconductor having a fully occupied valence band and empty or nearly empty conduction band at a slightly higher and separate energy level.

Any incident radiation will, if energetic enough, raise an electron from the valence to conduction bands creating an electron-hole pair, thus enhancing the conductivity of the detector. With a voltage applied across the detector, current will flow in direct relation to the energy of incident radiation.

Noise considerations require the detector to be of the highest resistivity, which will greatly reduce DC leakage. Even the purest silicon conducts as a result of thermally excited electron hole-pairs and with impurities present this conductivity is increased. The most important of these impurities is boron which renders silicon a 'p' type semiconductor. This can be compensated for by diffusing lithium into the matrix, under an applied electric field, giving an intrinsic-type high resistivity material. Electrical pulses, characteristic of the incident x-rays, are

produced and pre-amplified by a field effect transistor (FET) which offers a good signal to noise ratio. This together with the detector is cooled by liquid nitrogen constantly to prevent further diffusion of lithium in the detector; noise reduction also being aided.

The pulses are further amplified and the resultant energy spectrum fed into a multichannel pulse height analyser where pulses are classified according to their height (energy) and the number of pulses of each specific energy is counted. The resultant spectrum is usually then displayed on a CRT or graphically plotted. Thus a whole range of x-rays of different elements can be recorded simultaneously.

3. THE USE OF CRYSTALLOGRAPHIC FEATURES IN DETERMINING THICKNESS

A technique utilising stacking faults is discussed, with particular reference to the image contrast of these coherent defects. Secondly, a method is investigated in which errors due to ambiguity in the orientation of the foil surface are eliminated. This is a tilting method employing slip traces and other defects.

3.1 Preparation of Specimens for TEM Examination

The first stage of specimen preparation for TEM work involved making flat discs 3.0mm in diameter and less than 0.5mm thick. From material in the form of thin sheets, the discs were stamped out, while for cast alloys a thin slice of metal was removed and gently ground flat prior to stamping. The discs were then mechanically thinned to less than 0.5mm thickness using a special adjustable holder and fine emery paper.

After being cleaned in an ultrasonic bath, samples were further thinned by electropolishing in a Tenupol apparatus. Here the specimen forms the anode of a D.C. electrolytic cell, with the electrolyte directed onto the sample from nozzles on either side which also form the cathodes. The gradual erosion of the anodic specimen takes the form of a polishing operation under controlled conditions of current, flow rate and temperature. The temperature of the electrolyte has to be kept well below room temperature in most

instances and this can be accomplished by pumping cold water, carbon dioxide/alcohol mixtures or liquid nitrogen through a cooling coil immersed in the electrolyte. The presence of a large reservoir of electrolyte helps to maintain stable temperature conditions.

To either side of the specimen are a light source and a photocell. The eventual perforation of the sample is accompanied by the activation of the photocell, this causing the disconnection of the thinning power supply and the activation of a warning buzzer. Rapid withdrawal and cleaning (dipping in beakers of alcohol) of the sample prevents further chemical attack of the very thin regions immediately adjacent to the perforation. The sample is then dried and is ready for TEM examination.

The conditions of preparation and the composition of the materials used are given in tables 1 and 2. In this particular section, stainless steel, aluminium and copper were examined.

The prepared foil is inserted into the previously aligned TEM and its height carefully adjusted until eucentric conditions are obtained. In this position the foil tilt axis lies in the same plane as the focussed electron probe and the specimen may be tilted while keeping the same field of view on the microscope screen. In addition, the magnification stays constant for different tilt angles. Conditions were set at

MATERIAL	wt% COMPOSITION/CONDITION								
Al	99.999% pure, ½" diameter round bar								
Cu	Commercially pure sheet, 1mm thick								
Stainless Steel	Austenitic sheet, ½mm thick. Nominal 18%Cr, 8%Ni, Bal.Fe.								
Al-Cu alloys	wt% COMPOSITION (All alloys available as castings)								
	Cu	Mg	Ag	Mn	Ti	Zr	Si	Fe	Al
AUWE alloy P89	4.87	<0.01	<0.01	0.31	0.14	<0.02	<0.05	0.05	BAL
AUWE alloy P91	4.92	0.27	0.44	0.31	0.15	<0.02	<0.05	0.05	BAL
BATH alloy A1	3.01	0.26	1.03	<0.02	0.11	<0.01	0.05	0.05	BAL

Table 1. Composition of materials used in foil thickness and precipitation studies.

MATERIAL	ELECTROLYTE	CURRENT	FLOW RATE NUMBER	TEMPERATURE
Al & Al-Cu alloys	1 vol. Nitric acid 4 vols Methanol	150mA	5-6	-20°C
18.8 Austenitic stainless steel	1 vol. Perchloric Acid (60%) 20 vols Acetic Acid (99%)	150mA	3-4	14°C
Copper	1 vol Nitric acid 4 vols Methanol	130mA	5-6	-20°C

Table 2. Conditions of Electropolishing

100kV with a beam current of 100μA and liquid nitrogen was poured in the anti-contaminator trap to minimise the build up of surface contaminant films during the study.

3.2 Crystallographic Analysis

Stacking faults occur on {111} planes in face centred cubic materials such as austenitic stainless steel. They are created as a result of either the removal or insertion of an extra plane of atoms thus disrupting the normal stacking sequence. The two types are called intrinsic and extrinsic faults respectively.

A stacking fault in a stainless steel sample is shown in Fig. 18a. The fringe contrast is due to a phase factor being introduced by the fault of $\alpha = 2\pi \underline{g}\,\underline{R}$ which affects both the transmitted and diffracted rays. $\underline{R}$ is the displacement of the planes caused by introducing the fault and $\underline{g}$ is the reciprocal lattice vector of the operating diffraction plane.

As the thickness of the specimen increases fringes add from the centre by branching of existing fringes. For perfect two beam conditions i.e. $\underline{s} = 0$ the number of dark fringes n, gives the foil thickness $(n - 1)\xi_g$ = foil thickness t. When $\underline{s} \neq 0$ the extinction distance value changes and there is no simple relationship between n and t. The value of ξ_g must also be known to use this technique, this not always being tabulated for alloy systems and less common elements.

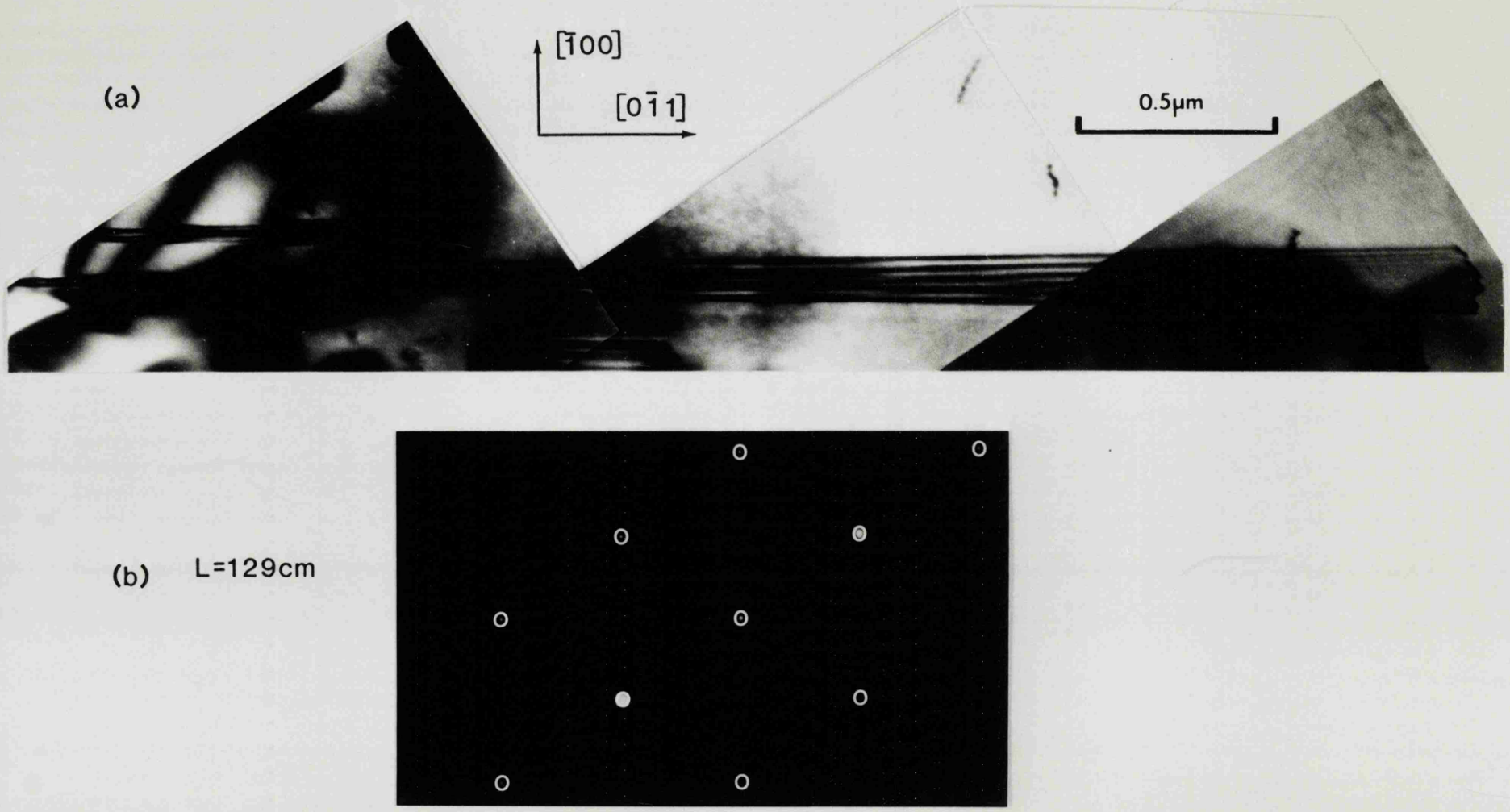

Fig. 18 (a) Bright-field image of a stacking fault in stainless steel, (b) corresponding diffraction pattern.

A method less likely to incur such errors involves determining the orientation of the stacking fault with respect to the electron beam. This is the method investigated next.

Figure 18 shows a stacking fault in stainless steel together with a select area diffraction pattern. The fault appears to diverge because the foil is tapered as a result of the thinning process.

From the diffraction pattern the plane was found to lie on either a (111) or $(\bar{1}\bar{1}1)$ plane, both of which are inclined at an angle of 54.7^{o} to the beam direction [011], this being calculated from equation 3.1.

$$\theta = \cos^{-1} \frac{h_1 h_2 + k_1 k_2 + l_1 l_2}{\sqrt{(h_1^2 + k_1^2 + l_1^2)(h_2^2 + k_2^2 + l_2^2)}} \qquad 3.1$$

where $(h_1k_1l_1)$ and $(h_2k_2l_2)$ are the Miller indices of the respective planes. Knowing the angle of inclination θ the foil thickness can then be calculated using equation 1.8 viz $t = W \cot \theta$, where W is the projected fault width. Foil thickness was plotted against distance from the foil edge, Fig. 19, to give a linear relationship. This showed that the foil, in the vicinity of the fault, had been thinned to a nearly perfect wedge tapering to about 15nm thick (extrapolated) at the edge. The maximum thickness measured was 120nm.

Possible errors in the thickness values obtained by the stacking fault method can arise from three main sources; errors in θ, errors due to non incidence

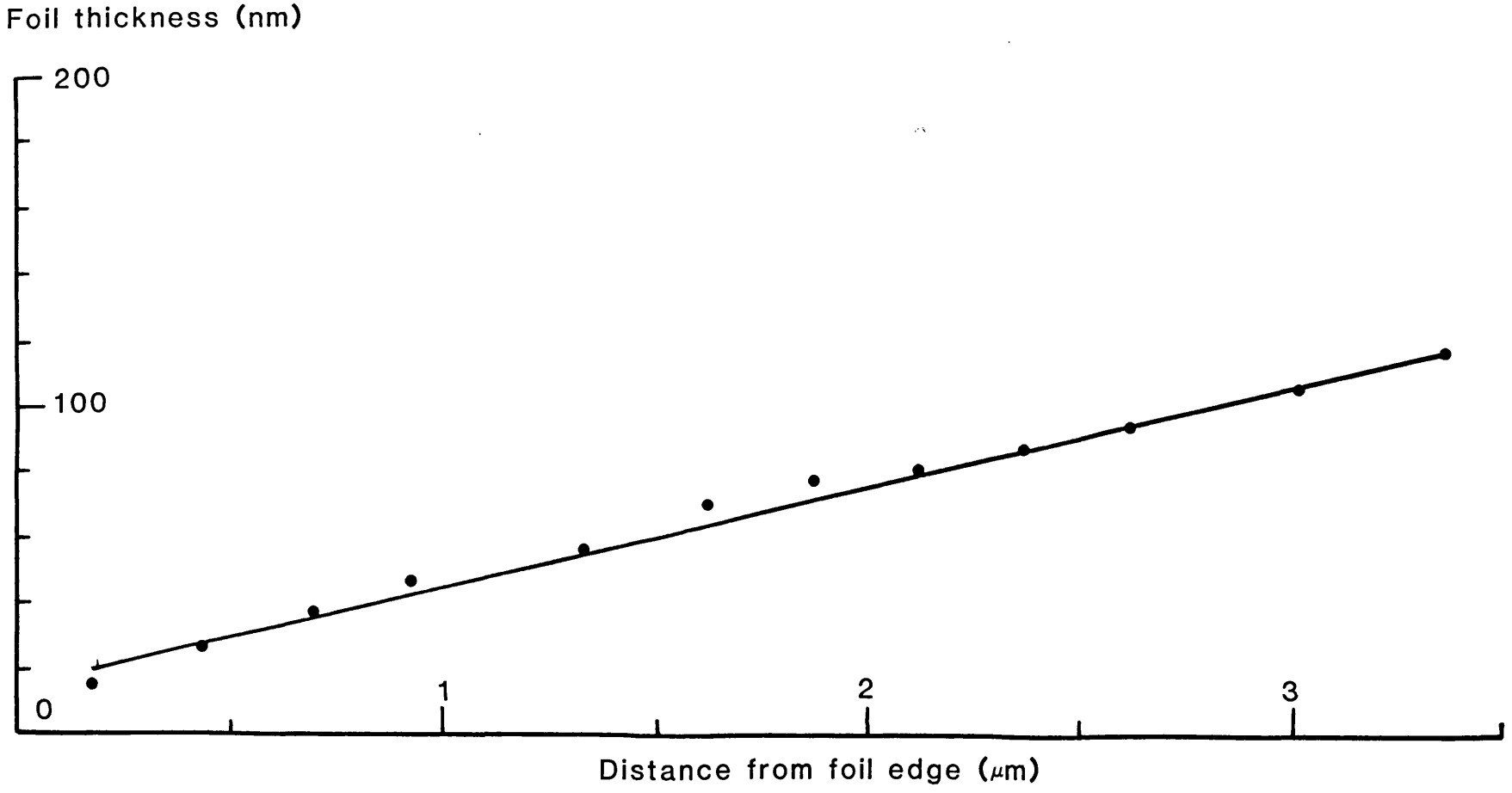

Fig. 19 Foil thickness variation along a wedge shaped specimen, as determined from the bright field image of a stacking fault.

Fig. 19

of foil normal and beam, and errors in W. Errors due to the second factor have already been discussed in the introduction and there is little one can do to quantitatively assess them. Ambiguity in θ can be minimised by using 2-beam diffracting conditions. The alignment of Kikuchi lines with the transmitted and diffracted spots can reduce errors in this parameter to a fraction of a degree. If it is not possible to orientate the specimen satisfactorily to obtain 2-beam conditions, or Kikuchi lines are not present in the diffraction pattern, the error in θ may be a few degrees.

The potential uncertainty in the image width W depends on the accuracy of the instrument magnification and correct interpretation of image contrast. The lattice imaging of beef liver catalase crystals was used to calibrate the magnification to within an accuracy of one per cent. These cells have lattice spacings of 8.75 nm and 6.85 nm and are easily visible at high magnification as may be observed in Fig. 20.

As the image of the stacking fault depends on diffraction contrast its width was measured under different diffraction conditions. Bright and dark field images of a stacking fault were obtained by imaging with the transmitted beam and a $\{111\}$ diffracted beam. Fig. 21 shows the fault under the two different imaging conditions.

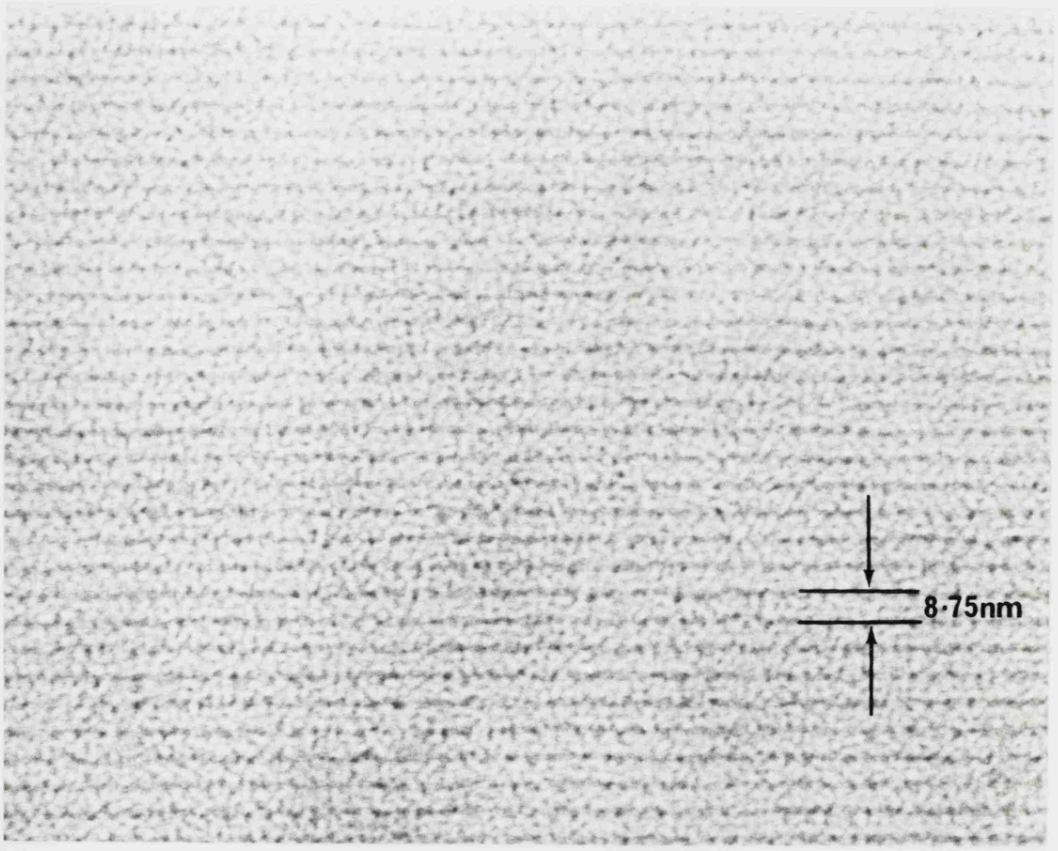

Fig. 20 Image of Beef Catalase crystal lattice, used in magnification calibration.

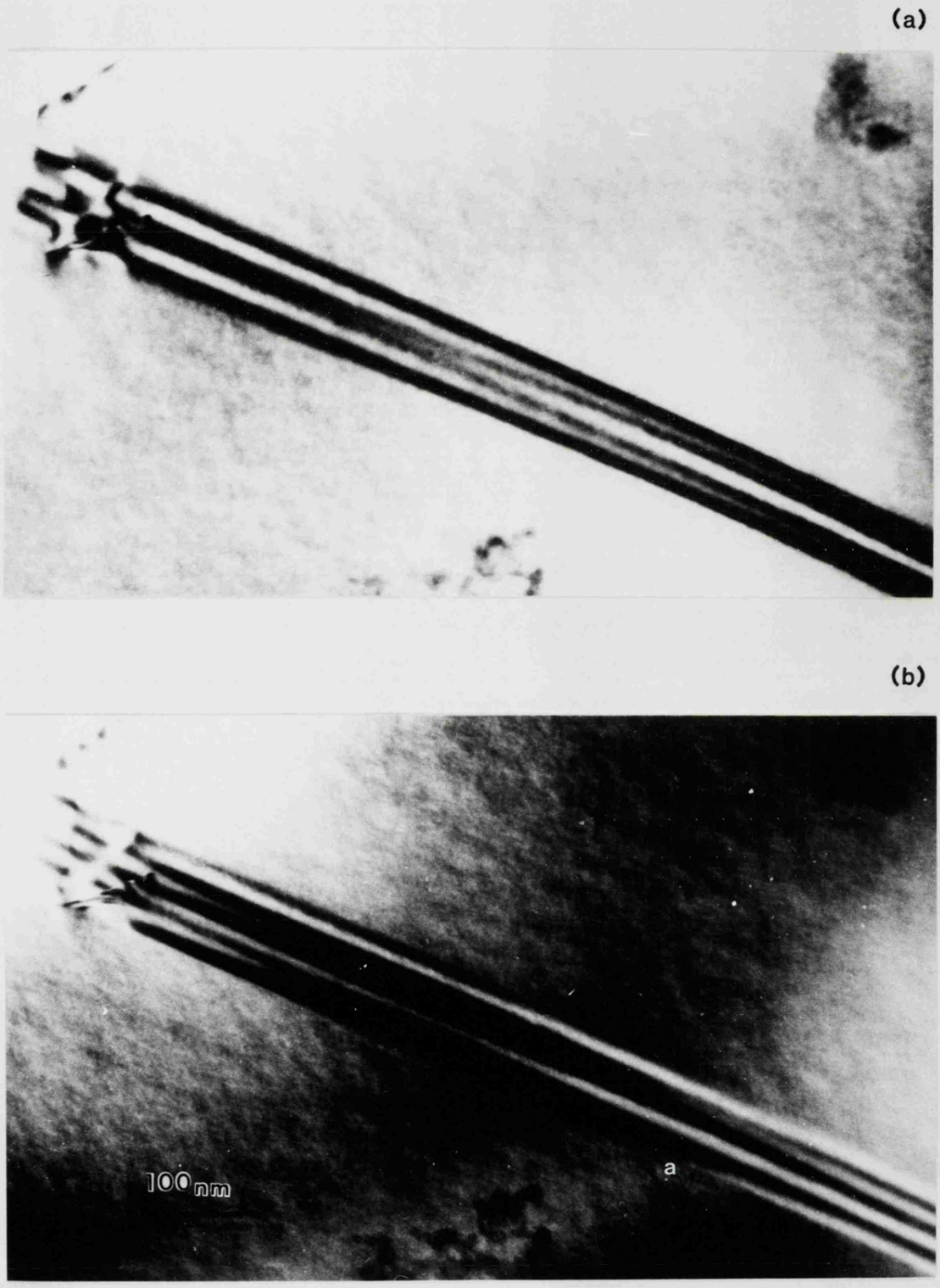

Fig. 21 (a) Bright-field and (b) dark field image of a fault in stainless steel.

Measurement of corresponding widths of the fault in bright field and dark field modes yielded different results for the same fault, the dark field method giving slightly higher readings and hence higher values for thickness. In the region studied dark field image widths were approximately 12% greater than corresponding bright field measurements. Thus, in this particular case, a discrepancy of 12% occurs in thickness values obtained by the different imaging procedures.

On the dark field image the contrast of the outer fringes changes along the length of the fault i.e. contrast appears to vary with foil thickness. At point (a) in Fig. 21 the outer fringe changes from dark to bright and is actually at the background level of contrast and therefore difficult to see. It is thought that in the bright field image all of the outer fringe is at the background level, this accounting for an underestimation of the fault width in this mode. It can be seen from Fig. 22 that the amplitude of the intensity function varies more markedly from an arbitrary background level in the dark field case. It can also be seen that this variation is dependent on the sign of the phase angle α.

Hall and Vander Sande (1975) noticed discrepancies as large as 40% in corresponding bright and dark field image widths of stacking faults in cobalt alloys, with the dark field image giving the higher value. Their work suggested that the image contrast was strongly

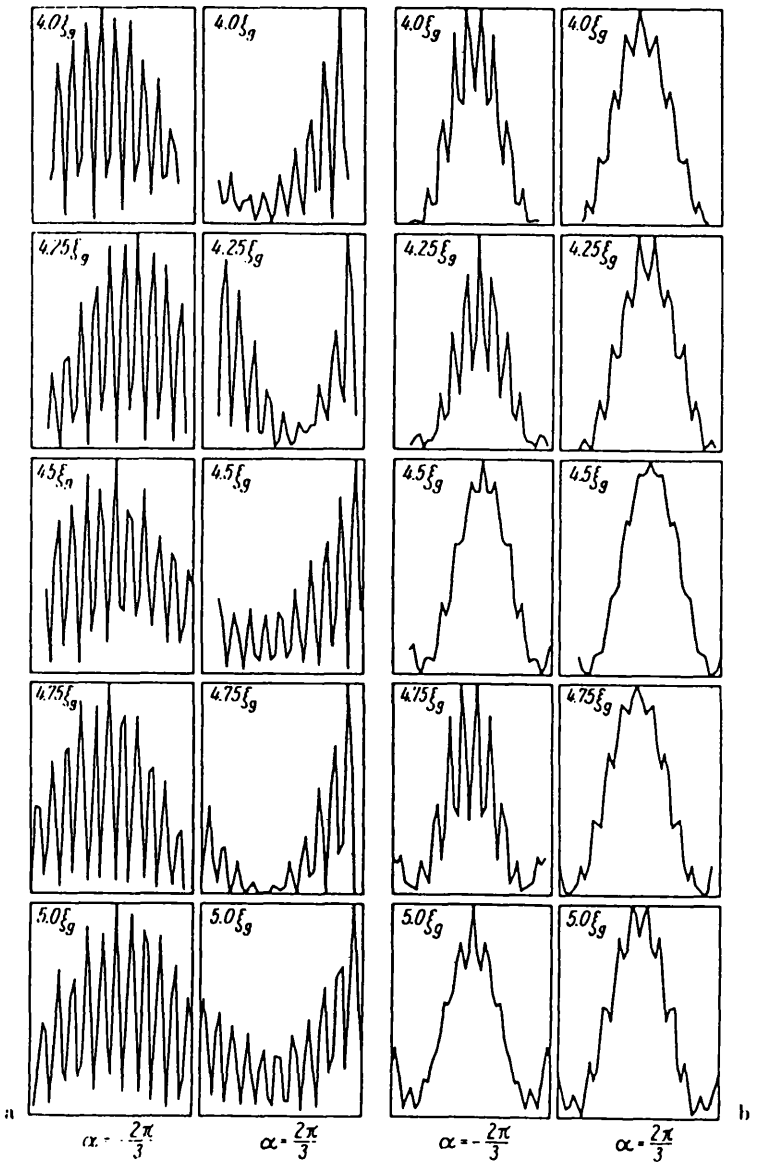

Fig. 22

(a) Computed profiles of D.F. images for $\alpha = \pm 2\pi/3$ when second order reflection conditions are satisfied. The foil thickness varies from 4ξg to 5ξg in 1/4 ξg increments.

(b) Corresponding B.F. image profiles.

(After Chen & Thomas 1974).

dependent upon the deviation parameter s, the extinction distance ξ_g, and the phase angle α. For values of $\omega > 0$, where ω is equal to $s\xi_g$, the width of the bright field image was approximately 75% of the width of the corresponding dark field image but when $\omega \leq 0$ the two image widths were similar with the bright field image width exceeding 90% of the dark field image width in all cases. The work showed this to be the case for foils in the range where $1.0 \leq \frac{t}{\xi_g} \leq 2.0$. In this range of thicknesses the contrast is dependent on ω. For $\omega > 0.4$ and negative phase angle α Hall et al observed dark outer fringes on the fault examined whilst bright outer fringes resulted when $\omega < 0$. Intermediate between these extreme values of ω is a range where the outermost fringes show similar contrast to the background i.e. they become invisible.

Clarebrough and Head (1976) found that this effect occurs over a much wider range of thicknesses than predicted by Hall et al, and that the effect also occurs in dark field imaging but to a lesser extent this being shown in the present work in Fig. 21. True image widths and calculated thickness measurements may therefore be underestimated in both bright field and dark field imaging; the latter however giving a closer approximation to the true value.

Hall and Vander Sande suggest that weak beam dark field micrographs will be most accurate since the intensity deviates most rapidly from background with

depth in this mode. The use of such images is however sometimes impractical as their brightness is very low and photographic exposure times; especially in thick foil region may be unacceptably high. Chen and Thomas (1974) found that contrast of stacking faults using 650 kV electrons was much better than at 100 kV. At this higher voltage the electron wavelenth is less (λ_{650K} = ·0119 Å) and the Ewald sphere radius correspondingly larger. This allows more diffracted beams to contribute to the image and these many beam interactions give rise to better image contrast (Bell and Thomas 1972).

With so many potential sources of error it is unlikely that the method in its present format will be able to provide more than a very rough estimate of thickness. An improved technique, devised to overcome the shortcomings of the above technique, is next investigated. This utilises defects found in many foils to provide accurate thickness values for those foils. It requires no crystallographic analysis and can therefore be used with faults lying on unknown habit planes.

3.3 Fault Tilting Method

For this investigation electropolished samples of copper, aluminium and stainless steel were used. These materials were chosen as this particular technique was later used as a yard-stick by which to judge other techniques of measuring thickness. The

specimens (composition in table 1) were prepared in the usual manner, conditions of electropolishing being given in table 2.

Each specimen in turn was inserted into a goniometer holder capable of providing both eucentric tilt and lateral rotation. A suitable defect was chosen which intersected top and bottom surfaces of the foil. In the present study slip traces and grain boundaries were used but others such as overaged precipitates and incoherent twin boundaries could be used.
Stacking faults and other completely coherent defects were avoided because of the fringe contrast difficulties outlined in the previous section. However such problems could possibly be minimised using this method as images under a variety of contrast conditions are used and values which greatly underestimate the true fault width will be easily spotted.

Upon selecting a suitable defect the sample was rotated until the major axis of the fault lay parallel with the tilt axis. This was achieved by placing a contamination spot (see introduction and section 4) near to the fault. When the correct conditions outlined above were obtained the spots were seen to separate orthogonally to the major axis of the fault as the foil was tilted (Fig. 23).

When the above requirements were met, the fault was tilted through various clockwise and counter clockwise angles. Upon obtaining good contrast conditions

the fault was photographed in the TEM mode and the corresponding angle of tilt and its sense recorded.

The geometry of a fault tilting experiment is shown in Fig. 24. In this instance the foil is shown initially normal to the electron beam although the method is applicable to cases where this is not so.

It can be seen that:

$$\cos\beta = t/l, \qquad \sin\beta = w_1/l,$$

$$\sin(\alpha+\beta) \equiv \sin\alpha\cos\beta + \cos\alpha\sin\beta = w_n/l = \frac{w_n \sin\beta}{w_1}$$

Dividing by $\sin\beta$ and rearranging gives:

$$w_1(\sin\alpha \cot\beta + \cos\alpha) = w_n$$

Now $\cot\beta = \frac{t}{w_1}$ giving $w_1\left(\frac{t}{w_1}\sin\alpha + \cos\alpha\right) = w_n$

and $\therefore \quad t = \frac{w_n - w_1\cos\alpha}{\sin\alpha}$ or $t + w_1\cot\alpha = w_n/\sin\alpha$

A plot of $\frac{w_n}{\sin\alpha}$ versus $\cot\alpha$ is linear and gives the foil thickness t as the intercept on the $w_n/\sin\alpha$ axis. Over a narrow range of tilts ($\pm 20^{o}$) a plot of w_n versus α is linear and may be similarly used to determine the inclination of the fault and the foil thickness. However both plots may produce thickness values in error because of the ambiguity in the foil surface orientation. Although foil thickness measurements are therefore inherently susceptible to error by this approach no such uncertainty is present in the actual fault width l. This parameter can be deduced from such plots with a high degree of accuracy and a

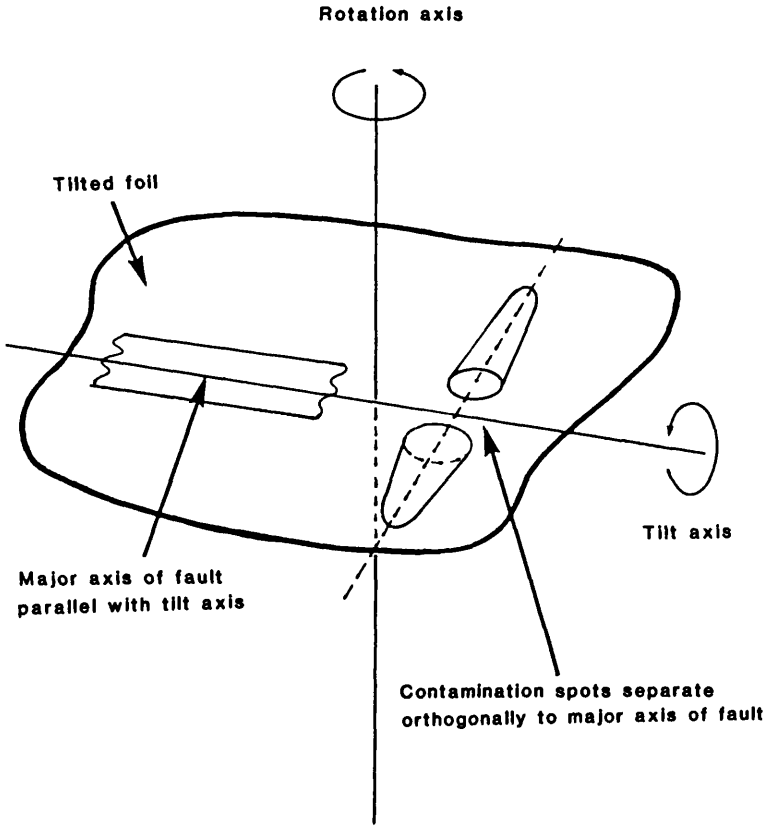

Fig. 23

Obtaining correct orientation conditions for fault tilting technique.

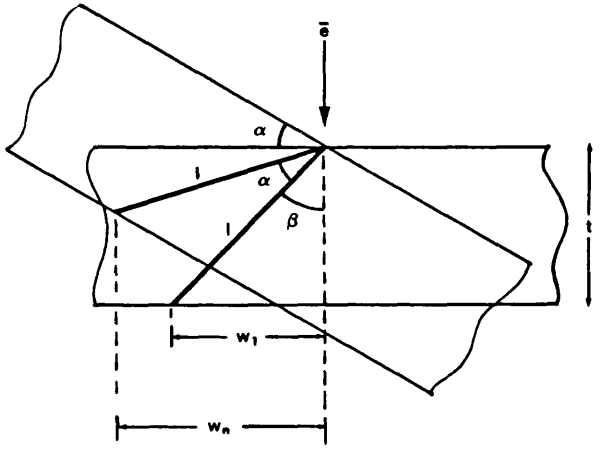

Fig. 24

Geometry of fault tilting experiment.

(Refer to text, page 58, for further information).

Figs. 23 & 24

value of the inclination of the fault with respect to the electron beam may also be obtained. With the fault tilted to the vertical position, l is equal to the thickness in the beam direction.

Figure 25 shows how the beam direction thickness was calculated for a fault in stainless steel. For steeply inclined traces there will be little difference between this value and the actual thickness. It is also the more correct parameter to use in many materials studies. Faults which are not steeply inclined should be avoided for two reasons. Firstly fault width measurements should ideally be made up to 20^{o} on either side of the vertical (zero width) position and the limited tilt restrictions on the goniometer stage make this easier in practice for steeply inclined faults. Secondly, the large tilts required to align a 'flat' fault vertically with the beam may have the unfortunate effect of severely limiting the lateral field of view of a typical wedge specimen. This, shown schematically in Fig. 26, is important because the 'modus operandi' requires any quantitative studies to be made under the same tilt conditions used in obtaining the beam thickness.

The accuracy of this graphical method is very high. Individual non-systematic errors in determining actual fault widths, l, due to less than perfect image contrast or slight ambiguity in the tilt angle, are eliminated.

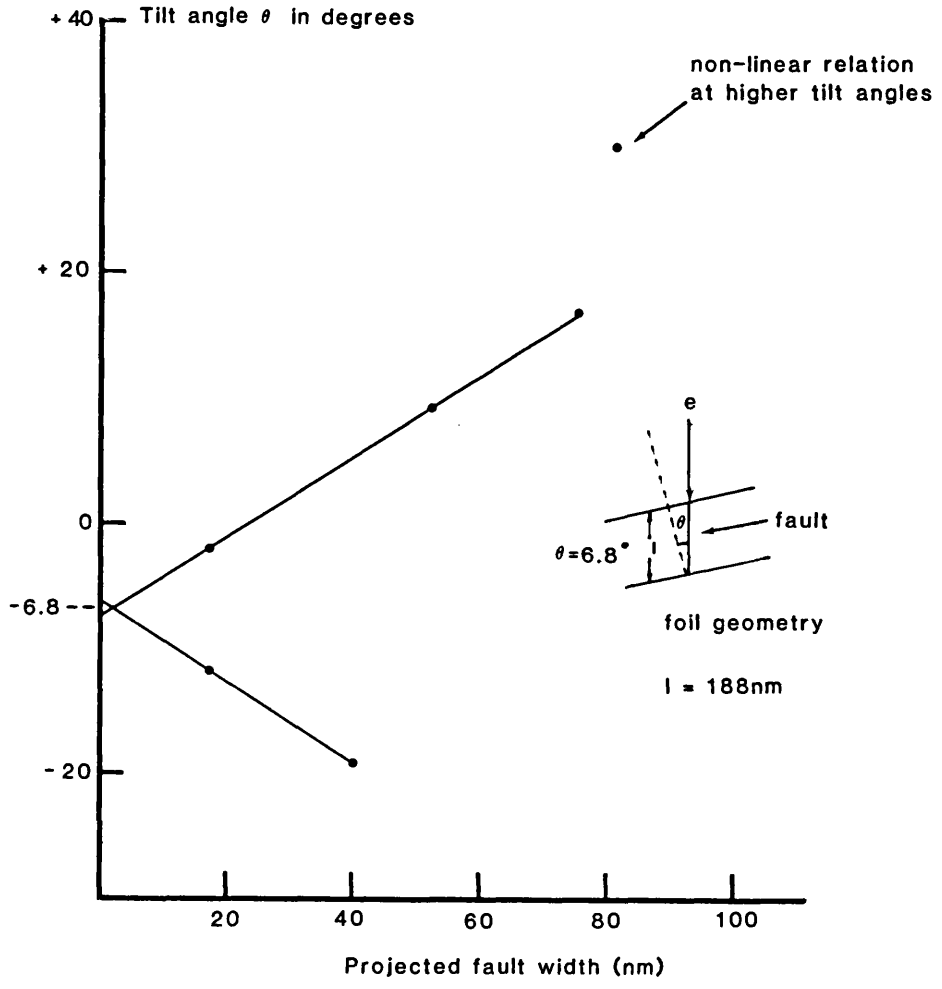

Fig. 25 Thickness determination by tilting fault technique. (Stainless steel foil)

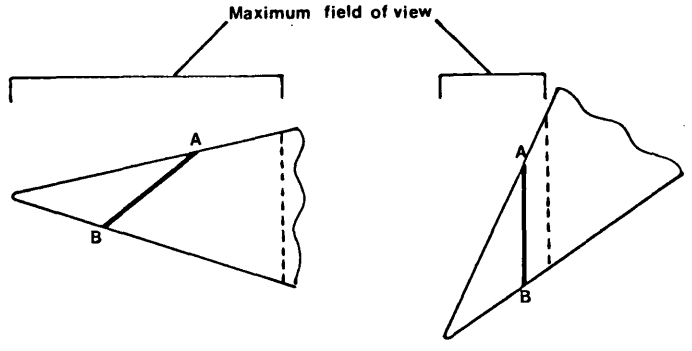

Fig. 26 Restricted field of view on a foil tilted to vertically align a shallow fault.

The fault inclination is known to within ± 0.5° if image widths are measured either side of the vertical position and the position of the foil surface need not be known. Systematic errors consist only of uncertainty in the magnification which is ± 1%. The total possible uncertainty in beam thickness using this method is ∿ 3%.

It was mentioned that the technique was used as a yardstick by which to judge other measuring methods. In order to avoid repetition, the results obtained for the various alloys are omitted from this section but are included in later sections where the technique has been compared with other methods.

4. THE CONTAMINATION SPOT METHOD

4.1 Preparation of Specimens

Specimens were prepared from bulk materials by the electropolishing technique and also using vacuum evaporation.

4.1.1 Thin foils

Specimens of copper, stainless steel and aluminium of composition given by table 1 were prepared for TEM examination using the techniques described in section 3.1. Conditions of electropolishing are given in table 2.

4.1.2 Thin evaporated films

Thin evaporated aluminium films of known thickness were required for part of this study. They were produced using a hot aluminium source in an evacuated chamber and measured by two different techniques, this being described in more detail immediately hereafter.

4.1.2.1 Production

The coatings were produced by thermal evaporation using an Edwards 'Speedivac' coating unit model 12E6 (fig. 27).

Inside the glass dome, connected to a low tension supply was placed a clean tungsten basket containing pure aluminium in the form of coiled wire, Fig. 27a. The sample to be coated was positioned directly above the basket on the underside of a tripod platform. Fig. 27b shows the plan view of such an arrangement. The specimen, which was a stainless steel TEM sample, was attached to the central region

of a set of pre-silvered glass slides. One half of these slides were blanked off by a set of plain glass slides and the whole assembly fixed to the underside of the tripod table using vacuum compatible tape. A quartz crystal oscillator was placed adjacent to the specimen. This was used to monitor the build up of the evaporated film and is described in detail in 4.1.2.2.

The system was evacuated to better than 10^{-4} Torr and the current was then carefully increased through the tungsten basket. As the heating effects of the current became more pronounced the aluminium eventually melted and subsequently started to evaporate. The current was further adjusted until the rate of deposition, as measured by the quartz crystal monitor, was $\approx$ 1nm. s^{-1}. The evaporating metal condensed on the surrounding surfaces and gradually increased in thickness. When the specified thickness was reached, the electric current was switched off and the chamber allowed to cool for ten minutes. This reduced the oxidation rate of the fresh metal when air was finally admitted. Subsequent to letting the apparatus down to atmospheric pressure the specimen and glass blanking slides were removed. The silvered slides, now coated with aluminium on one side of a sharp step, remained in the chamber and were further coated by the same technique with a thin covering of silver ($\approx$ 100nm). The TEM specimen was removed to the electron microscope as soon as possible and was kept in a vacuum dessicator when not being examined.

4.1.2.2 Measurement of thickness

The thickness of the evaporated film deposited on the TEM specimen was required. The brightly glowing molten aluminium in the tungsten basket is analogous to a light source. In the latter case the intensity of the light at any point in space is proportional to d^{-2} where d is the distance of that point from the source. Similarly the distribution of the evaporated aluminium atoms follows a similar rule. Hence the thickness of film deposited on the specimen can be deduced by measuring film thicknesses from surrounding areas and extrapolating these results.

The thickness of the aluminium film on the pre-silvered glass slides was measured at known distances from the position of the specimen using MULTIPLE BEAM INTERFEROMETRY.

Multiple beam interferometry

The aluminium coated glass slides are shown schematically in Fig. 28. The glass slide is covered with a silver layer approximately 100nm thick. This provides a substrate similar in nature (metallic) to the stainless steel TEM specimen. The aluminium layer deposited onto half the silvered slide was estimated to be approximately 170nm thick by the quartz crystal monitor. This in turn was coated by a second ($\approx$ 100nm) layer of silver.

The top silver layer provides a uniform, highly reflecting layer on either side of the stepped surface.

Fig. 27

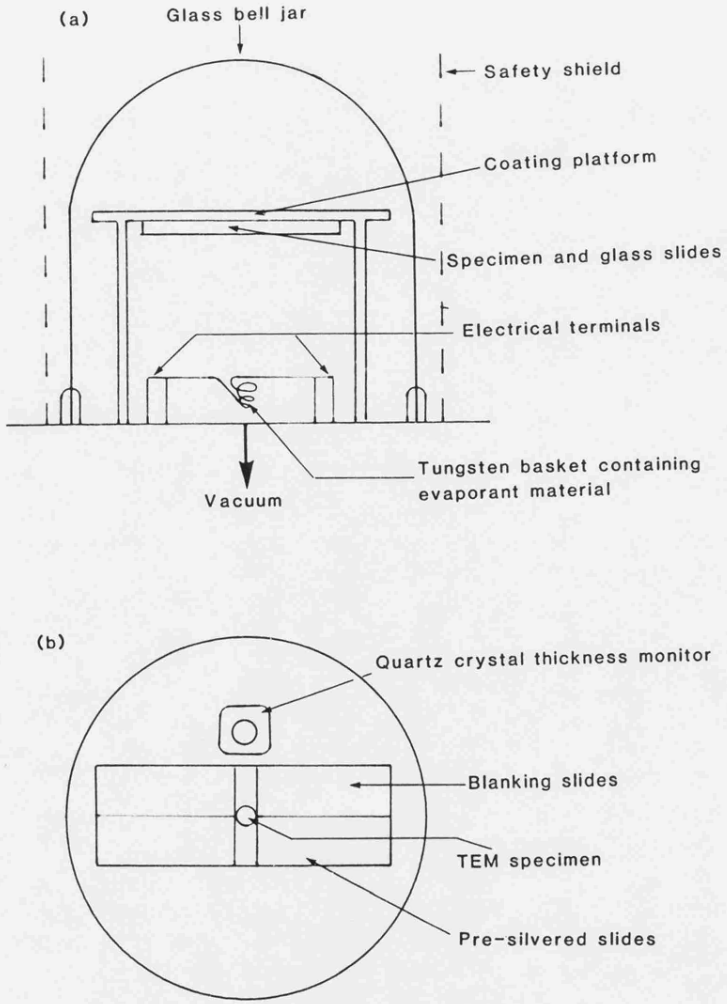

Fig. 27 (a) cross-section of coating chamber

(b) plan view of specimen platform

Fig. 28

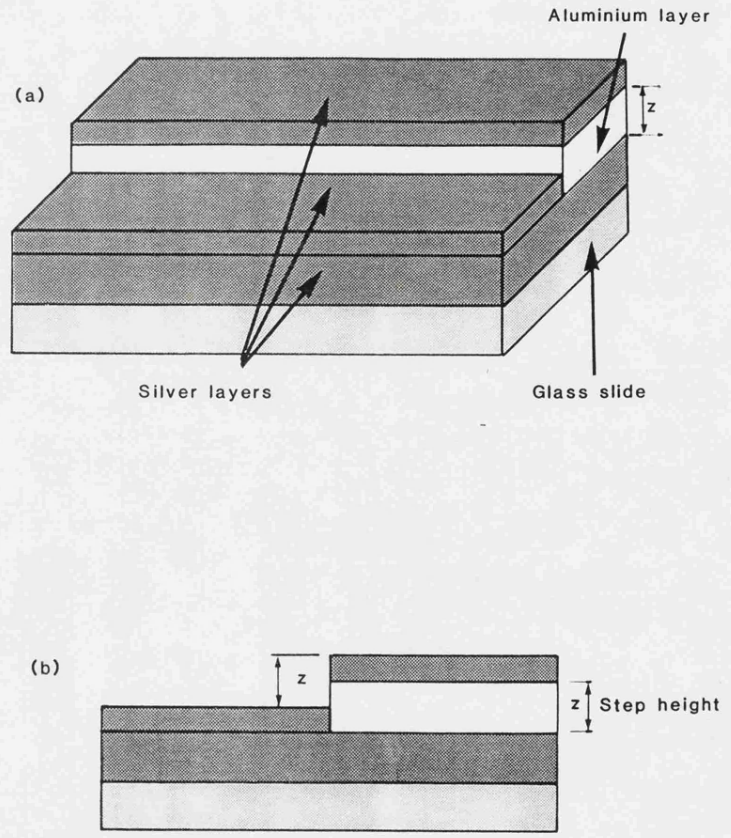

Fig. 28

Structure of evaporated films used in interferometry measurements.

(a) three quarter view

(b) cross-section

Tolansky (1948) has shown that such surfaces follow the contours of the substrate with a very high degree of precision which is accurate even on an atomic scale. Thus the step height Z remains the same after this coating as before. The advantages of adding this layer are three fold. Firstly the surfaces either side of the step have the same refractive index and there will consequently be no phase change in light reflected from either side. Such phase changes, when they occur, can affect interferometry readings and lead to erroneous thickness values. Secondly any oxidation of the surface will be minimal and equal on either side of the step and Z will therefore remain constant, whereas with dissimilar materials, e.g. silver-aluminium, differential oxidation rates could lead to the value of Z changing over a period of time. Finally, the highly reflective surfaces increase the intensity of higher order reflected beams which then take part in the resultant interferogram. This has the effect of narrowing the width of the dark fringes thus making measurement easier and more accurate.

The multiple beam interferometry method of determining the step height, and hence the thickness of the aluminium layer is shown in Fig. 29. A semi-silvered optical flat rests on the stepped surface of the slide such that a small angle (θ) is made with the horizontal. This assembly is illuminated from above by a sodium lamp producing monochromatic light with a wavelength λ of 589.3nm. Rays reflected from the surface of the

Fig. 29

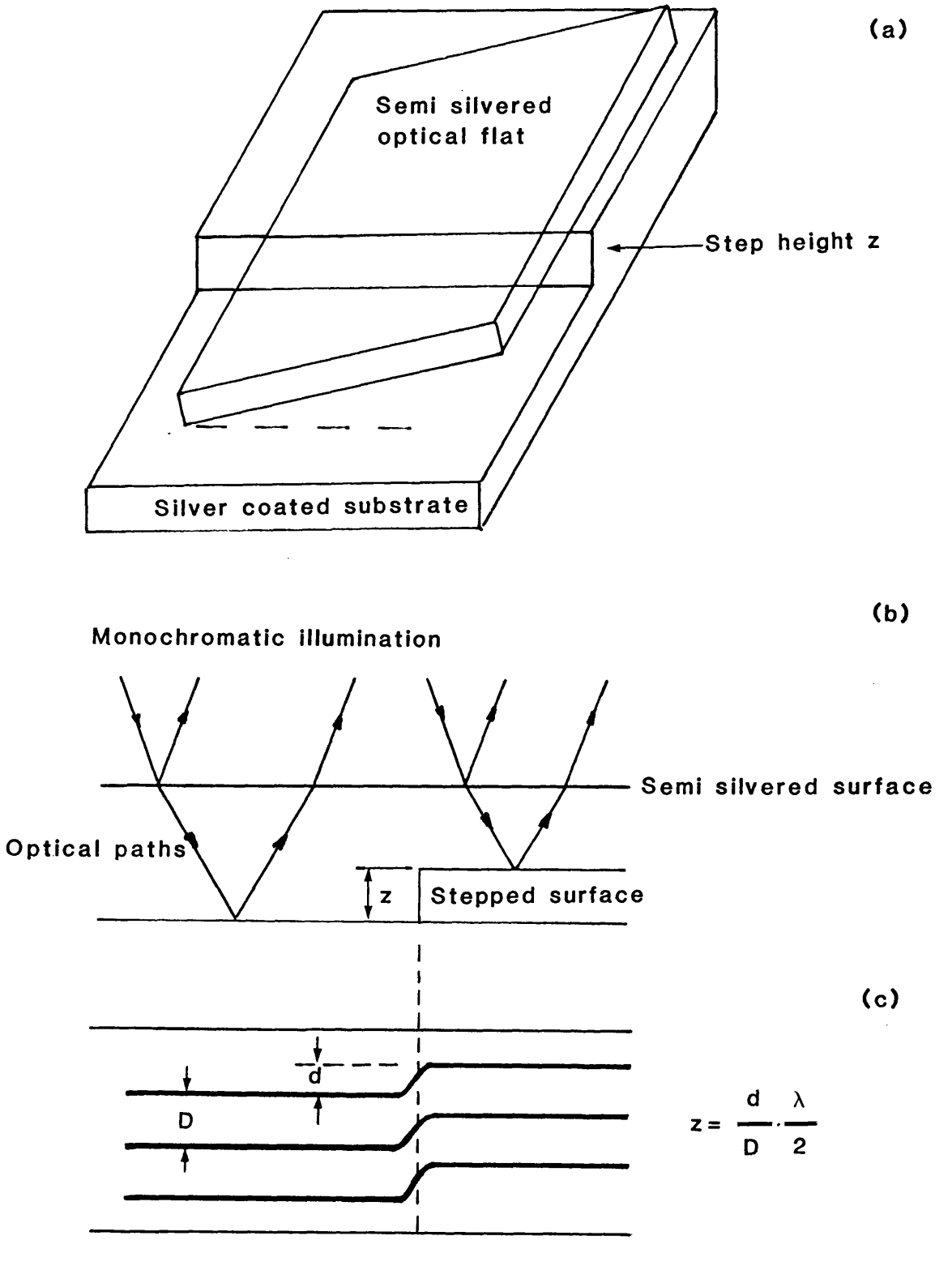

Fig. 29 The measurement of coating thickness by interferometry.

specimen and the base of the semi-silvered optical flat interfere. When the difference in total optical path length is $\frac{n\lambda}{2}$, where n is an odd integer, destructive interference occurs. For an optically flat specimen this results in alternate bright and dark parallel fringes, the inter-fringe spacing, D, corresponding to a height increment of $\frac{\lambda}{2}$. For a stepped specimen the fringes will be displaced either side of the step by an amount d and the step height can be calculated from

$$Z = \frac{d}{D} \cdot \frac{\lambda}{2} \qquad 4.1$$

The step height was measured at various points up to 11cm from the position of the TEM specimen. It can be seen from Fig. 30 that a plot of $Z^{-2/3}$ versus R^2, where R is the distance of the thickness measurement from the stainless steel specimen, is theoretically linear. Fig. 31 graphically displays the experimental results, the intercept on the ordinate giving a thickness value of 175 ± 5nm. Each point on the curve is the mean of eight values, these being given in table 3

Figure 32a shows a typical multiple beam interogram for a step height of 209nm. Tolansky (1948, 1955 and 1960) has claimed that shifts of 1/250 of a fringe may be detected and that individual step heights may be accurately measured to within ± 1 - 2nm. However the microscopic surface roughness present on films in this study was such that individual values lay within μ ± 10nm (1 SD) while the same degree of confidence in their means made these values accurate to approximately ± 3.5nm. Special

Fig. 30

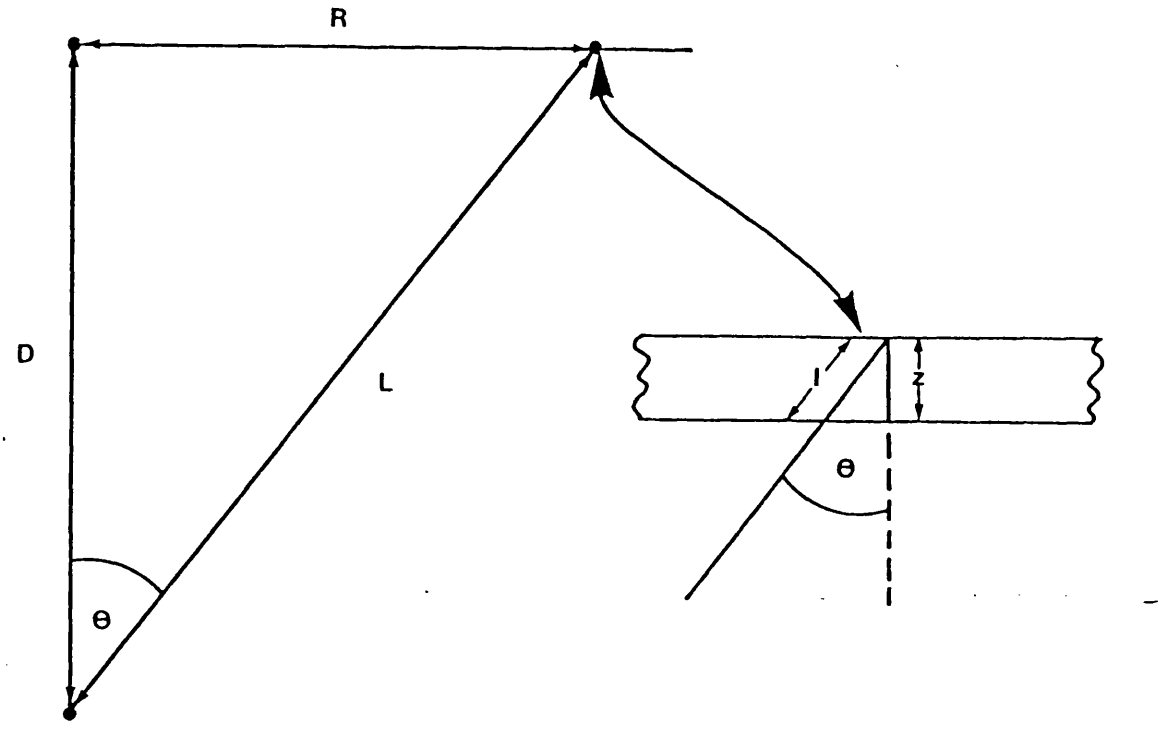

Fig. 30 Coating thickness at a distance R from the TEM specimen.

D = Vertical distance between aluminium source and TEM specimen

R = Distance of thickness measurement from TEM specimen

$l \propto L^{-2} = (D^2+R^2)^{-1}$ and $z = l \cos\theta = \frac{lD}{L}$

$\therefore z \propto \frac{\cos\theta}{(D^2+R^2)}$ or $\frac{D}{L(D^2+R^2)}$

Now $L = (D^2+R^2)^{\frac{1}{2}}$

$\therefore z \propto \frac{D}{(D^2+R^2)^{3/2}}$ i.e. $z^{-2/3} \propto \frac{D^2+R^2}{D}$

Now D is constant $\therefore z^{-2/3} \propto R^2$

Fig. 31

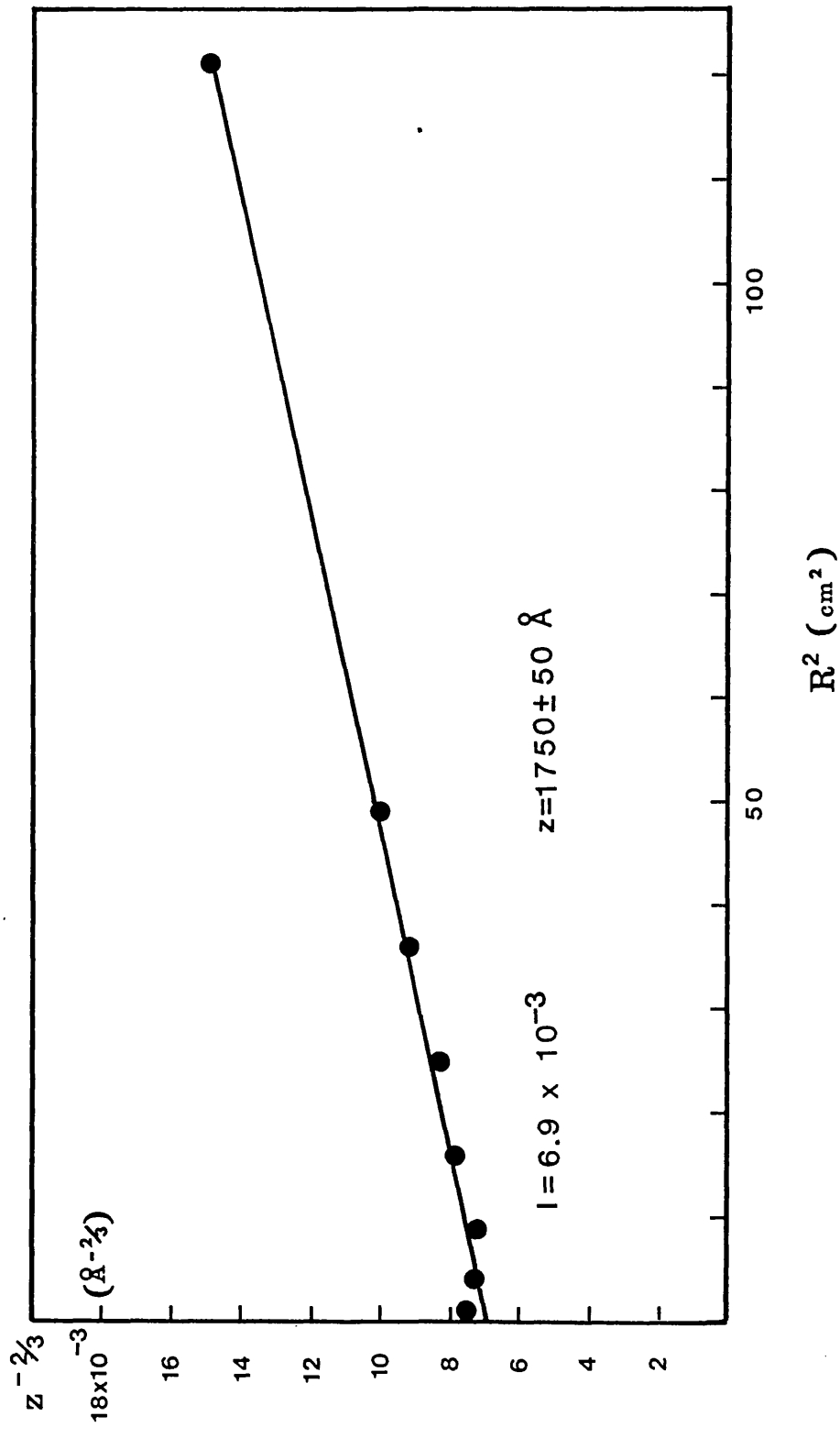

Fig. 31 Thickness determination of aluminium layer on a stainless steel TEM specimen by an interferometry technique.

	Distance from TEM specimen (cm)							
Thickness of deposited film (nm)	1	2	3	4	5	6	7	11
	139.5	176.7	166.1	143.3	143.0	114.0	104.5	62.7
	139.5	181.2	166.1	147.25	139.1	118.8	96.5	65.4
	147.25	171.8	159.2	155.0	129.9	120.0	99.7	65.4
	151.0	154.6	155.0	143.7	129.9	110.1	101.4	61.4
	158.0	143.3	155.0	122.7	134.6	115.0	101.6	56.4
	170.5	147.25	159.2	119.4	130.9	117.6	96.3	57.6
	167.15	158.6	159.2	132.5	126.2	114.3	98.7	35.1
	162.75	158.6	155.0	151.5	122.7	111.8	107.0	32.7
μ	154.5	161.5	159.4	139.4	132.0	115.2	100.7	54.6
σ	12.0	13.8	4.6	13.2	6.6	3.4	3.5	13.2

Table 3. Interferometry thickness data for a deposited aluminium film.

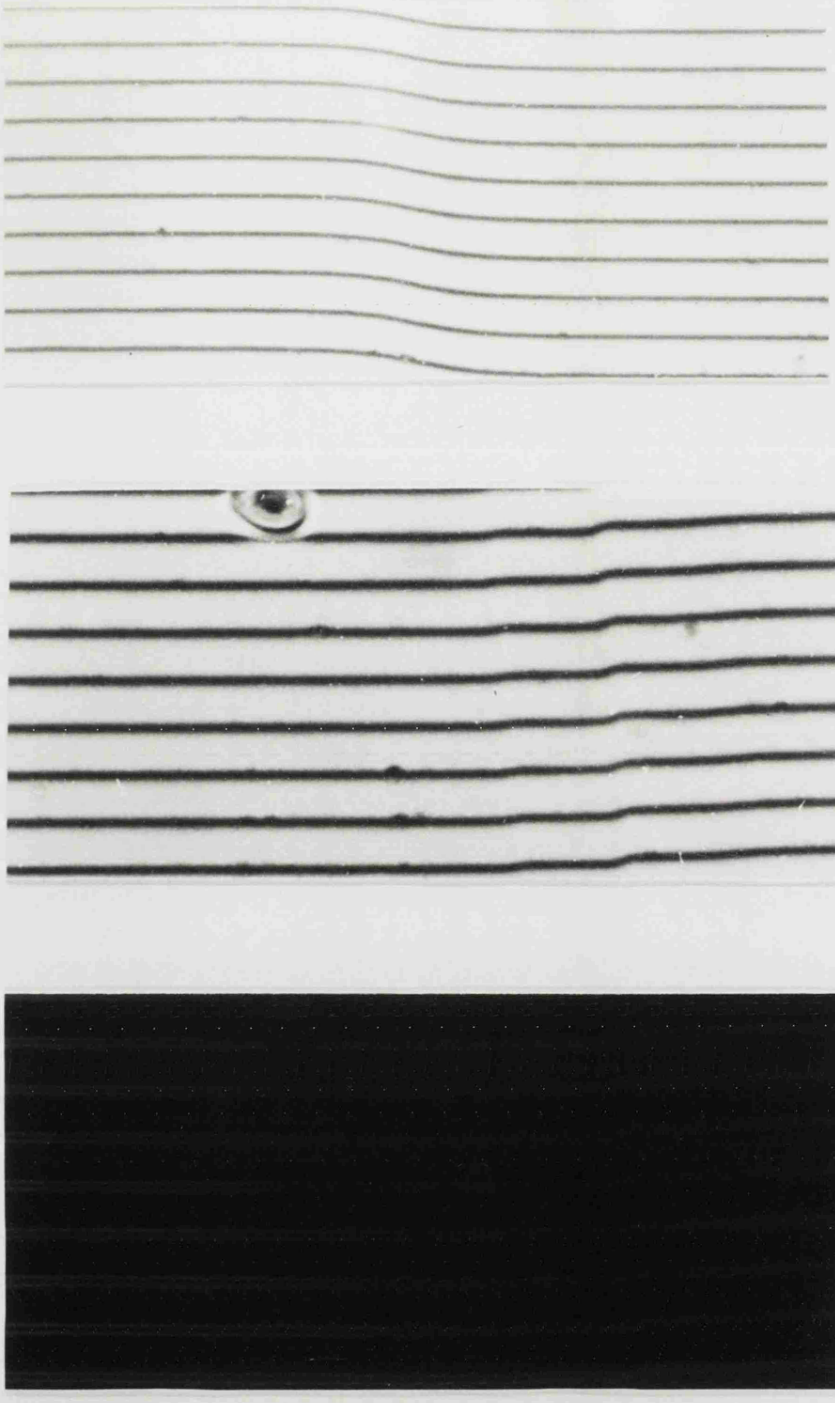

Fig. 32 (a) A typical multiple beam interferogram

(b) & (c) Sabattier technique for obtaining improved contrast Print initially correctly exposed , partially developed and then re-exposed

techniques of image enhancement may be employed in the darkroom to provide better images. These include the Sabattier technique (1980) which separates the single dark fringes into two thinner ones while reversing the contrast as well. This is shown in Fig. 32b and 32c but the technique is recommended only when extreme precision is required from a single interferogram as the method is time consuming and not always successful.

Quartz Crystal Film Thickness Monitor (F.T.M.)

When alternating current is applied to a quartz crystal, thickness shear oscillations are induced in the crystal with a frequency inversely proportional to its thickness. This phenomenon is exploited by the film thickness monitor (F.T.M.) where the frequency of an encapsulated control crystal is compared with that of a similar crystal in a coating unit. As evaporated material condenses on the crystal in the coater, its resonant frequency is reduced, this reduction being a function of the mass and hence thickness of the deposited material.

In the unit used (Edwards F.T.M.2) the frequency of the monitor crystal (6.0 MHz when uncoated) is mixed with that of the reference crystal (6.5 MHz) and the difference frequency then mixed with a variable oscillator to produce a final frequency of between 0 and 150 KHz. The drop in monitor crystal frequency is given by:

$$\Delta f = \frac{N \Delta M}{P_q t_q A_m} \qquad 4.2$$

where M = the deposited mass

A_m = the area of deposition

P_q = the density of quartz ($2.65 g/cm^3$)

N = a constant equal to 1.67×10^6 Hz mm and

t_q = the quartz crystal thickness in mm.

If the density of the evaporant is known the frequency drop of the quartz crystal can be calibrated directly in thickness units. To this purpose a density control is included in the Edwards apparatus.

In the experiment to deposit aluminium on the stainless steel sample the FTM was placed to one side of the specimen. The density control was set to 2.7 (the specific gravity of bulk aluminium) and a film of 170 nm was deposited. This figure, it must be stressed, was only an approximate guide to the thickness of the specimen which was more accurately determined by interferometry. The very close agreement between the two data is probably somewhat fortuitous. Errors in the thickness value may arise because the FTM and the specimen to be coated are not equidistant from the source, the thin film and bulk density of the material may be slightly different and, finally, increases in temperature of the FTM may alter the frequency of the crystal. The first and last factor may be minimised by placing the FTM and specimen close together and as far from the source as possible. Smaller tungsten baskets containing less aluminium will produce less heat.

Differences between thin film and bulk densities may cause systematic errors. These can be removed by calibrating the F.T.M. by another technique such as multiple beam inferometry. In this case the density control is kept in its fully clockwise position and the direct reading compared with step heights on glass slides. For greater accuracy care must be taken to ensure the slides and FTM are equidistant from the source.

4.2 Effect of Deposition Conditions on Contamination Spot Morphology

To produce contamination spots on a TEM specimen the area of interest is focussed in the STEM mode and the scanning coils turned off. This results in a fine stationary beam impinging on the specimen causing a rapid build up of contamination on top and bottom surfaces.

Foil thickness is proportional to the projected distance between the top and bottom contamination spots on a tilted foil. Clearly to obtain maximum precision in thickness values, optimum contrast of the spots and unambiguity in the measurement end points is required. The shape and size of the spot will be a function of the deposition time and the intensity of the electron beam reaching the specimen (specimen current), while the contrast of the spots could vary with substrate composition and thickness.

To optimise spot clarity and thus measurement precision, the effects of specimen current and

deposition time have been investigated. The effect of foil thickness and substrate composition on the spot morphology and its accuracy is revealed by comparing thickness measurements obtained by this method with those from the 'yard stick' tilting fault method, this being done on foils of different compositions.

4.2.1 Specimen Current

The current of a fine STEM probe was measured for various instrument settings with a Faraday cage occupying the normal specimen position. Table 4 shows how the various settings affect this parameter. The readings were repeated on several occasions over a period of time (once a week for 3 weeks), ensuring that the microscope was initially correctly aligned and that aberrations and astigmatisms were minimised prior to measurement. The current was found to be reasonably stable over this time scale, fluctuating by approximately ± 5% from the mean value.

The specimen (stainless steel, composition table 1) produced by the normal electropolishing techniques, (table 2) was focussed at a medium magnification (50K) in STEM mode. The scanning coils were de-activated for ninety seconds and the resulting contamination spot was then photographed in the zero tilt and tilted positions. The procedure was repeated for a range of pre-calibrated currents.

The spot shape and size varied markedly with current. At low currents the spots had a needle like appearance,

INSTRUMENT SETTINGS				SPECIMEN CURRENT (nA)
Condenser Aperture	Objective Aperture	Diffraction Aperture	Spot Size Setting	
STANDARD RESOLUTION				
0	0	1	Large	1.216
0	0	1	Small	0.580
1	0	1	Large	0.384
1	0	1	Small	0.201
2	0	1	Large	0.188
2	0	1	Small	0.091
3	0	1	Large	0.051
3	0	1	Small	0.026
4	0	1	Large	0.019
4	0	1	Small	0.009
HIGH RESOLUTION				
0	0	1	Large	0.57
0	0	1	Small	0.29
1	0	1	Large	0.181
1	0	1	Small	0.098
2	0	1	Large	0.088
2	0	1	Small	0.047
3	0	1	Large	0.025
3	0	1	Small	0.013
4	0	1	Large	0.009
4	0	1	Small	0.004

Table 4. Specimen Currents for various instrument settings. (Voltage = 100kV, Beam current = 100μA, Magnification = 50K).

but gradually adopted a more hemispherical appearance as the current was increased, Fig. 33. The apparent volume of the spots was determined by assuming them to be cone frustrums surmounted by hemispheres (Fig. 34). The trend revealed in Fig. 35 shows an apparently decreasing level of contamination as current increases. This however is not considered to be a real effect. The spots deposited at higher currents essentially consist of a 'hump' superimposed on a surrounding thin aureole of contaminant, with only the volume of the 'hump' being easily measureable. The extent of lateral spreading of the aureole is uncertain. It gradually becomes thinner as it spreads and may become so thin that a lack of contrast renders it invisible in the TEM. Evidence backing this hypothesis is shown in Fig. 33 (c) and (d) which shows a spot deposited at 9×10^{-10} A before and after tilting through 45^{o}. Note the halo of contaminant encircling the central spot.

Wall (1980) showed that for a rastering electron probe the volume of contaminant remained constant as beam current was varied. Such a rastering beam can be described as producing an infinite number of individual contamination spots. In this situation any individual 'halos' become combined in a layer which then contributes to the volume measurement. Another consequence of this 'constant volume' approach is that the thickness of any contaminant is proportional to the inverse square of the electron probe radius i.e. the height of the contamination needles in this experiment should decrease with increasing

Fig. 33

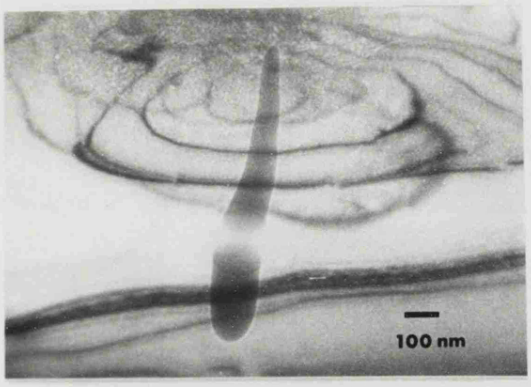

(a) $I = 0.63 \times 10^{-10}$ A

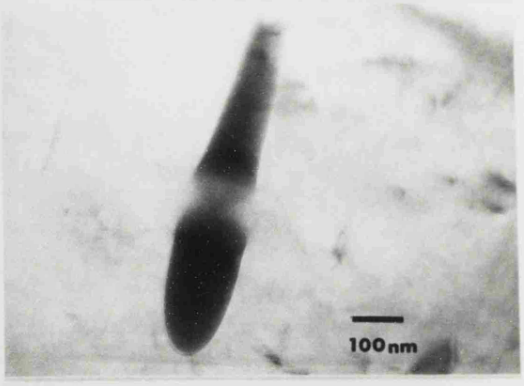

(b) $I = 2.76 \times 10^{-10}$ A

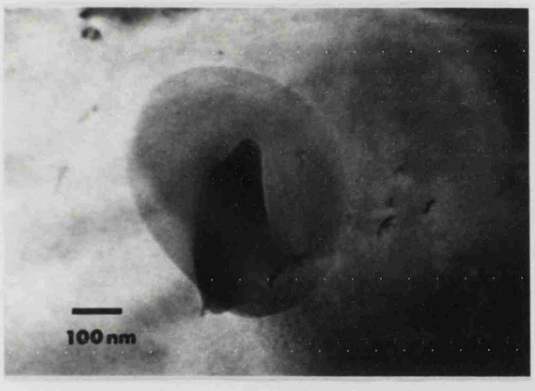

(c) $I = 9 \times 10^{-10}$ A

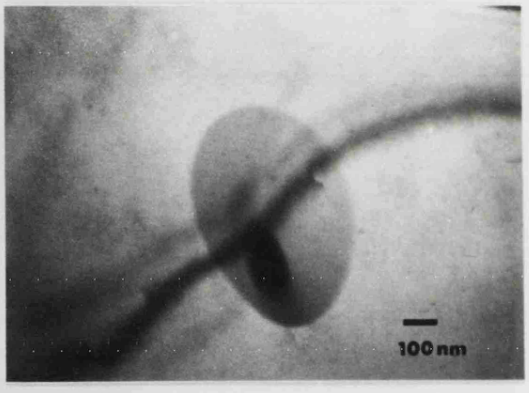

(d) as (c) but at zero tilt

Fig. 33 Effect of specimen current on spot profile.
Spots at 45° tilt unless otherwise stated.
Deposition time 90 seconds.

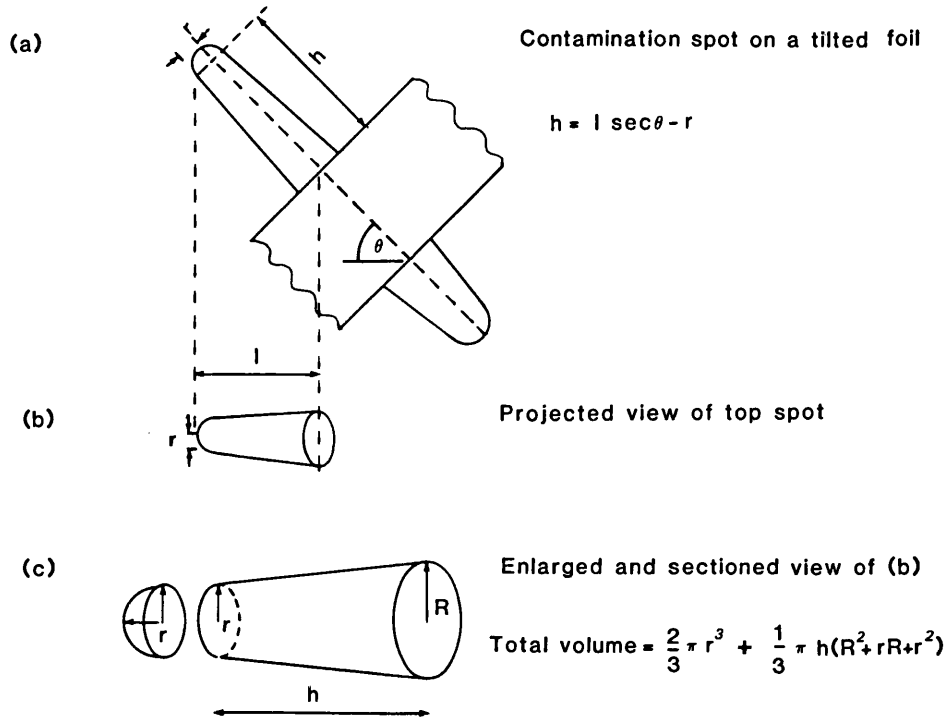

Fig. 34 The determination of spot volume from the projected image of a tilted spot.

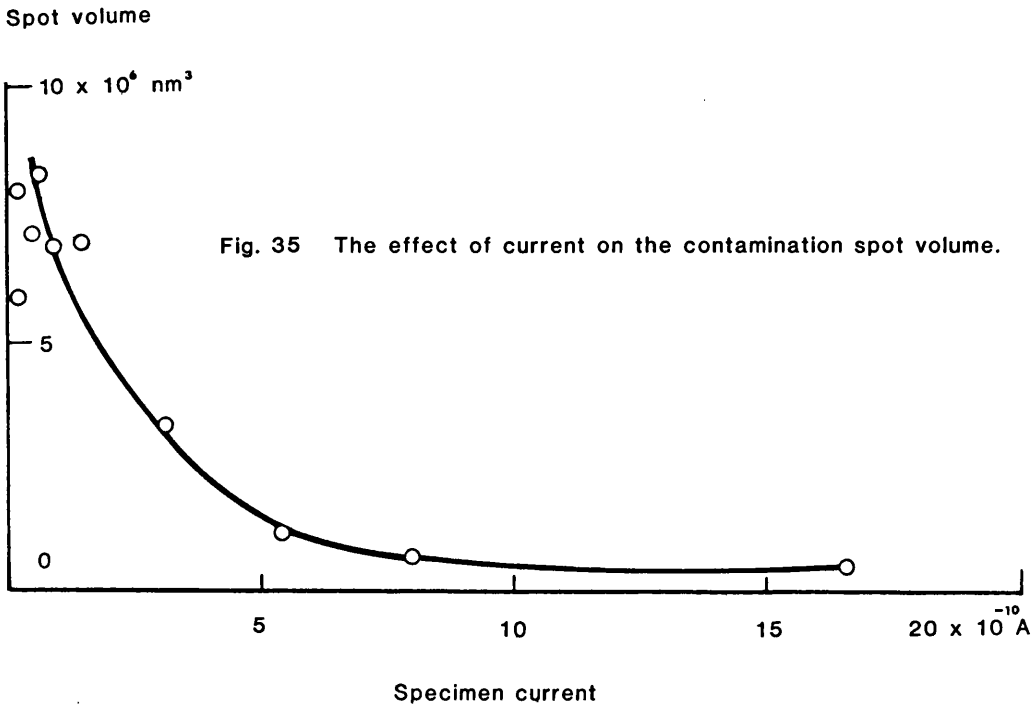

Fig. 35 The effect of current on the contamination spot volume.

current. This did occur, as can readily be observed in Figs. 33 and 36 . It has also been postulated that very low specimen currents may be unable to polymerise all of the incoming contaminant molecules, causing contamination cones to diminish in size below a certain threshold current.

The spots exhibiting optimum growth rates and least ambiguous contrast occurred at low to medium specimen currents ($< 5 \times 10^{-10}$A). Above this value the spots became ill-defined and the increasing 'halo' effects made the exact intersection of the spot and the specimen surface uncertain. This could of course lead to errors in any foil thickness determination.

4.2.2 Deposition Time

From the previous experiment it was concluded that a specimen current of $\approx 2.0 \times 10^{-10}$A produced contamination spots that grew rapidly and had a clear profile, both properties being pre-requisites for fast and precise analysis. All subsequent contamination spots were deposited at this current.

Spots were formed on a stainless steel foil, the time of deposition varying from a few seconds to many minutes. The micrographs in Fig. 37 qualitatively display the resultant changes in spot size and shape. The change in volume of the spots with time is shown in Fig. 38. It is apparent that the contamination rate is approximately linear.

Spots with the optimum profile and contrast are

Fig. 36 The variation of spot height with current.

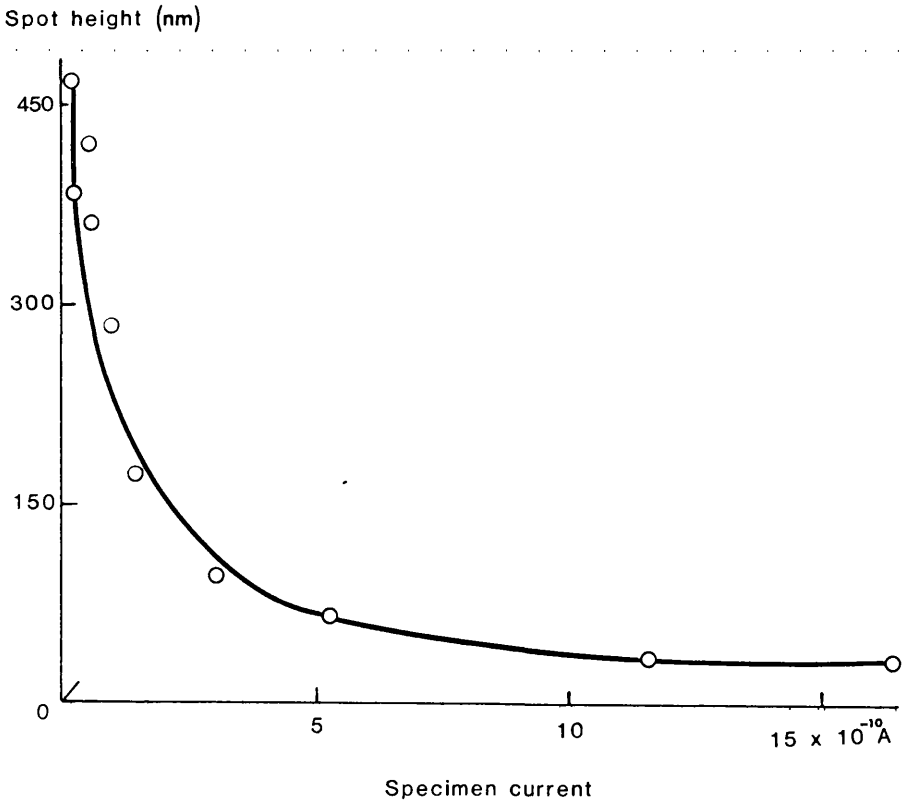

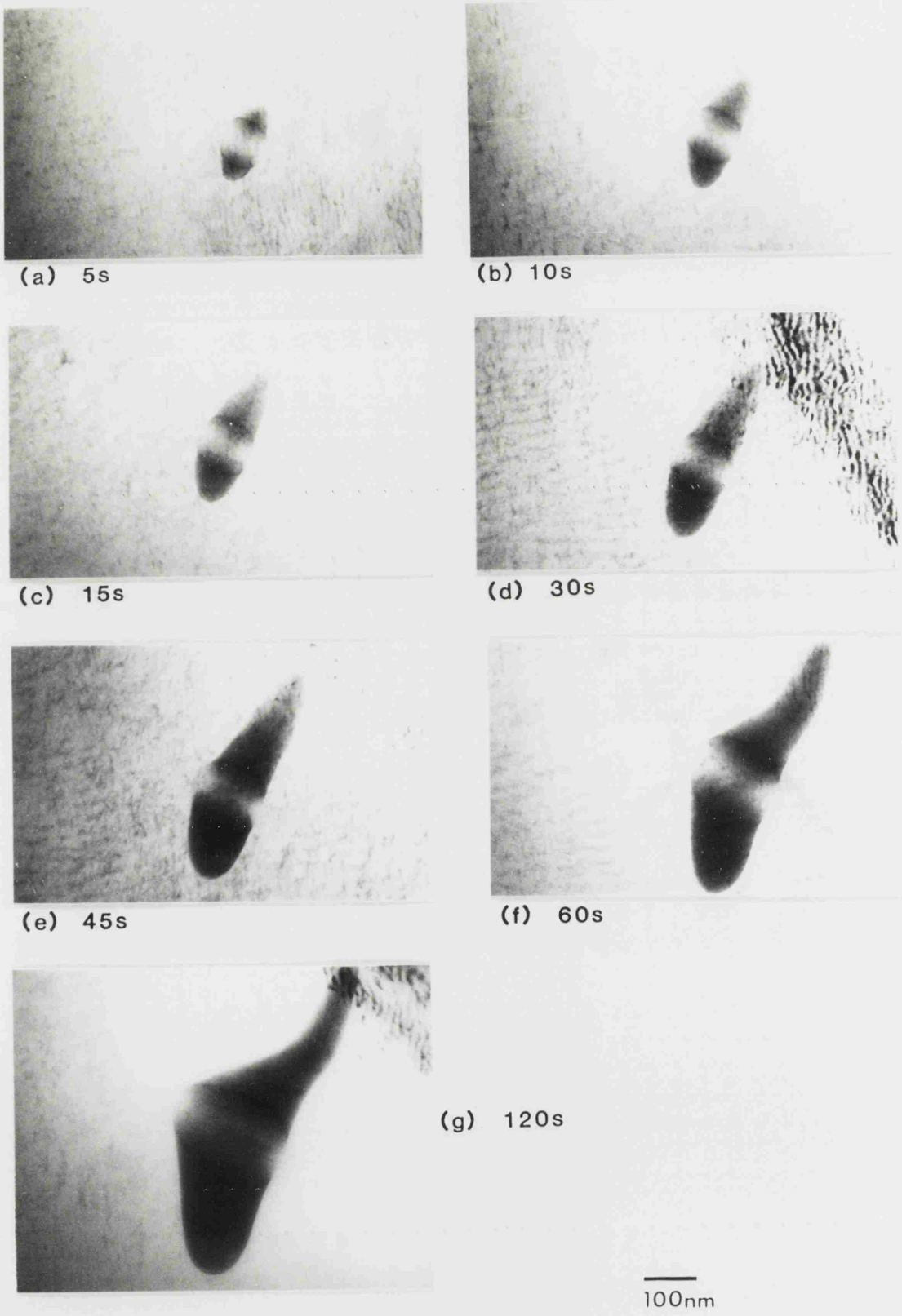

Fig. 37 Effect of deposition time on spot profile, ($I = 2 \times 10^{-10}$ A).

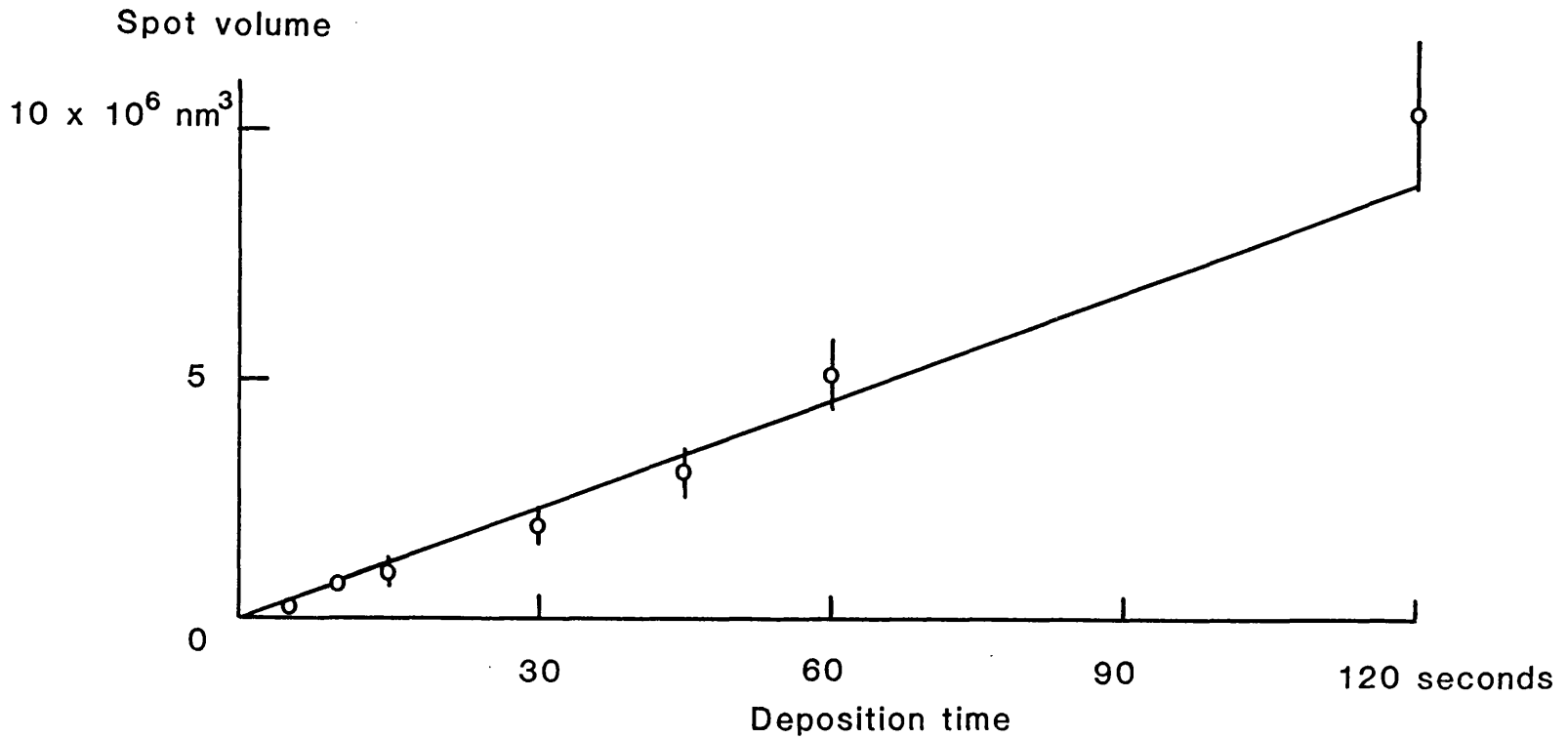

Fig. 38 The variation of contamination spot volume with deposition time.

Fig. 38

produced in times of less than one minute. Over longer periods the shape becomes rather unwieldy. The lateral spreading of the spot base means that spot separation at low foil thicknesses is less well defined than for smaller spots.

4.3 The Comparison of the Contamination Spot Technique and Tilting Fault Method

The tilting fault method, described in section 3.3 was used as an accurate method by which to assess the accuracy and precision of the contamination spot technique.

4.3.1 Contamination Spot versus Tilted Fault in Stainless Steel.

Stainless steel specimens of composition given in table 1 and containing slip traces were electropolished under condit ions outlined in table 2. Using the approach given in section 3.3 the TEM specimen was rotated until the major axis of a slip trace lay parallel with the goniometer tilt axis (see Fig. 23 in section 3.3). The slip trace was then tilted until it was parallel with the electron beam. This was achieved to a high level of accuracy using the graphical technique of section 3.3. With the trace in this parallax position a row of contamination spots was deposited along the line of the slip trace using optimised deposition conditions ($I_{spec} = 2 \times 10^{-10}$A and $t_{dep} = 30$ seconds). The foil was then tilted through an angle θ until the separated spots and slip trace were in good contrast. Fig. 39 shows this sequence of events schematically. The width

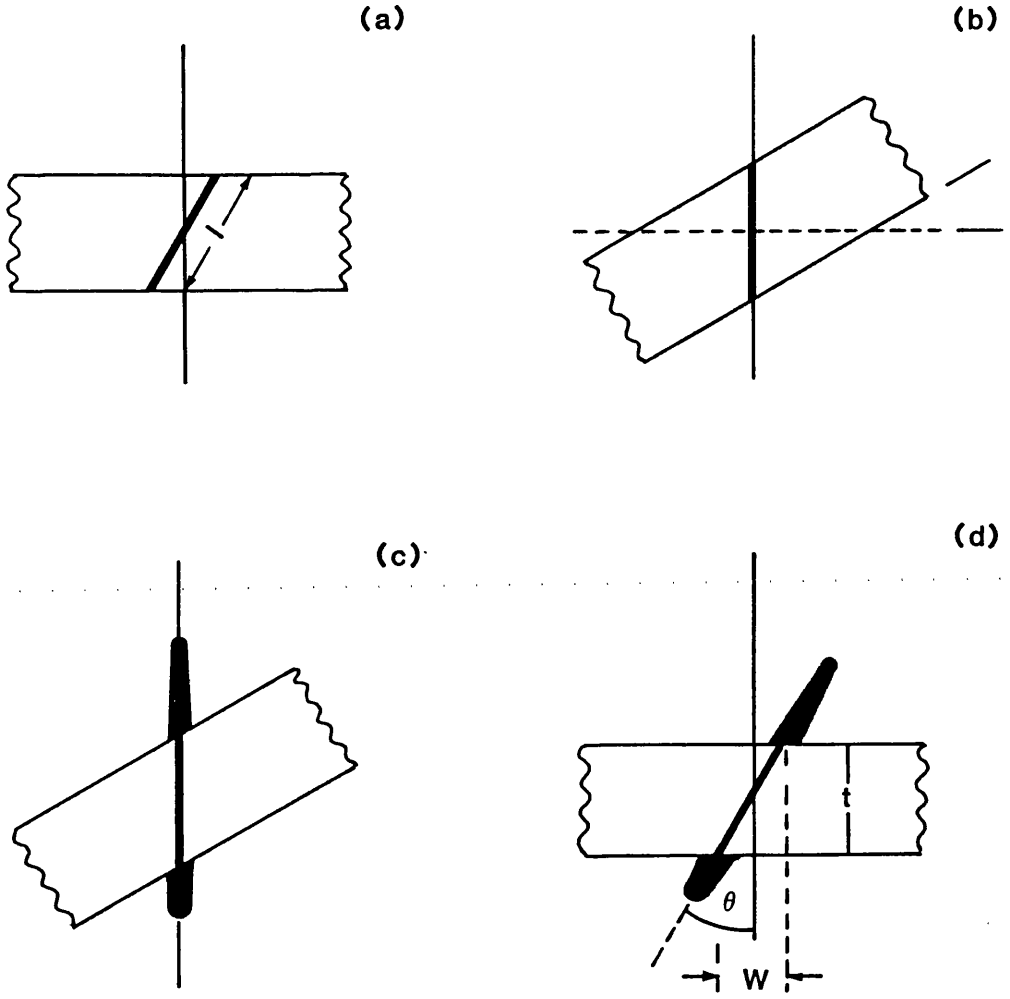

Fig. 39

Comparison of contamination spot method with slip trace technique:

(a) slip trace rotated until parallel with tilt axis of goniometer stage

(b) foil tilted so that slip plane is parallel to electron beam

(c) as (b) and contamination spots deposited

(d) foil tilted back through measured angle θ .

Width of slip plane trace l = W cosec θ

of the slip trace, l, is given by W cosec θ where W is the projected fault width. The separation of the contamination spots gives a second determination which should also correspond to l.

Fig. 40 is taken from a stainless steel foil containing a slip trace. The pair of contamination spots were produced upon the slip trace when in its parallax position, and in the electron micrograph the foil is tilted 35^{o} from this position. The measurement required from the contamination spots is the distance between the tips of the cusps i.e. between the lines XX' and YY' in the micrograph . Clearly this gives a value in excess of the projected width of the slip trace. Using the formula $l = W$ cosec θ it was calculated that the contamination spot method gave a value of l = 275 nm whereas measurement using the projected width of the slip trace gave l = 175 nm, the discrepancy Δl between the two values being 100 nm. If Δl is converted into a discrepancy in measuring the effective foil thickness, h , we obtain $\Delta h = \Delta l \cos 35^{o} = 82$nm. A series of such measurements were carried out involving several different faults over a range of thicknesses from which a mean value of $\underline{\Delta h = 75 \pm 10 \text{ nm}}$ was obtained.

Since it is difficult to believe that the slip plane trace is underestimating l it follows that the contamination spot method must be in error. Factors which could account for the observed disparity are:

A. a surface oxide film

B. a uniform layer of carbon contamination formed on the foil before insertion in the electron

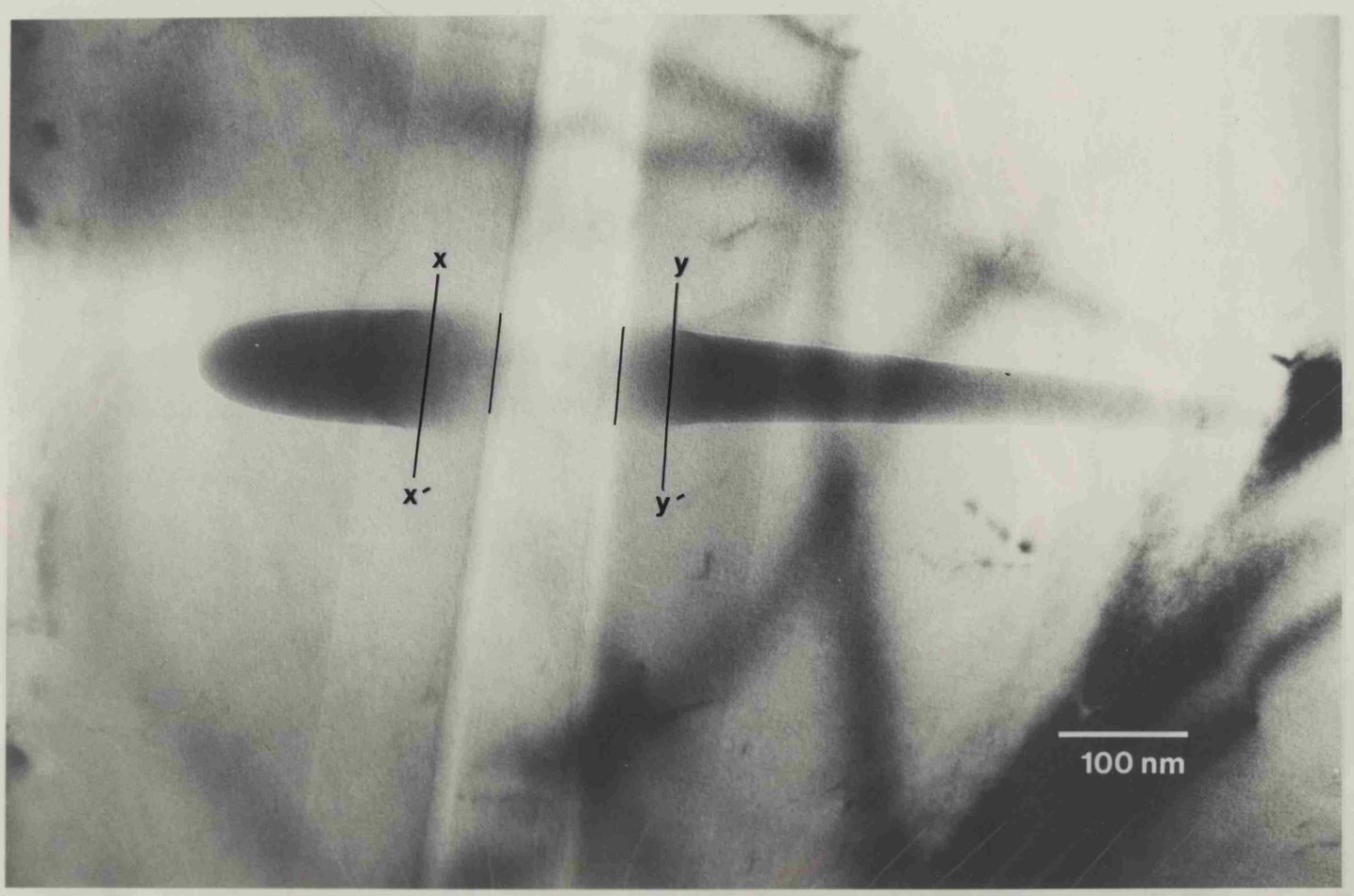

Fig. 40 Projected width of a slip trace and corresponding contamination spot displacement (stainless steel foil).

Fig. 40

Fig. 40 Projected width of a slip trace and corresponding contamination spot displacement (stainless steel foil).

Fig. 40

microscope.

C. a uniform layer of carbon contamination formed while the foil was being examined in the electron microscope.

D. an error in the practical application of the contamination spot method.

These factors are examined sequentially.

4.3.2 Influence of Pre-existing Surface Films

The possible presence of surface oxide and contaminant films could result in overestimation of true foil thickness when using the contamination spot technique. Clearly, surface films must be present in order to see slip traces in the foil. The thickness of such films was estimated using a calibrated wavelength dispersive analysis technique which related the oxygen and carbon characteristic intensities to film thickness.

To estimate oxide thickness a number of stainless steel strips were oxidised for different periods in a hot bunsen flame. The thickness of each oxide film was estimated from its interference colour (Vernon, Wormwell and Nurse 1939 & 1944) and ranged from 45 to 70 nm. The oxygen K emission of each specimen was measured in an electron probe microanalyser using 5 keV electrons and a specimen current of 100 nA. A calibration curve of these data was constructed (Fig. 41) and the oxide thickness on electropolished, stainless steel TEM specimens deduced by relating the oxygen K intensity from these specimens to the calibration curve. It was concluded that any oxide film present on the electro-

polished stainless steel foils was less than 2.5 nm per surface.

In similar fashion the thickness of any carbon contaminant layers was found. The calibration curve was produced using stainless steel samples coated by vacuum evaporation with known thicknesses of carbon (measured by multiple beam interferometry and quartz crystal techniques). These results showed negligible carbon (< 2nm per surface) to be present on the electropolished foils.

The surface layers present on an electropolished stainless steel specimen account for no more than ≈9 nm of the thickness. The total discrepancy between thickness obtained by the slip trace and contamination spot techniques was 75 ± 20 nm. Clearly other factors are involved in causing the contamination spot technique to register such a large overestimation. One attributable factor could be the formation of a surface carbon film within the TEM during examination. Another could be due to an inherent uncertainty in locating the exact position of the contamination spot/specimen surface interface. The discrimination between these two factors required setting up a special experiment and, is described in the next sub-section.

4.3.3 Surface Film Growth in the TEM

To examine the possibility that a localised layer of contamination could have formed on the surfaces of the specimen while it was being examined in the

electron microscope, foil thicknesses were measured using the contamination spot technique before and after an aluminium film of known thickness had been deposited. The intention was to remove any errors inherent in the method of contamination spot measurement by subtracting the two sets of readings.

A row of standardised contamination spots ($I = 2 \times 10^{-10} t_{dep} = 30$ s) spaced 2.5μm apart was deposited on a stainless steel foil with its surface approximately perpendicular to the electron beam. It was then tilted through 45^{o} and the spot separation measured. Next the foil was coated with an evaporated layer of aluminium in the Edwardes 12E6 coater. The production of the film and the measurement of its thickness is fully described in section 4.1.2. The film thickness was determined to be 170 ± 5nm. The specimen was reinserted into the electron microscope and a second set of contamination spots placed between the first series. Conditions of deposition were as before and the spot separations were measured after tilting through 45^{o}. Both sets of data are plotted in Fig. 42 and the curve for the specimen after coating with aluminium gives points which are consistently 180 ± 10 nm higher than for those of the non-coated specimen (the undulation in both curves is due to a non-uniformly tapering section in the region of a grain boundary).

Comparison of the interferometric data with contamination spot measurements indicates that any contamination of the foil surface produced during examination

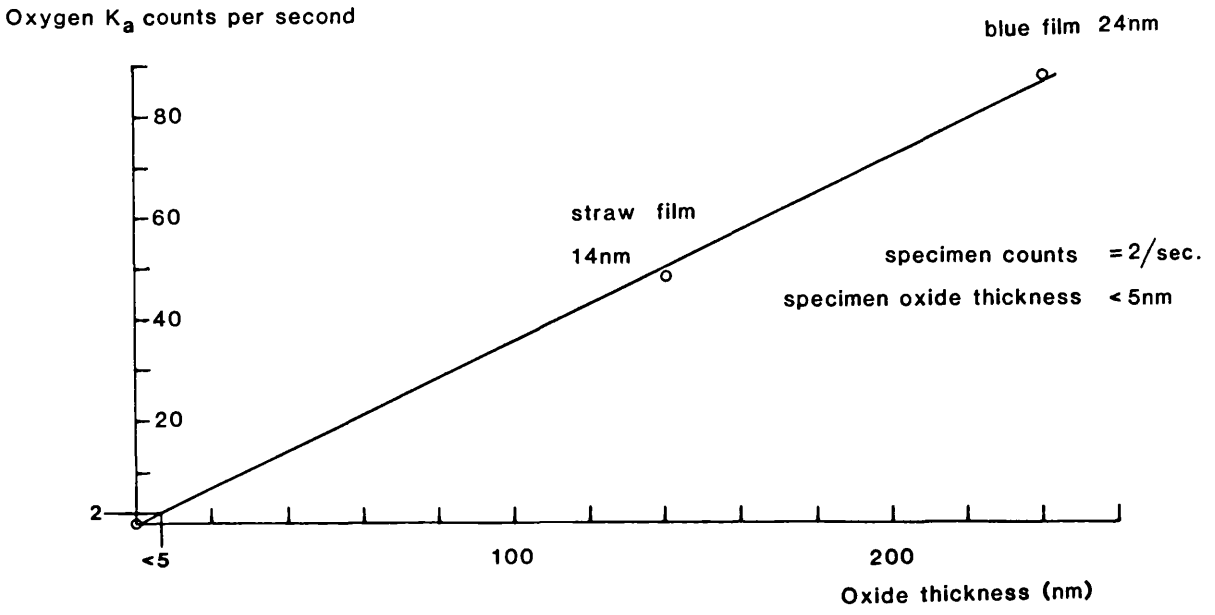

Fig. 41 Calibration curve for oxide thickness determination.

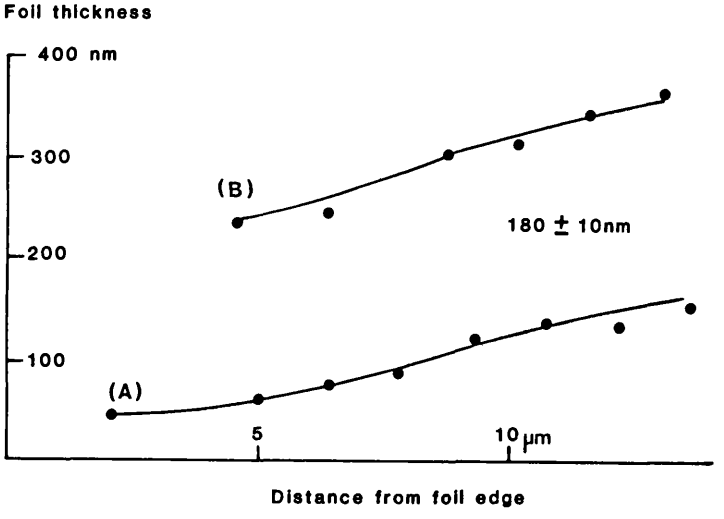

Fig. 42 Foil thickness profile (A) before and (B) after the deposition of an aluminum layer 170± 5nm thick.

is limited to less than 10 nm per surface, i.e. less than 20 nm overall. Hence the contamination spot method itself must contain the major source of error. Table 5 reproduces the information from which this deduction is made.

Table 5. Sources of overestimation in the contamination spot method.

CONTAMINATION SPOTS DEPOSITED ON STAINLESS STEEL	
TOTAL O/E = 75 ± 10 nm	
SOURCE OF O/E	MAGNITUDE
Oxide layer	5 nm
Contamination layer (produced during specimen preparation)	<4 nm
Contamination layer (produced in TEM)	<20 nm
∴ Contamination spot O/E	= 75 - (5+4+20) = 46 ± 5 nm

4.4 Analysis of Uncertainties in the Contamination Spot Method

The accuracy of the contamination spot technique rests heavily on the precision with which the position of the spot/specimen surface interface can be assessed. For an apparently well defined spot this will be enhanced by sharp image contrast between the spot and foil surface. Such contrast may well be affected by the profile of the spot, its size and the nature of the substrate upon which it is deposited.

Instrumental and measurement errors will of course be present. As one is essentially measuring the difference

between an initial and final tilt, errors from this source are less than ± 10'. The magnification, calibrated as in section 3.2, is accurate to within ±1 % providing the specimen is eucentrically positioned and measurements are performed on the negative. By measuring directly from the negative and using a light box and magnifying lens, the spot separation can be measured to within ± 0.2 mm. This corresponds to a typical error in h, the beam direction thickness, of ± 2.8 nm (M = 100K, $\theta = 45^{\circ}$). The total of these three errors result in a thickness uncertainty of ± 3.5 nm for a foil 100 nm thick tilted through an angle of 45° and photographed at a magnification of 100 K. This is summarised in Table for the range of thicknesses covered

Nominal thickness	Mag.	Tilt	uncertainty
500 Å	100K	45°	± 30Å
1000 Å	100K	45°	± 35Å
1500 Å	100K	45°	± 41Å
2000 Å	100K	45°	± 49Å
2500 Å	100K	45°	± 58Å
3000 Å	100K	45°	± 67Å
5000 Å	100K	45°	± 105Å

Table 6. Magnitude of errors in corrected contamination spot technique.

4.4.1 Effect of Spot Profile

Let us begin by constructing the expected carbon profile across a pair of contamination spots produced with the electron beam perpendicular to the foil surface. The measurement required to calculate the thickness of the foil is the distance between the tips of the spot cusps (see Fig. 43). However, if the spots do not have this idealised shape but are broadened at the base by a 'tailing' effect (Fig. 44) then the carbon profile will be different.

Figures 44b and c show the result of introducing such a tail. Firstly the carbon level does not drop to zero between the two maxima (44b) and secondly the edges of the spot become more diffuse. If the distance between the tips of the cusps is measured (44c) the result after applying the tilt correction would correspond to h', which is greater than the foil thickness.

In order to check this hypothesis a photo-densitometer trace was obtained from the electron micrograph of a contamination spot. The spot had been formed on a thin foil of annealed aluminium, this material giving regions of more uniform contrast than were obtainable with stainless steel. Figure 45a shows spots formed on an area of foil $\sim$ 300 nm thick. It can be seen that the spots are well separated and there appear to be no overlapping regions. The corresponding densitometer trace, obtained using a finely collimated beam of light (50μm slit), is given in Fig. 45b. Its closer similarity with the carbon profile illustrated in Fig. 44b than

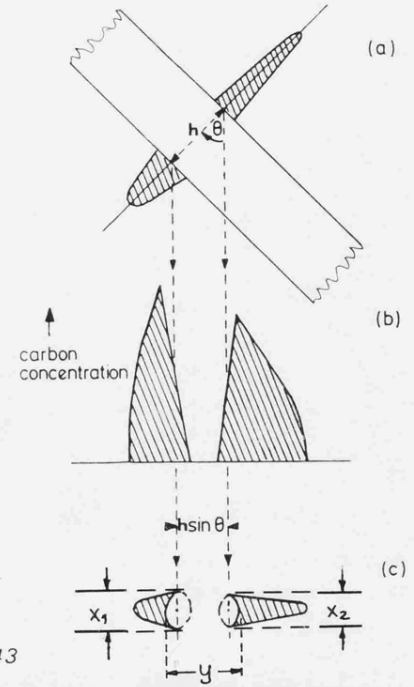

Fig. 43

Expected carbon profile and plan view of spots resulting from cones of contamination produced at normal incidence to foil

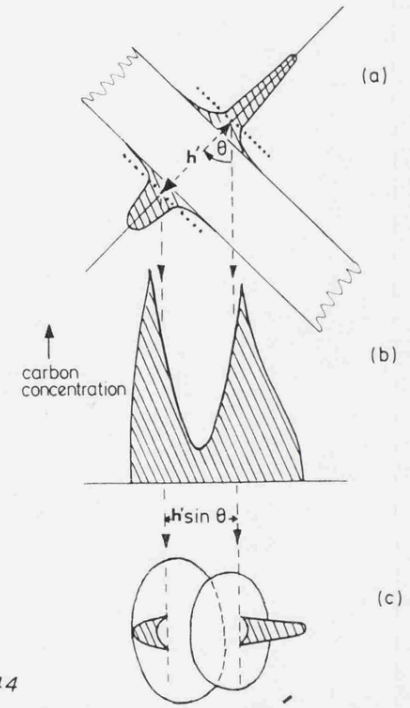

Fig. 44

As *43* but with disc of contamination surrounding cones; note that in (b) carbon level is not now zero between maxima

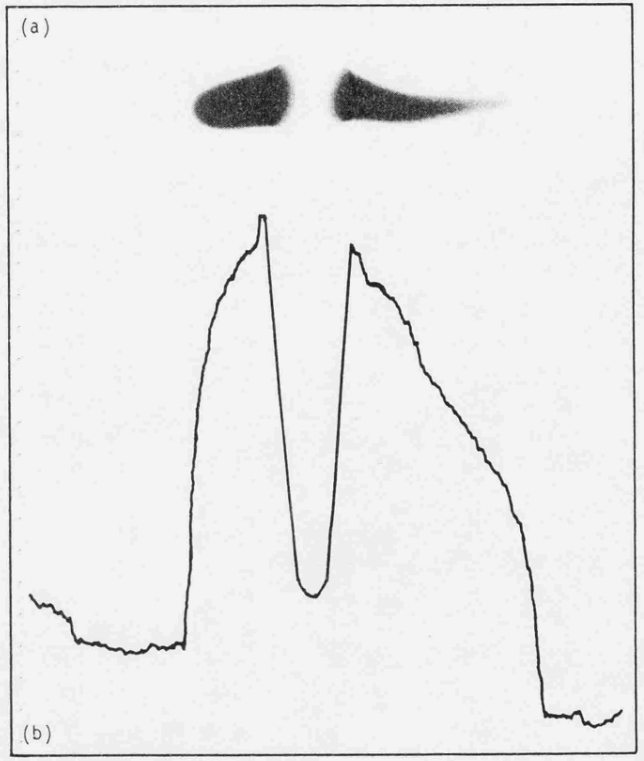

45 (a) Contamination spot produced on Al foil at normal incidence (foil tilted through 35°); (b) corresponding photo-densitometer trace across spots; note profile is better represented by *44(b)* than by *43(b)*

Figs. 43–45 Effect of spot profile on thickness determination.

the idealised form in Fig. 43b confirms the existence of a 'tail' or aureole surrounding the contamination spots. The important point to note is that although the contamination spots appear to be well separated in the electron micrograph the densitometer trace shows a detectable level of carbon between them.

4.4.2 Effect of Spot Size

It seems logical to assume that the size of the surrounding aureole will be related to the size of the contamination spot and that the degree of foil thickness overestimation will thus also depend on these factors. This indeed was observed when thickness was measured using spots with deposition times of 30s and 90s respectively.

Figure 46 shows the estimated thickness profile of a stainless steel foil using spot deposition times of 90s and 30s. In Fig. 46a it is apparent that the 90s spots predict higher thickness values than the 30s spots. However the 90s spots were deposited after and in between the 30s spots and it could be argued that they are in fact resting on the 'tails' of the previously deposited series. In Fig. 46b no such ambiguity exists. The 90s series of spots still produced larger over-estimations of foil thickness despite being deposited prior to the 30s spots. The difference in thickness values produced from 90s and 30s spot data was 20nm when the 90s spots were deposited first and 30nm when they were deposited second.

Fig. 46

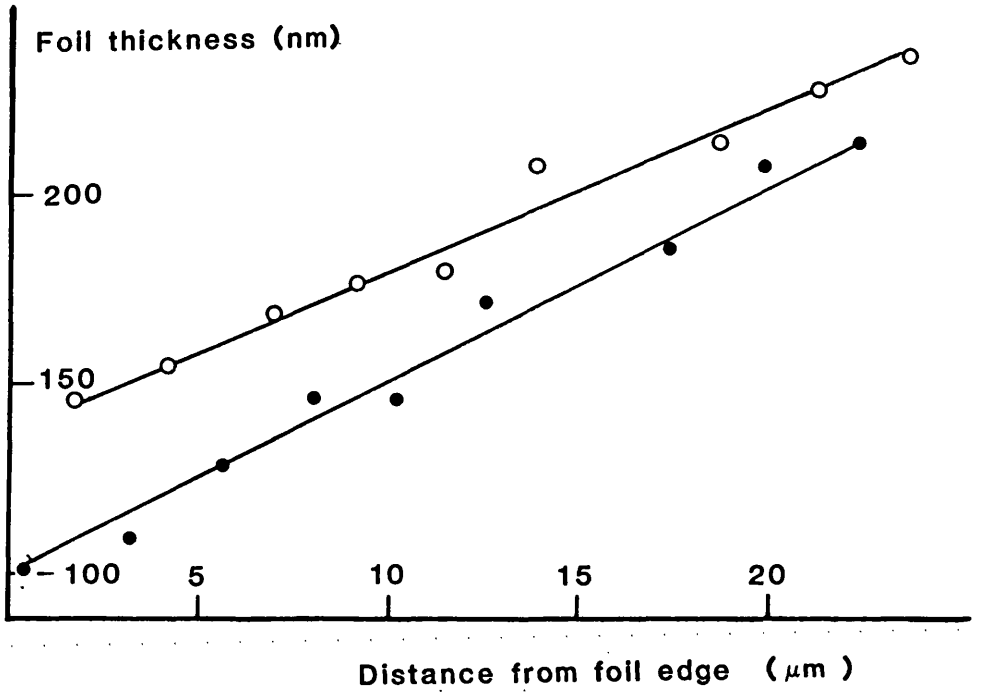

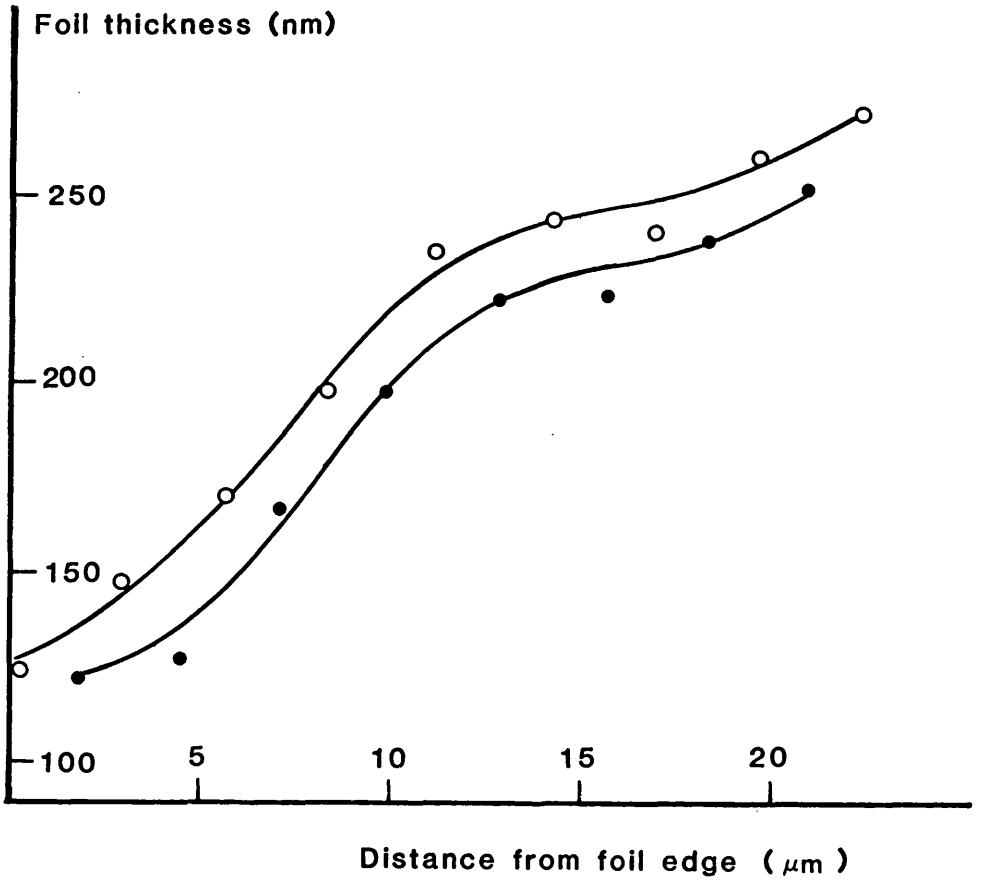

Fig. 46

Foil thickness vs Distance from foil edge. Contamination spot data.
(a) 3 0 second spots (•) deposited prior to 90 second spots (o)
(b) " " " after " "

It may be concluded from these observations that:
(i) there is an error in the contamination spot method of measuring foil thickness since 90s spots always give larger overestimates of foil thickness than 30s spots; and
(ii) since the difference in the overestimates depends on whether the 30s or 90s spots were deposited first, part of the measurement error must be due to some overlap between neighbouring spots.

It is thus beyond doubt that some broadening of the base of the core deposit must occur. An indication of this was available from earlier observations (Fig. 33) where a thin but visible annulus of carbon surrounded the base of spots deposited at relatively high beam currents. The annulus was, however produced under unusual irradiation conditions and such a feature was not readily visible around any of the spots deposited under the adopted standardised conditions.

4.4.3 Effect of Different Foil Materials

The method of comparing contamination spot data and slip trace width for stainless steel, described in 4.3.1 and 3.3 was adopted for use on different materials.- Slip traces and grain boundaries in copper and aluminium were compared with the standardised contamination spot technique. A wide range of thicknesses was studied by using the tapering faults which were available in these foils.

The results of the many thickness comparisons made are shown in Figs. 47 and 48. It can be seen that the more dense material, Cu, gives a greater degree of

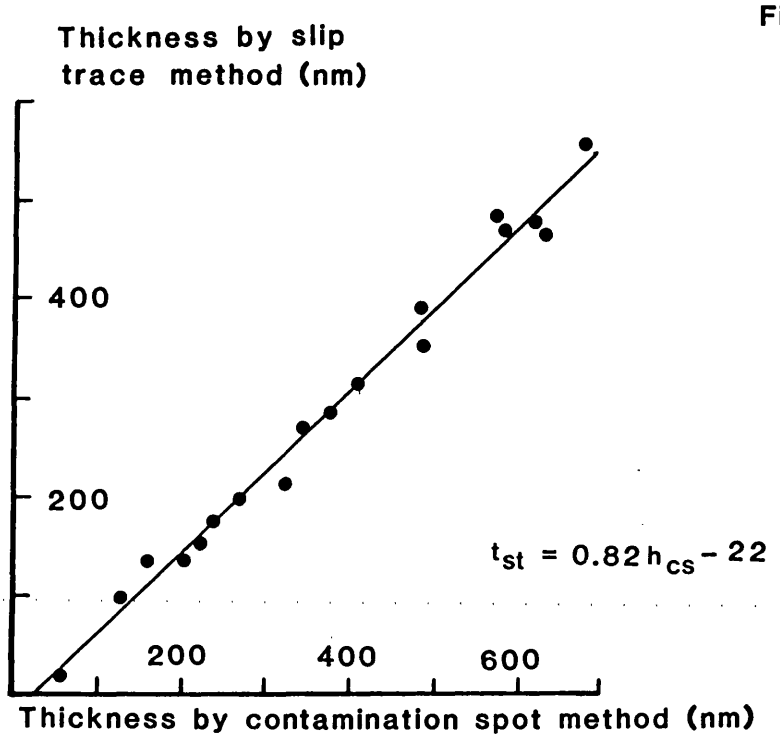

Fig. 47 Comparison of slip trace and contamination spot results for aluminium specimens.

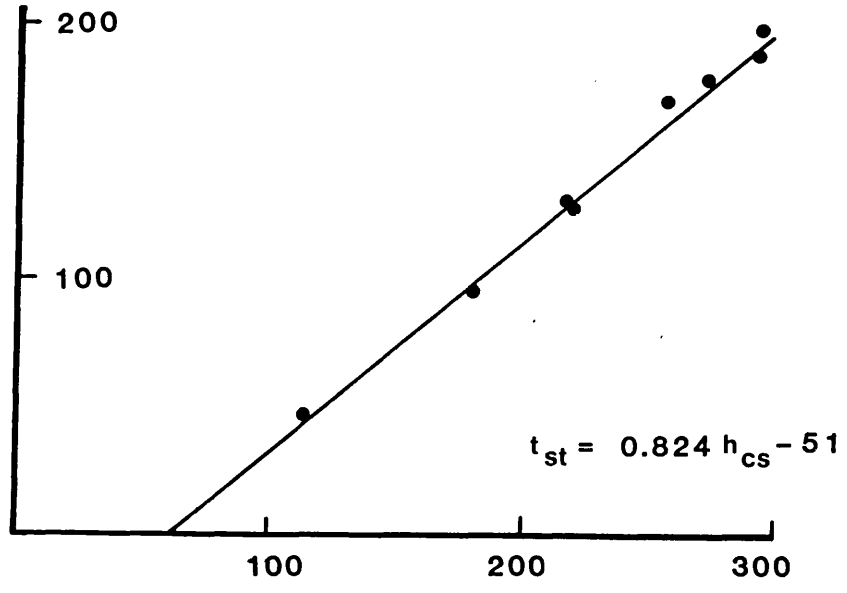

Fig. 48 As above for copper specimens.

overestimation and that for both materials the degree of overestimation increases with increasing thickness. This is thought to be due to decreasing contrast between the spot base and substrate at higher thicknesses and substrate densities.

4.5 Discussion

The contamination spot method may be used for rapid determination of the thickness of TEM specimens. The 'thickness', h, is measured in the beam direction and as such is the measurement required for most materials studies. This value will equal the 'true thickness' when the foil normal and beam direction are parallel at the time of deposition. The total specimen thickness is measured by the contamination spot method. This will include any films residing on the metal surface. Such layers may include oxide films produced during preparation and a carbonaceous layer formed either during preparation or examination in the electron microscope. Even with extreme care being taken the magnitude of these factors may introduce an over-estimate in foil (metal) thickness of ≈ 30 nm. For different specimen substrates and preparation procedures this factor could change in magnitude.

The contamination spot itself is subject to over-estimation. The level of overestimation is sensitive to the deposition time, the substrate and the actual thickness being measured. When all these uncertainties are recognised and their magnitudes determined, the contamination spot technique provides a useful method for obtaining reproducible foil thickness values. For confidence in these values the specimen preparation and spot deposition must be performed under standardised conditions and the method must first be calibrated using another absolute technique such as the slip trace technique. For such a fully calibrated system the potential errors in thickness are

approximately ± 10nm (typically h = 100 nm ± 8.5, 250 nm ± 10, 500 nm ± 13 etc), which is a 10% error for thickness of 100 nm but only 2% when the thickness is 500 nm. This level of accuracy may be improved by adopting a special measuring technique.

Figures 8 and 43 show that the normal spot analysis procedure requires estimating the position of the interface between spot and specimen surface. The position of this interface is not well defined as the image contrast changes very gently to either side of it (see Fig. 43b). It can be seen from the same figure that peak contrast (maximum carbon thickness) coincides not with these interface positions but with points on the circumference of the cone base. These positions are sharply defined in the spot image and it is easier and more precise to measure between these contrast maxima . This is especially true when overall contrast is low e.g. when imaging thick foils. In the majority of cases the spot bases are circular in shape and in these circumstances the improvement in measurement precision may be obtained by substituting

$$l = y - \left(\frac{x_1 + x_2}{2} \cdot \cos\theta\right) \qquad 4.2$$

in the normal thickness equation viz $h = l \operatorname{cosec} \theta$. When these spots are deposited on a tilted foil, as in x-ray studies, the equation may further be modified. If α is the angle at which spots are deposited and θ the angle at which their separation is measured then, providing θ and α are either side of the zero tilt position equation 4.2 may be re-written

$$l = y - \frac{x_1 + x_2}{2} \cos \theta \sec \alpha \qquad 4.3$$

The upper thickness limit using the contamination spot method depends only on obtaining satisfactory image contrast of the separated spots. The lower limit is governed by the ease with which the spot-surface interfaces may be located. These converge in thin foils to the extent that the top and bottom surface spots appear to overlap in the image. Theoretical minimum thicknesses of 20 - 30 nm could be measured using standardised spots.

5. CONVERGENT BEAM DIFFRACTION

5.1 Preparation of Specimens

Specimens of aluminium (sample composition, table 1) were prepared for TEM examination using the electropolishing conditions given in table 2. The procedure for electropolishing such samples has already been detailed in section 3.1.

5.2 Convergent Beam Diffraction Measurements

5.2.1 Production of convergent beam diffraction patterns

Prior to inserting the electropolished foil in the microscope, instrumental settings for both TEM and STEM modes were carefully adjusted to ensure that the electron optics remained aligned whenever the spot size was altered. A double tilt or rotation-tilt specimen holder was used, either device greatly aiding the production of two beam diffraction conditions.

With the specimen stage eucentrically positioned and an area of interest located, the following procedure is adopted to obtain a convergent beam diffraction pattern (CBDP).

A. Select area diffraction mode is deployed and the sample tilted until a strong two beam condition is obtained. The diffraction pattern from a thick region of foil is used to achieve this, the coincidence of the chosen Kikuchi line and diffracted spot facilitating accurate alignment. A micrograph of the diffraction pattern taken at this stage can be used to index the diffracting planes. It is wise to do this with the

sample slightly tilted off two beam conditions to allow non systematic reflections to contribute and aid in the pattern identification.

B. All apertures below the specimen in the electron column are removed and the largest condenser aperture (diameter 400μm) inserted to enlarge the diffracted disc size.

C. A low TEM magnification of either x 330 or x 660 is selected. The magnification control effectively acts as a camera length adjustor, low magnification giving a short camera length which results in a wide angle view of the diffracted spots being obtained.

D. The liquid nitrogen cold trap is introduced and the area of interest is 'flooded' to fix the surface contaminant. This process, devised by Eades and Rackham (1976) consists of irradiating a large area of foil with a defocussed electron beam. In the illuminated region contaminant molecules are transformed into an inert thin carbonaceous layer. Further contamination cannot occur until hydrocarbons from the edge of the fixed zone have migrated to the beam. The surface diffusion of such molecules is temperature dependent and with the cold trap present contamination free operating periods of up to five minutes are available.

E. The scanning module is turned on. This transfers

control of the objective lens to this module while the condenser lens adjustments are achieved as before. Greater flexibility is now achieved as the two controls may be used simultaneously to control beam convergence.

F. A medium electron spot size (diameter, 1μm) is obtained by adjusting the lens current in the first condenser lens. Smaller spot sizes may be used but contamination rates will increase accordingly.

G. The condenser and objective lens controls are adjusted to obtain a clear convergent beam diffraction pattern. An inversion point in the image indicates that maximum beam angle convergence has been obtained.

H. The magnification control should then be altered until the diffracted discs are almost touching and/or extend to the photographic frame size limits on the fluorescent screen. The pattern is then photographed.

A second method for obtaining CBDP's utilises the very fine probes obtainable in the micro-micro diffraction mode. Steps A to E are common to both techniques but then the following procedure is used.

F. The micro-micro diffraction mode is selected and an image obtained on the cathode ray screen.

G. The fluorescent viewing screen, normally upright in this mode, is manually lowered and the scanning coils de-activated to form a stationary probe on the specimen.

H. The condenser controls of the scanning facility are adjusted to focus the discs now visible on the fluorescent screen. If the projector lens is switched off the camera length is reduced to $\frac{1}{5}$ of its former value

(approximately 200 mm as opposed to 1000 mm) and this will increase the size of the diffracted spots.

I The diffraction pattern is photographed.

To assess the usefulness and practical accuracy of the method a wide range of foil thicknesses were studied using various reflecting planes to form the CBDP. In this section of the work the errors that arise during the production and analysis of CBDP's are discussed and some idea of the technique's limitations will be given. However it is not considered reasonable to categorically state that the actual thickness measurements obtained by this technique are what they claim to be. They are, after all, based on a theory containing several assumptions. It is therefore important that the method should be compared with other techniques which supposedly measure the same parameters. To this end the CBD method is compared with the crystallographic method and the contamination spot method.

5.2.2 Analysis of convergent beam diffraction patterns and treatment of results

The selected area diffraction pattern corresponding to the CBDP was indexed and the theoretical extinction distance for the strongly excited spot obtained from Edington (1975).

Magnified (x 5) photometer traces of all CBDP negatives revealed the intensity distribution across the diffracted discs, all distances subsequently being

measured on these traces (Fig. 49). The distances of the minima $\Delta\theta_i$ and maxima $\Delta\theta'_i$ were measured and the deviation parameter for each fringe obtained from:

$$S = \frac{\lambda}{d^2}\left(\frac{\Delta\theta}{2\theta_d}\right) \qquad \text{(see Fig.50)} \qquad 5.1$$

All measurements were made on the side of the disc furthest from the transmitted spot. The position of the two outermost minima (furthest from the transmitted spot) are used to determine the approximate thickness by utilising the simple kinematic theory of electron diffraction. This is essentially a special case of the two-beam dynamical theory and considers the propagation of the transmitted and a single diffracted ray through a crystal when the diffracted ray is weak in intensity compared with the transmitted ray. No interaction is assumed to take place between them, approximately the case when S, the deviation from the Bragg angle is high. In this situation the intensity distribution of the diffracted ray with depth is given by

$$|\phi_g|^2 = \frac{\pi^2}{\xi_g^2}\,\frac{\sin^2(\pi ts)}{(\pi s)^2} \qquad \text{(cf equation 1.3a)}$$

where s, the deviation parameter is constant. Plotting intensity against s, Fig. 51 it can be seen that the minima occur at $\pm\frac{1}{t}$, $\pm\frac{2}{t}$ etc. The thickness can thus be obtained from $\Delta s = \frac{1}{t}$.

Having obtained an approximate value for t and a value for ξ_g, the correct starting value of n_i can be

Figure 49

Typical CBDP Results.

(a) Select Area Diffraction Pattern of analysed area showing two beam conditions.

(b) Convergent Beam Diffraction Pattern.

(c) Photometer trace of above CBDP.

Fig. 49

(a)

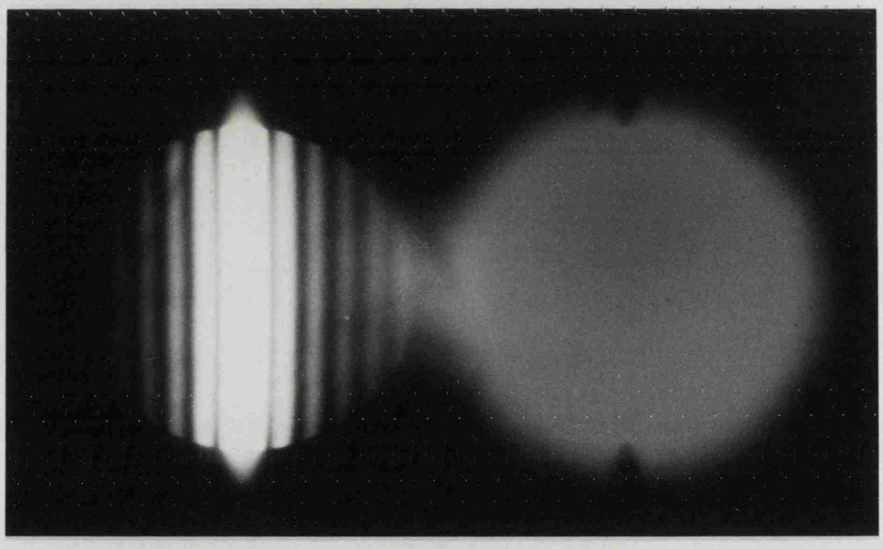

(b)

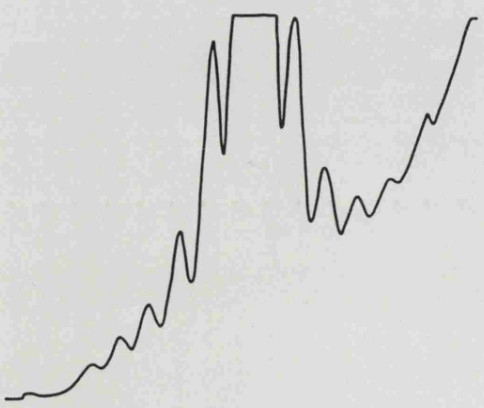

(c)

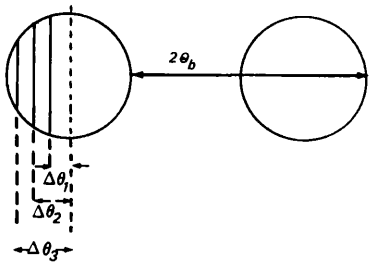

(a) Typical CBDP (schematic)

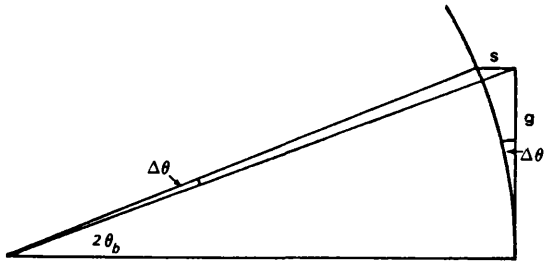

(b) Ewald Sphere construction

For small θ and $\Delta\theta$:-

$s = g.\tan\Delta\theta \simeq g\,\Delta\theta = g.2\theta_b(\Delta\theta/2\theta_b)$

Now $\tan 2\theta_b \simeq 2\theta_b = \dfrac{g}{1/\lambda} = \dfrac{1/d}{1/\lambda} = \lambda/d$

and $g = 1/d$

$\therefore\ s = \dfrac{1}{d}\cdot\dfrac{\lambda}{d}\,(\Delta\theta/2\theta_b) = \dfrac{\lambda}{d^2}\cdot(\Delta\theta/2\theta_b)$

Fig. 50 Proof of equation 5.1

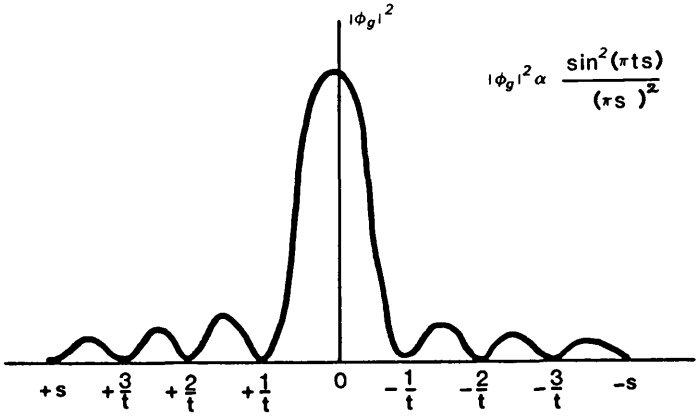

Fig. 51 Variation of diffracted beam intensity as a function of crystal orientation according to kinematic theory.

Figs 50 & 51

determined for equation 1.7 viz

$$\left(\frac{s_i}{n_i}\right)^2 = -\left(\frac{1}{\xi_g^2}\right)\left(\frac{1}{n_i^2}\right) + \frac{1}{t^2}$$

The above equation, with n_i an integer, is used to analyse the minima . A similar equation can be used for the fringe maxima where, instead of integer values of n_i being used, values of x_i are substituted which are solutions of

$$x_i = \tan x_i \qquad 5.2$$

This equation from Siems et al (1962) gives initial values of x_i as 1.430, 2.459, 3.471, 4.477, 5.482 etc.

Fig. 52 shows the extracted data from the CBDP in Fig. 49 plotted to show the effect of correct and incorrect choices in the starting value of n_i. For correct values the data lie on a straight line with the specimen thickness being determined from the intercept on the ordinate and the extinction distance from the slope of the line. This of course should closely agree with the theoretical extinction distance for the particular operating reflection.

Figures 53-56 show data from various CBDP's, plotted with their correct n values, for a range of specimen thicknesses. The thickness values are obtained from a best fit of the points; it may be mentioned here that since the outermost point (corresponding to the fringe spacing $\Delta\theta_1$), is most subject to error, it is sometimes excluded from the analysis. The justification

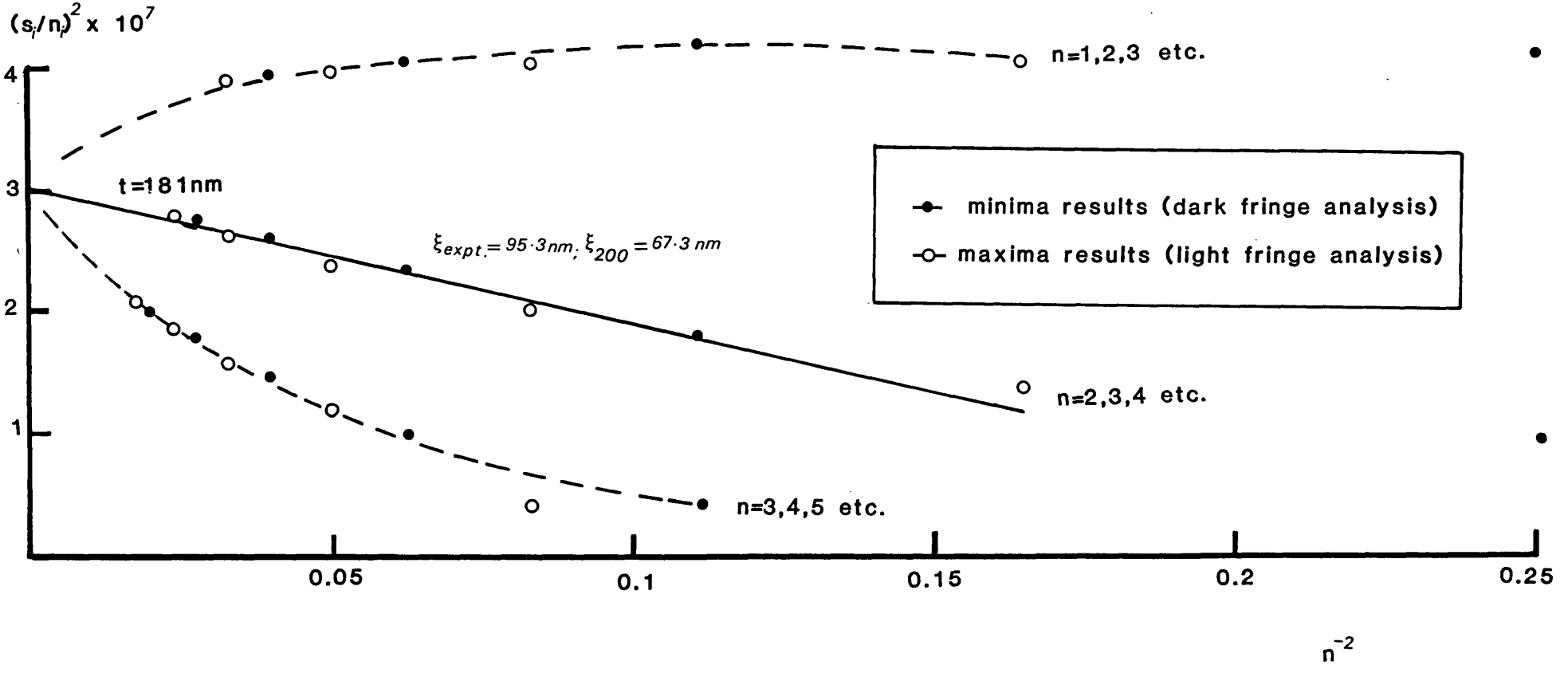

Fig. 52 Convergent-beam data from fig. 49 plotted to show the effects of incorrect and correct starting values of n.

Fig. 52

Fig. 53

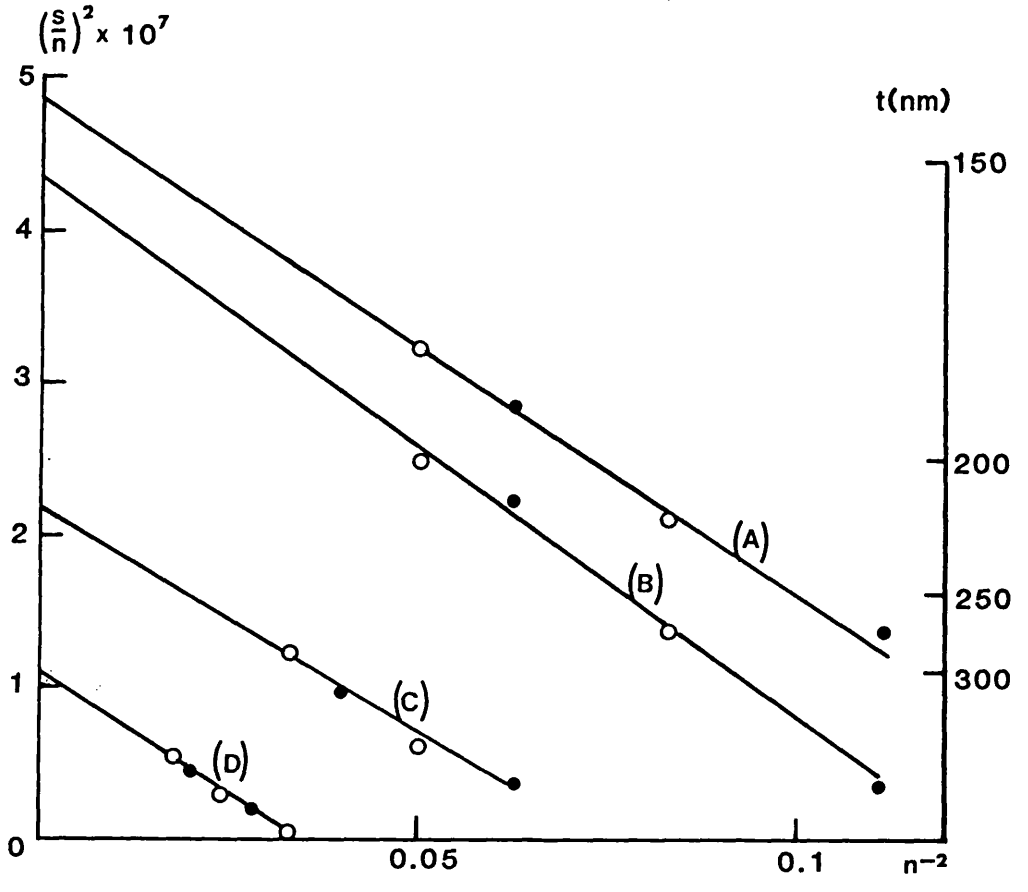

(A)	ξ = 57nm	t = 145nm
(B)	ξ = 53nm	t = 151nm
(C)	ξ = 56nm	t = 227nm
(D)	ξ = 56nm	t = 298nm

Fig. 53 $(s/n)^2$ vs (n^{-2}) for $\{111\}$ reflections in aluminium.

Fig. 54

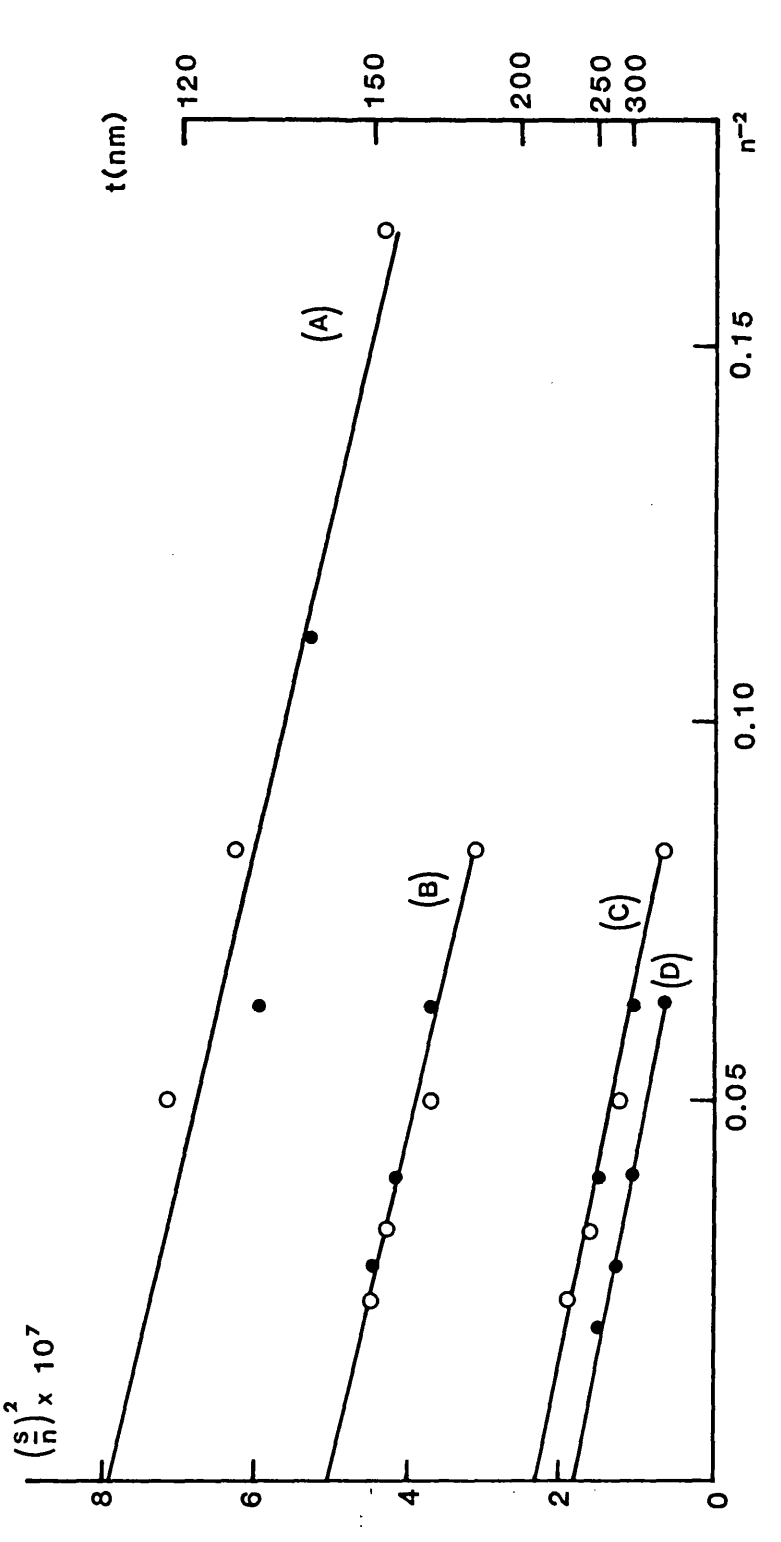

(A)	ξ = 67nm	t = 113nm
(B)	ξ = 65nm	t = 141nm
(C)	ξ = 70nm	t = 209nm
(D)	ξ = 71nm	t = 233nm

Fig. 54 $(s/n)^2$ vs (n^{-2}) for {200} reflections in aluminium.

Fig. 55

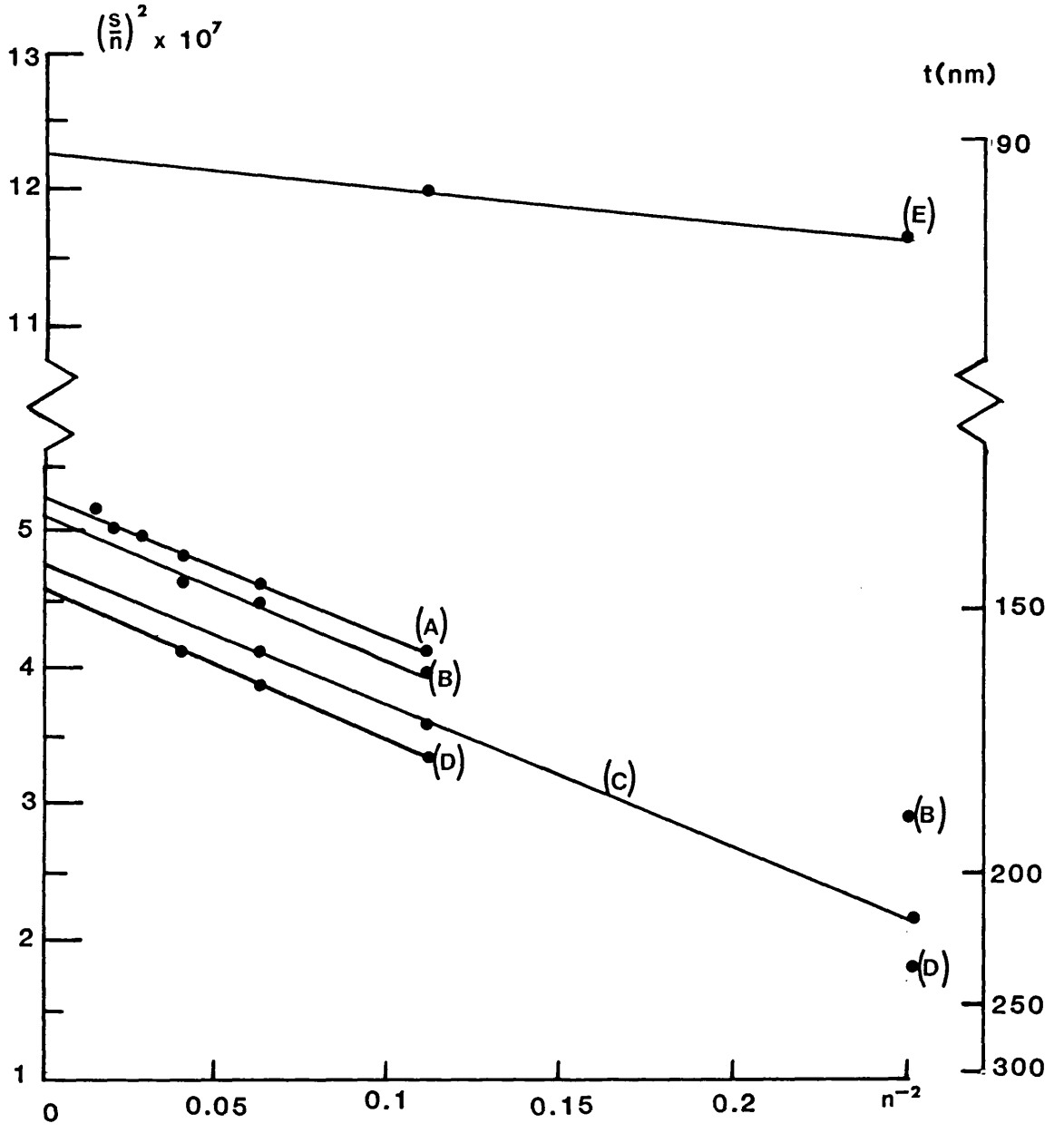

(A)	ξ = 97nm	t = 137nm
(B)	ξ = 102nm	t = 140nm
(C)	ξ = 97nm	t = 144nm
(D)	ξ = 94nm	t = 147nm
(E)	ξ = 155nm	t = 89nm

Fig. 55 $(s/n)^2$ vs (n^{-2}) for {220} reflections in aluminium.

Fig. 56

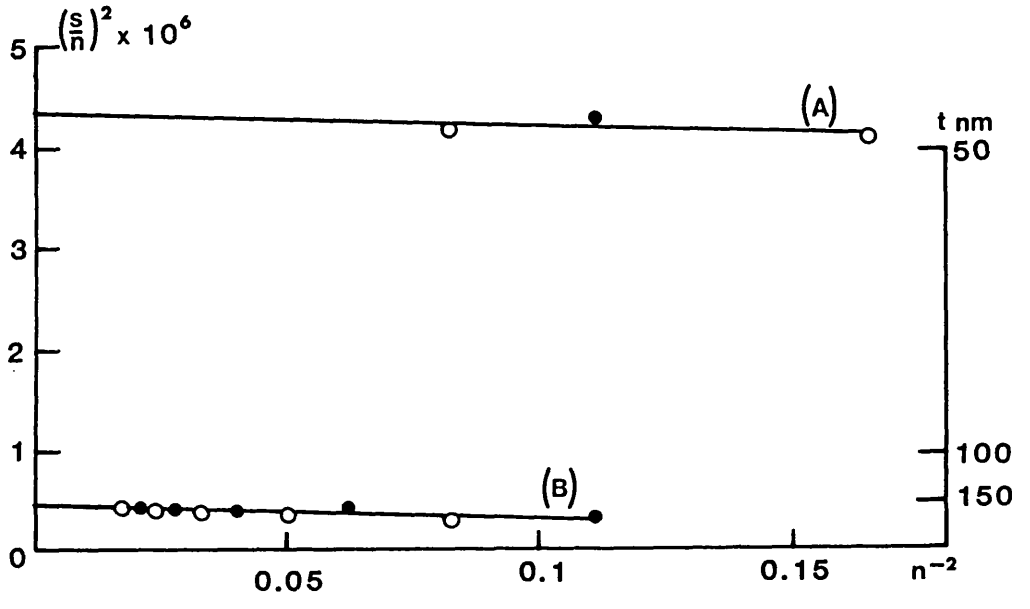

(A)	ξ = 155 nm	t = 48 nm
(B)	ξ = 104 nm	t = 154nm

Fig. 56 $(s/n)^2$ vs $(\bar{n}^2)$ for {311} reflections in aluminium.

for this is presented in the discussion of anomalous absorption. From the intercept of the best fit line with the $\left(\frac{s}{n}\right)^2$ axis the thickness of the specimen can be calculated. The positioning of the intercept can be determined precisely from the experimental points, the error in the intercept position resulting in thickness errors of no more than 3%.

The extinction distances obtained from the gradients of the curves are compared in table 7 with theoretical many beam values given in Edington (1975).

5.2.3 Discussion

Experimental values of t and ξ_g can be determined from analysis of convergent beam diffraction data. The positioning of the curve on the experimental points can be accomplished precisely with errors in t from this source being below 3%. It can be seen that errors in t appear to be greatest when ξ_g is small and small percentage changes in the relatively steep gradient cause the largest uncertainty in t. The converse is true for ξ_g which, being measured from the gradient of the line, has least uncertainty when the points lie on a steep line i.e. small ξ_g values.

The non coincidence of the experimentally determined ξ_g values with theoretically determined values is difficult to explain as no established pattern occurred. However the scatter in the results is greatest when ξ_g is large and the gradient of the line small. This is to be expected as minor errors in the $\left(\frac{s}{n}\right)^2$ positions, although

Reflecting plane	ξ_g expt. (nm)	Average ξ_g expt. (nm)	ξ_g theory (nm)
{111}	56.6 52.8 55.5 55.6	55.1	55.5
{200}	91.8 80.3 99.5 98.0	92.4	67.3
{220}	97.0 102.0 97.3 93.8 154.9	109.0	105.7
{311}	154.5 103.9	129.4	130.0

Table 7. Comparison of experimental and theoretical extinction values.

Approximate thickness range for which the thickness measurement technique is applicable.

Material	g	ξ_g (nm)	ξ'_g (nm)	Minimum thickness (nm)	Maximum thickness (nm)
Aluminium	111	55·5	2530	52	520
	200	66·4	2860	43	590
	220	106·3	3800	22	790
Copper	111	29·0	527	55	109
	200	32·2	557	31	115
	220	44·0	640	17	132
Gold	220	26·3	165	21	34
	311	31·0	176	16	36

Table 8. After Allen (1981)

negligibly affecting extrapolated thickness values will strongly bias the gradient of the line.

Systematic errors arise due to the limitations of the two beam theory assumptions. This theory only allows for interaction between the transmitted beam and one diffracted beam within the narrow confines of a column, with no loss or gain to the surrounding material. In practice reciprocal lattice points lying in the same straight line as the point corresponding to the strong reflection will produce systematic reflections. This is strikingly shown for {111} planes in Aluminium in Fig. 57. Spot 1 is the most strongly excited beam and is seen from 57(c) to intercept the Ewald sphere, but spots -2, -1, 2 and 3 are also present as they too are close to the Ewald sphere. If one considers the symmetrical case when Kx = 0, -1g and +1g reflections are equally excited with their deviation being given by $s = -g\theta_B = -g^2/2K$ where $\theta_B = g/2K$. Thus $w = s\xi_g$ is given by $-g^2\xi_g/2K = -g^2/2U_g$. $\xi_g = \frac{K}{U_g}$ where U_g is the potential of the g operating plane (see Thomas & Go ringe 1979 p.249). For $|w| > 1$ the reflections are both weak (kinematic) whereas for $|w| < 1$ both reflections are strong (dynamic) and a dynamical theory for at least 2 diffracted beams is required. At 100kV the values $g^2/2U_g$ for aluminium reflecting planes are 1.89 and 9.60 for {111} and {220}, while for gold the values are 0.53 and 2.22. Thus many beam effects are most pronounced for low order reflections in high atomic number metals.

Figure 57

The Effect of Systematic Reflections on a CBDP.

(a) Spot 1 is strongly excited but spots -2, -1, and 2 are also present.

(b) CBDP obtained under the diffraction conditions shown in (a).

(c) Schematic Ewald Sphere construction for the above diffraction conditions.

Fig.57

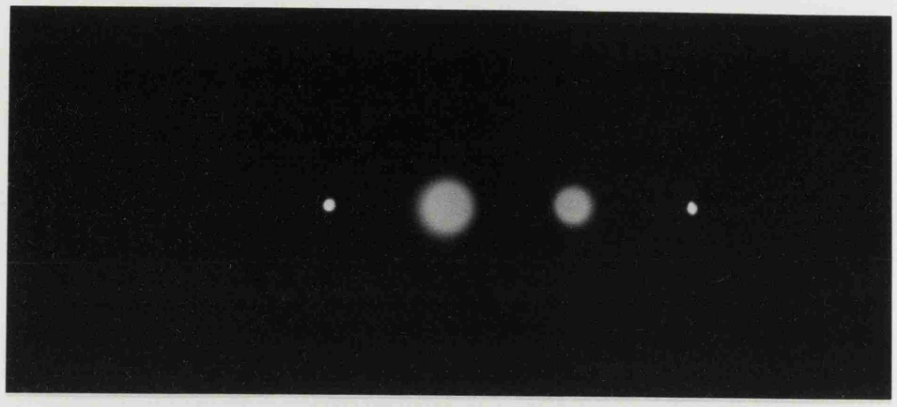

(a)

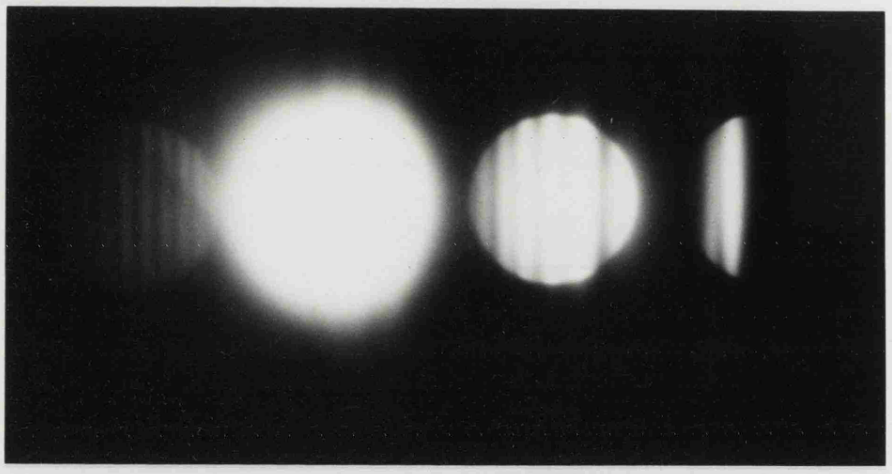

(b)

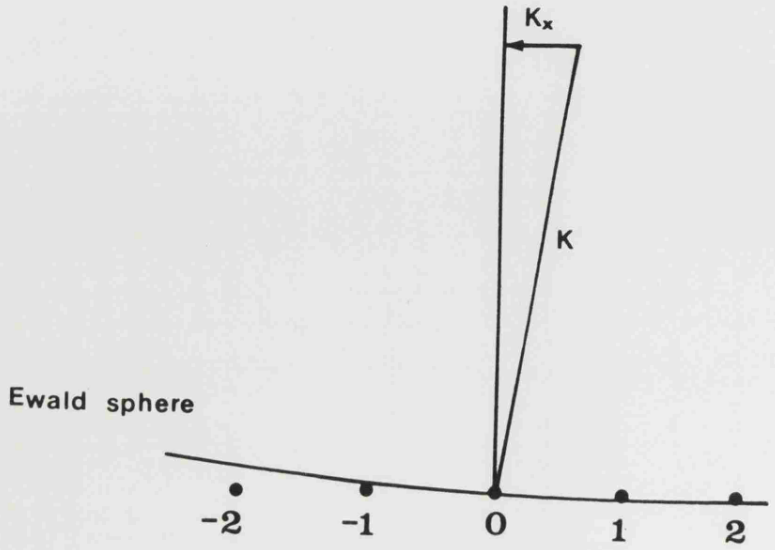

(c)

The effect of such multiple reflections on the accuracy of the method has been studied by Allen (1980) for the metals Al, Cu and Au. Using multiple beam dynamical theory (Hirsch et al 1965) he computed the variation in intensity across the strongly excited +g reflections for foils of varying thickness. For this purpose eight beams in the systematic row were excited (from $-\underline{3}g$ to $+\underline{4}g$) and the electron energy was 100 kV. The resulting intensity distribution for the +g reflection was then analysed by the Kelly method using the two beam equations 1.7 and 5.2 i.e. as if it was a photometer trace of an experimental CBDP. The resultant thickness value obtained was compared with the original thickness value used to produce the multiple beam trace. Allens results confirm that the effects of multiple reflections are more severe for low order reflections and high atomic number (high scattering) elements. For aluminium errors can be reduced to negligible proportions by using {200} or higher order reflections whereas in gold one must use {311} or higher.

With the microscope used in the present investigation the maximum allowable angle for a diffracted beam is 2.5×10^{-2} radians with the specimen eucentrically positioned. Diffracted rays from planes where $2\theta_B > 2.5 \times 10^{-2}$ radians pass out of the electron optical column. At 100kV operating voltages, CBDP's may therefore be formed using any diffracting planes with $d \geq 1.48\text{Å}$ i.e. {200} and {111} for most common f.c.c.

metals. Lowering the specimen below the eucentric position effectively reduces the camera length of the microscope. The manufacturers claim that lowering the specimen by 0.5mm doubles the maximum angle for a diffracted beam. This theoretically enables CBDP's to be obtained from all planes satisfying $d \geq 0.74\text{Å}$ i.e. up to {422} in most common f.c.c. metals. In practice, the highest order reflections used were {311}. Above this order the diffracted discs were very low in intensity. Also, photographing the diffracted and transmitted discs together proved difficult because of the difference in intensities. It also proved to be very difficult to converge the beam sufficiently to bring transmitted and high order diffracted discs close enough together to be photographed.

The presence of $n\underline{g}$ systematic reflections will also affect the intensity profile symmetry of the diffracted beam. For exact 2-beam conditions this is symmetrical about w = 0 (see Fig. 3a); however with the presence of systematic reflections the symmetry about w = 0 is lost. As w or $\underline{s}$ becomes more +ve, the $2\underline{g}$ reflection is more strongly excited i.e. multiple beam effects are more prominent on the side of the diffracted disc nearer to the transmitted spot. This is why all measurements were taken outwards from the w = 0 position. This again is more important for the low order patterns containing visible systematic reflections. Absorption effects have been discussed by Blake, Jostsons, Kelly and Napier (1978). The effects

of anomalous absorption on the CBDP can be seen in Fig. 52 where the $\left(\frac{s}{n}\right)^2$ values obtained from analysis of the maxima are in general lower than those values taken from the minima . The cause is the superposition of the anomalous absorption curve, which is a maximum at $\underline{s} = 0$ onto the intensity versus $\underline{s}$ curve for the diffracted ray, see Figure 58b. This results in a shift of maxima towards the $\underline{s} = 0$ position and the opposite for the minima , hence the positive or negative bias on the $\left(\frac{s}{n}\right)^2$ results from analyses of minima and maxima respectively. Fortunately errors due to the effect are generally self cancelling and, at higher $\underline{s}$ values the discrepancy between the results tends to zero as the anomalous absorption effects recede. However, for thin highly absorbing crystals with only two or three fringes of low $\underline{s}$ value the errors could be significant. This can be seen in Fig. 52 where the discrepancy between $\left(\frac{s}{n}\right)^2$ values obtained from maxima and minima is greatest for the innermost fringes (high $\frac{1}{n^2}$ values). However, as can be seen by the vertical thickness scale, only minor errors result in the determination of t but of course the gradient and hence ξ_g values will suffer larger errors, in some cases negative ξ_g values being calculated! For this reason the innermost fringe nearest $\underline{s} = 0$ was excluded from the analysis if seen to be strongly affected by absorption.

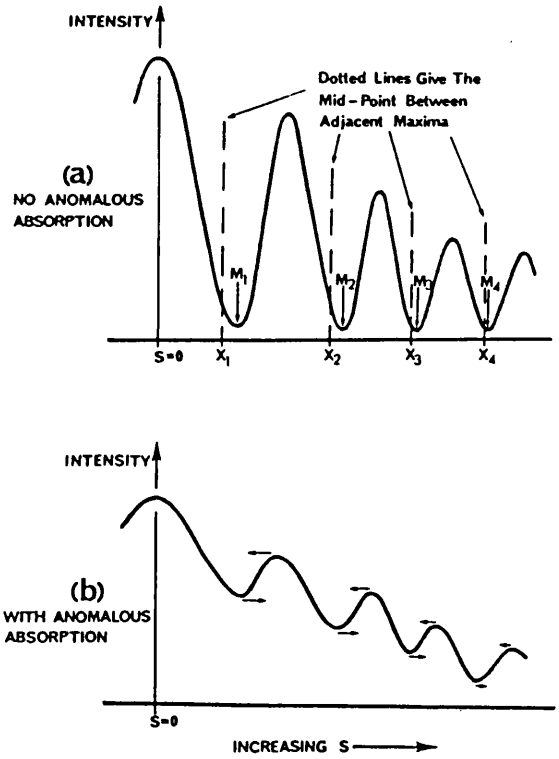

(*a*) Calculated diffracted intensity profile for zero absorption case showing displacement of the mid-point X_i of adjacent maxima from the true minima M_i. (*b*) Calculated diffracted intensity profile for finite absorption showing the shift in maxima and minima caused by the presence of the sloping background intensity.

Fig 58 The shift in intensity minima and maxima as a result of anomalous absorption. (After Blake et al 1978).

The effect of non-systematic reflections on the intensity distribution across the main diffracted spot are less tangible. It is known (Howie & Basinski 1968) that the presence of such reflections reduces the value of ξ_g, this being more noticeable at high g values. Any effects should be minimised by careful initial alignment to limit reflections to one axis if possible. It is considered that such reflections, if present, will influence thickness results to a much lesser extent than the more strongly excited systematic reflections.

Carbon contamination can build up rapidly on the surface of the TEM specimen, especially in the beam region, if precautions are not taken. This results in a degradation the CBDP quality due to electron scattering in the contaminant. Under such circumstances useful CBDP images could be retained only for a period of 15-30 seconds. Flooding of the specimen and insertion of the liquid nitrogen cold trap enabled good image quality to be retained for much longer periods, typically one or two minutes.

Thicknesses from 48nm to 300nm were successfully determined for aluminium samples using this technique. Allen predicted the theoretical lower and upper limits of thickness determination by this method for several elements. The lower limit is based on the requirement of only two extrema being present in the diffracted disc to produce a linear plot, while the upper limit is governed by absorption effects which will cause

loss of contrast in the pattern. The values calculated (see table 8) show that CBDP's are potentially useful in measuring the thickness of materials like aluminium but have limited application to heavily absorbing materials such as gold.

5.3 Comparison of the convergent beam technique with Other Methods

Comparisons were made between the convergent beam technique and the contamination spot and tilting fault techniques. The former comparison was made directly while the latter was deduced.

It has been mentioned that CBDP and crystallographic methods are both thought to measure the metal thickness while the contamination spot technique includes any surface films in its measurement. The comparison made in section 4 showed that the contamination spot method was capable of large overestimations. It is almost impossible to directly compare the crystallographic and convergent beam techniques due to the contrasting experimental requirements of each method. The main difficulties in such an exercise are given in table 9 Comparison of both techniques in turn with the contamination spot technique allows the possibility of an indirect comparison to be inferred.

5.3.1 Contamination spot method

With two beam conditions being set up and prior to the convergent beam diffraction patterns in section

Conditions required for crystallographic techniques	Conditions required for convergent beam diffraction
Presence of defects required e.g. slip plane traces, stacking faults etc.	Defect free region needed for analysis
At vertical fault position, symmetrical diffraction conditions obtained	Exact two-beam diffraction condition required
Fault habit planes predominantly {111} in many metals	Low order planes to be avoided if possible
Rotation-tilt specimen holder required for correct alignment of fault axis.	Double tilt facilities required to remove unwanted non-systematic and systematic reflections.

Table 9. Contrasting requirements for crystallographic and convergent beam diffraction techniques.

5.2.1 being obtained, four contamination spots were deposited, under standard conditions, forming each corner of a square grid. The spacing of the spots in each grid was approximately 1.5μm. The thickness of the foil was determined in the usual manner and the foil returned to its two beam condition. The CBDP was then taken from the centre of the grid after following the sequence outlined in section 5.2.1.

The average thickness value obtained from the four surrounding contamination spots was compared with the value obtained from the CBDP. As the contamination spots were deposited with the specimen in the two beam condition, the thickness values obtained by the two methods are directly comparable. Figure 59 shows this relationship. It can be seen that the contamination spot technique produces the higher values of thickness.

5.3.2 Tilting fault technique

In section 4.4.3 the relationship between thickness values measured by the contamination spot and tilting fault methods was investigated. A linear relationship was found, which for aluminium foils obeyed

$$t_{\text{SLIP TRACE }(\text{Å})} = 0.82h_{\text{C/SPOT}} - 220$$

In the present comparison a least squares fit of the points showed that:

$$t_{\text{CONVERGENT BEAM }(\text{Å})} = 0.856\ h_{\text{C/SPOT}} - 309 \qquad 5.3$$

Both these lines are included in Fig. 59 for comparison

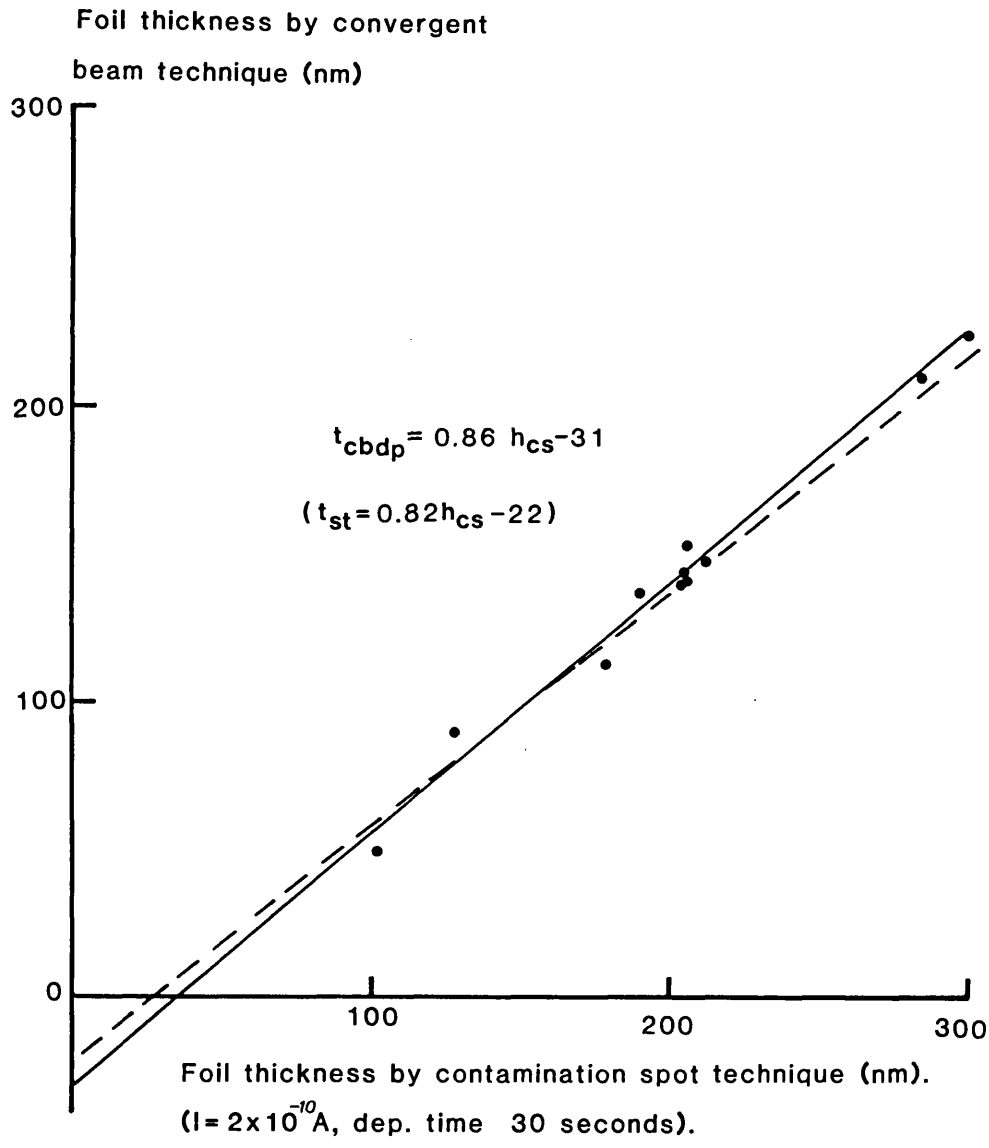

Fig. 59

Comparison of convergent-beam and contamination spot thickness results for aluminium.

(Broken line shows slip trace vs contamination spot comparison).

and it can be seen that within the limits of experimental scatter they are similar. The conclusion drawn from this study is that the convergent beam technique and slip trace techniques are comparable and both measure the same parameter i.e. the crystalline metal thickness.

6. X-RAY MEASUREMENTS

The potential use of x-ray data for determining foil thickness was outlined in the introduction. Characteristic and continuum radiation intensities are expected to change with specimen thickness and absorption and fluorescence effects may also be manifest in certain materials. The magnitude of such effects may make them useful in determining the thickness of thin foils.

In this study various x-ray phenomena were measured over a range of foil thicknesses and for a range of foil materials. The various phenomena, such as recorded intensities, absorption and fluorescence are known to depend on other parameters in addition to specimen thickness. It was therefore considered prudent to summarise the relevant theories prior to the experimental work

6.1 X-ray theory relevant to the present study

6.1.1 X-ray generation

Characteristic lines

The x-ray spectrum resulting from electron-specimen interactions consists of distinct lines, characteristic of the target material, superimposed on a background or continuum.

The energetic incident electrons colliding with atoms in the specimen may cause the ejection of inner shell electrons from some atoms. The subsequent return of the atom to a more stable state, caused by filling

the vacancy, is accompanied by the emission of a quantum of x-radiation. If the innermost atomic shell (K) is ionised the resulting radiation is identified as 'K' emission. The K spectrum consists of several lines due to transitions from L, M etc., levels which contain electrons of decreasing binding energy. Transitions from L to K and M to K result in Kα and Kβ radiation respectively being emitted. This is slightly further complicated by various subshells within the L (L_{I-III}) and M (M_{I-IV}) shells giving rise to KαI ($L_{III} \rightarrow K$) etc., and $K\beta_2$ (M_{III} - K) lines. The potential between the energy levels is fixed and unique to each element. The frequency of the characteristic radiation emitted by such transitions may be obtained from the well known equation:

$$E = h\nu \qquad 6.1$$

(Energy = Planck's constant x frequency)

This may be more conveniently expressed as:

$$E = 12396/\lambda \qquad 6.2$$

where E is measured in electron-volts and the wavelength in angstroms. The uniqueness of characteristic lines to specific elements was first related by Mosely (1913) who found that the characteristic Kα lines had frequencies related to the atomic number, Z, of the target element by the equation:

$$\nu = 2.48 \times 10^{15}(Z-1)^2 \qquad 6.3$$

Not all inner shell transitions result in an x-ray being produced. Sometimes the energy made available is used to eject an electron (Auger effect). This effect occurs more often in low atomic number elements where inner shell binding and electron cloud shielding are less efficient. The proportion of transitions resulting in an x-ray emission is known as the fluorescent yield, w. An equation describing the effect of atomic number on this parameter for K radiation has been given by Wentzel (1927) viz:

$$w_K = \frac{Z^4}{\text{constant} + Z^4} \qquad 6.4$$

Similar relationships have been discovered for L and M radiation.

The Continuum

Some incident electrons may interact with the 'nuclear field' surrounding the target atoms. This can cause a deceleration of the electron with the subsequent lowering of its energy being accompanied by the emission of an x-ray photon. As each interaction is unique, a range of emitted x-ray energies is produced extending right up to the energy (Duane-Hunt limit) of the incident electrons.

Continuum energy distributions are similar in appearance for any target material but the intensity is proportional to the atomic number, Z, of the target. Figure 11 shows a schematic view of a typical x-ray spectrum with characteristic lines superimposed on the

continuum. The theoretical maxima of the continuum curve has been predicted by Kramer (1923) to occur at $2\lambda_o$ where λ_o is the cut-off wavelength. In practice it usually occurs at a lower value of λ due to preferential absorption of the longer wavelength (less energetic) x-rays.

6.1.2 Depth distribution of generated x-rays

As electrons become progressively absorbed and decelerated during their passage through the target, the distribution of generated x-rays changes as a result. For a bulk specimen where no electrons are transmitted the typical electron and x-ray distributions are shown in Fig. 60. These theoretical profiles, predicted using Monte-Carlo techniques, are in close agreement with experimental results obtained using methods such as the tracer technique of Castaing and Descamps (1955). Such distributions may be plotted graphically, Fig. 61, as a function of mass depth, ρz. Such $\phi(\rho z)$ curves are plotted for bulk materials with unity on the ordinate axis representing the x-ray intensity from a very thin film of the element.

The value of $\phi(\rho z) > 1$ at the surface of bulk samples is due to electron backscattering occurring in bulk samples (Fig. 61b) which increases the chance of x-ray production from surface regions. Forward scattering progressively increases an electron's path length through depth increments $\Delta\rho z$ (also see Fig. 61b). This increases the chances of causing x-ray generation

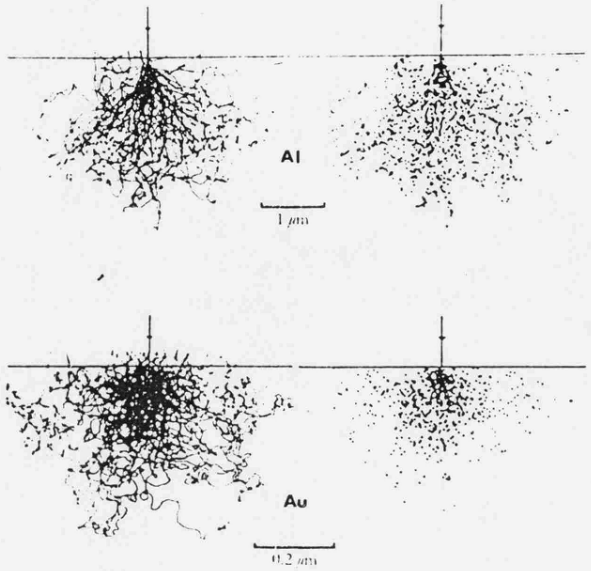

Electron trajectories (left) and X-ray production (right) for aluminium and gold (E_0 = 20 keV) computed by Monte Carlo method (Curgenven and Duncumb, 1971).

Fig. 60 (Through Reed, 1975).

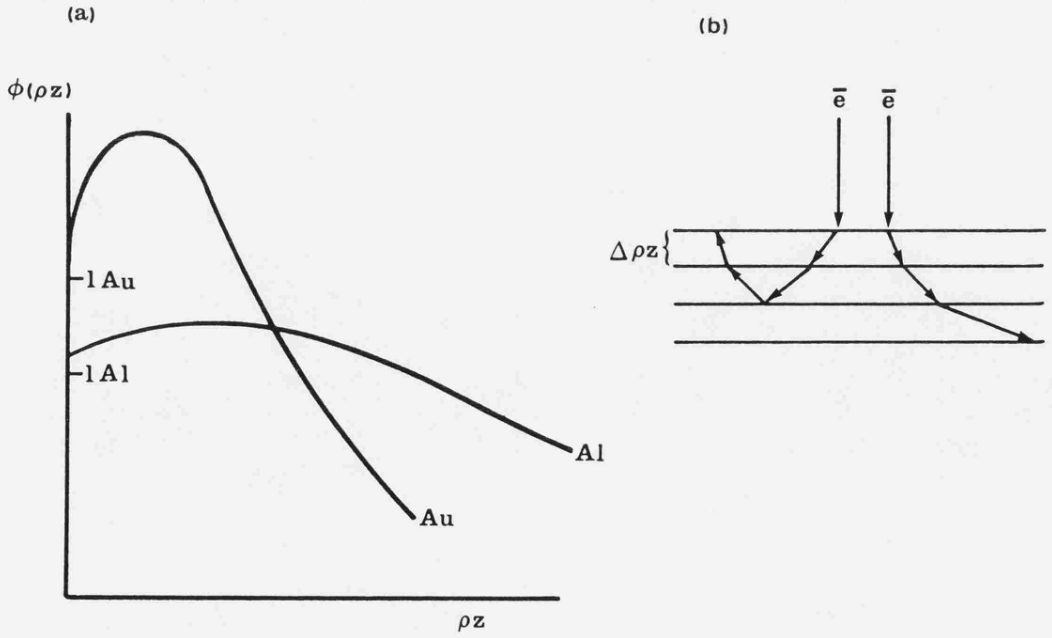

Fig. 61 (a) X-ray depth distribution (schematic), $\phi(\rho z)$ curves for gold and aluminium

(b) electron backscattering within a specimen.

and accounts for the initial rise in the $\phi(\rho z)$ curves. The eventual decrease in $\phi(\rho z)$ results from increasing absorption of electrons with depth.

6.1.3 Intensity of generated x-rays in a thin film

The characteristic intensity of x-rays generated in a thin film per incident electron has been given (Reed 1975) as:

$$Io_A = \frac{C_A N w_A Q_A \rho t}{A_A} \qquad 6.5$$

where C_A is the mass concentration of element A

N is Avogadro's number

w_A is the fluorescent yield from A

A_A is the atomic weight of A

ρ and t the density and thickness of the film

and Q_A the ionisation cross-section.

The last parameter is equal to the number of ionisations per increment of path length divided by the number of atoms per unit volume i.e. it is a probability of ionisation.

In the above equation the assumption is made that the depth distribution of generated x-rays is constant for thin films, i.e. that the 'Atomic Number Correction' used in bulk material analysis is negligible when thin films are being used. The assumption is here justified. The atomic number correction consists of a backscattering factor and a stopping power factor. In bulk systems some backscattered electrons re-emerge from the specimen

surface. The amount of backscattering depends upon the atomic number of the target; the backscatter coefficient η being defined as the proportion of total incident electrons that re-emerge from the top surface of the sample. Tixier (1979) points out that as this coefficient is very small for thin films, the backscatter factor [$Fb = 1/(1-\eta)$] may safely be ignored.

The stopping power correction factor describes the variation in efficiency of x-ray production with depth and is given by

$$F_s = \text{constant} \Big/ \int_{E_c}^{E_o} \frac{Q}{S}\, dE \qquad 6.6$$

where S, the stopping power is defined as $-dE/d(\rho x)$. Q is relatively insensitive to the minor energy changes that occur when energetic electrons pass through thin foils. Scott (to be published) has shown that a 0.36eV energy loss is predicted for 100KeV electrons passing through a 200nm copper foil. Thus $dE/d\rho x$ is negligible and F_s may be assumed constant for thin films.

6.1.4 X-ray emission and correction procedures

The intensity of x-ray emission differs from that generated due to a number of interactions between x-ray and specimen. Correction procedures aimed at removing such discrepancies are well established for bulk systems. Some of these bulk effects are manifest in thin films while others are negligible. These factors are qualitatively explained and when relevant to thin film situations developed quantitatively.

Absorption

X-ray absorption occurs when the x-ray's energy is used up within the specimen. The most important relevant mechanism (in magnitude) is the photoelectric effect. The x-ray photon's energy is completely absorbed by an atom and an electron is ejected.

The power of an absorber may be expressed by Beer's Law viz:

$$I_{emitted} = I_{generated} \exp(-\frac{\mu}{\rho}. \rho x) \qquad 6.7$$

where $\frac{\mu}{\rho}$ is the mass absorption coefficient ($cm^2\ g^{-1}$), ρ is the density of the absorber (gcm^{-3}) and x the x-ray path length through the absorber (cm).
Leroux's (1961) expression:

$$\frac{\mu}{\rho} = \text{constant}. \lambda^n \qquad 6.8$$

(where n is dependent on atomic number and x-ray energy) is generally used to predict mass absorption values. They have also been extensively tabulated for characteristic lines in pure elements by Heinrich (1966).

For the geometry in an electron probe microanalyser the mass path length of the x-rays is equivalent to ρz cosec ψ (see Fig. 62), where ψ is the take-off angle defined as the angle between the x-ray detector and the specimen surface, the angle being measured in the plane of the detector. For x-rays generated from an increment $d\rho z$ at a depth z the generated intensity is $\phi(\rho z).d\rho z$. it can be seen that the fraction emitted from the surface at an angle ψ is

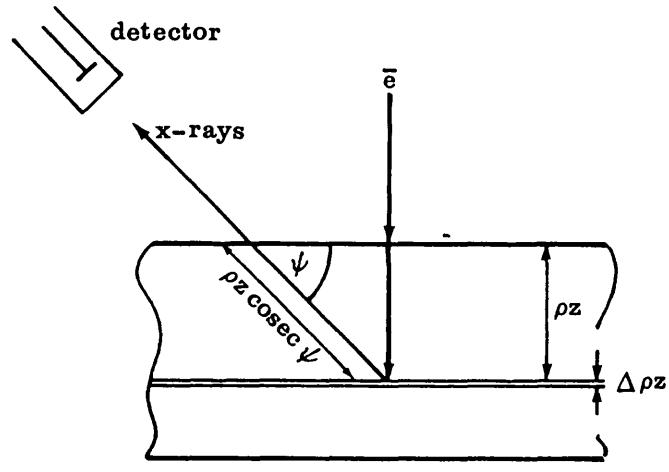

Fig. 62 Absorption path lengths in a conventional probe situation.

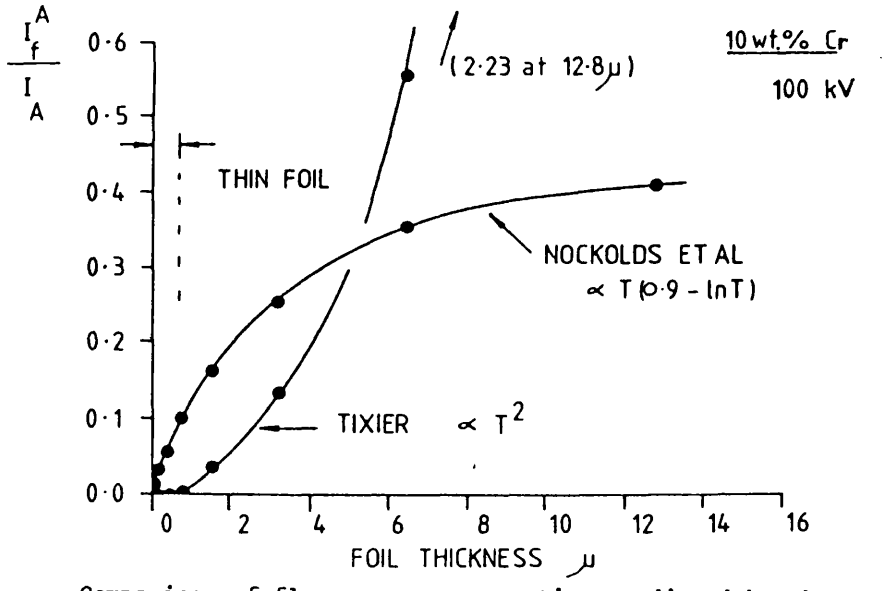

Comparison of fluorescence correction predicted by the present model and that of Tixier for a 10 wt%Cr - 90 wt%Fe alloy as a function of thickness.

Fig. 63 (After Nockolds et al, 1980).

$$dI = \phi(\rho z).\ \exp\left(-\frac{\mu}{\rho}.\ \rho z\ \text{cosec}\ \psi\right)d\rho z \qquad 6.9$$

and the total emitted intensity becomes

$$I = \int_{o}^{\infty} \phi(\rho z).\ \exp\left(-\frac{\mu}{\rho}.\ \rho z\ \text{cosec}\ \psi\right)d\rho z \qquad 6.10$$

As the total generated intensity is $\int_{o}^{\infty} \phi(\rho z).d\rho z$ the absorption factor may be defined as

$$\frac{\int_{o}^{\infty} \phi(\rho z).\exp\left(-\frac{\mu}{\rho}.\ \rho z\ \text{cosec}\ \psi\right)d\rho z}{\int_{o}^{\infty} \phi(\rho z)\,d\rho z} \qquad 6.11$$

This ratio is usually termed $f(\chi)$ where $\chi = \frac{\mu}{\rho}.\ \text{cosec}\ \psi$.

For a thin specimen of mass thickness ρt, where it is assumed that x-ray generation does not vary with depth, the above equation may be reduced to:

$$f(\chi) = \frac{\int_{o}^{\rho t} \exp(-\chi\rho z)\,d\rho z}{\int_{o}^{\rho t} d\rho z} \qquad 6.12$$

which, upon inte gration gives:

$$f(\chi) = \frac{1 - \exp(-\chi\rho t)}{\chi\rho t} \qquad 6.13$$

This correction is easily applicable if the path length through the specimen is known. As this will be proportional to the specimen thickness the possibility of calibrating the absorption phenomenon to measure this parameter exists.

Fluorescence

Primary x-rays absorbed by the specimen can cause the ejection of electrons. If these are from the inner atomic shells, the return to the ground state may be accompanied by x-ray emission. This secondary fluorescence can occur for characteristic and continuum radiation and is of maximum intensity when the energy of the primary x-ray just exceeds the critical excitation energy of the electron shell giving rise to the fluorescence. The magnitude of the effect is very small in comparison with primary excitation levels. Also the depth distribution for secondary generation is more spread out, thus making its effect even less pronounced in thin films.

Philibert and Tixier (1975) have investigated the magnitude of fluorescence in thin films and conclude that characteristic fluorescence is negligible if $\left(\frac{\mu}{\rho}\right)^{AB}_{B} . \rho x < 0.1$ where element B is the potential fluorescer of element A in a binary system. Nockolds, Nasir, Cliff and Lorimer (1980) dispute this criterion, arguing that fluorescence can occur in much thinner films of certain materials. Lorimer (1977) encountered significant fluorescence of chromium in thin films of low %Cr-Fe alloys. The thin film limits predicted by both criteria for a 10% Cr-90% Fe alloy are shown in Fig. 63.

Work to date indicates that continuum fluorescence is a very minor effect which is of negligible magnitude in thin films.

6.1.5 X-ray detection

X-rays will be generated in all directions from an electron irradiated specimen and only a proportion of this total yield can be measured. In the present study an energy dispersive spectrometer was used to detect the x-rays. This basic concept of the detector is described in section 2.3.

6.2 Preparation of specimens

Specimens of copper, stainless steel and an Al-Cu alloy (designated P89) of composition given in table 1 were prepared by the normal procedure for obtaining electropolished samples given in section 3 and table 2.

Some specimens, suspected of having surface artefacts present were ion beam cleaned. This was performed in an Edwards IBT 200 ion beam thinning machine. The sample, a TEM disc pre-thinned by electropolishing, was made the target in an evacuated chamber. To either side of the specimen and pointing at it, argon ionising guns were positioned. In these guns commercially pure argon gas is introduced through a hollow anode-cathode arrangement set at a potential of 5kV. The argon atoms are stripped of their outer shell electrons and the resulting ions are accelerated towards the specimen. The argon ions literally knock atoms off the specimen thus thinning it. Figure 64 is a schematic view of the arrangement within the thinning chamber. An initial vacuum pressure of 5×10^{-5} torr was obtained prior to thinning. With a potential of 5kV applied across the electrodes the

Fig.64

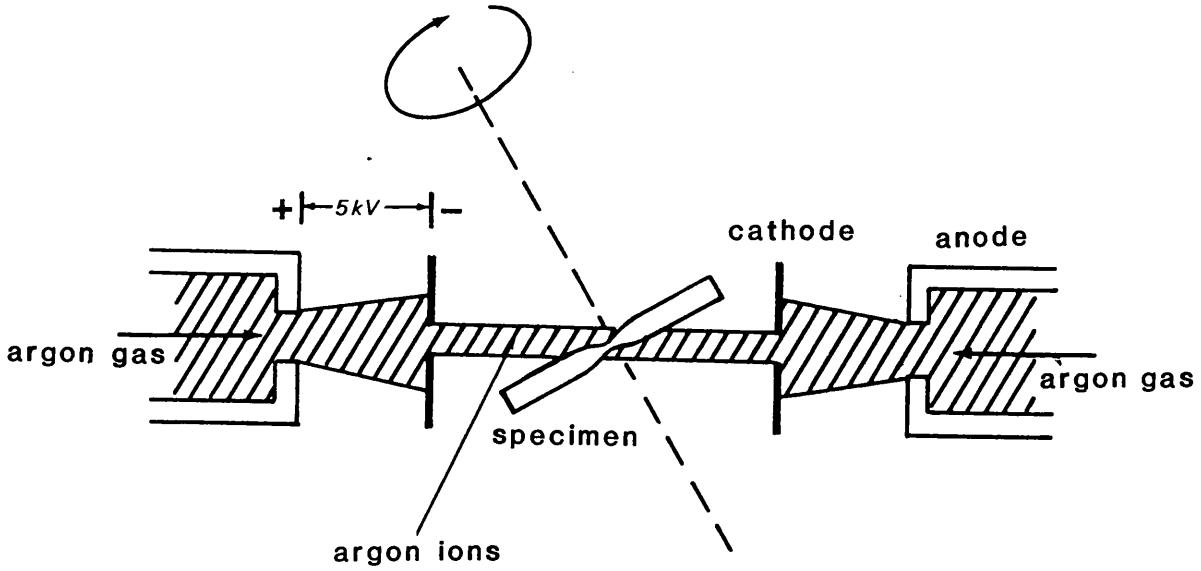

Fig. 64 Schematic view of ion-beam thinner.

argon gas was introduced at a rate which gave a specimen current of 30 to 40μA. The specimen was tilted so that the angle of incidence of the ion beam was approximately 10^{o}. This was found to give a very gentle rate of surface removal (< 0.5μm per hour for the materials used). To ensure an even rate of surface removal the specimen holder was rotated slowly but continuously during the thinning. A binocular focussed on the specimen was used to decide the termination point of the thinning procedure; the increased size of the specimen perforation indicating the extent of surface erosion.

6.3 Production and processing of x-ray data

Production

To optimise the reproducibility of x-ray readings, instrumental operating conditions were kept constant whenever possible. A beam current of 100μm and a specimen current of $\approx 2 \times 10^{-10}$A at an operating voltage of 100kV were employed.

The whole x-ray spectrum in the energy range 0 - 16 KeV was recorded over a specified time interval for each area of interest. Within this spectrum pre-set energy windows, each consisting of 9 individual channels of 20eV width, collected data on the various characteristic lines, their backgrounds and the continuum.

'Hole counts' taken through the specimen perforation at regular intervals provided details of any extraneous radiation coming from the instrument.

The specimen holder was made of beryllium which, by virtue of its low atomic number (Z = 4), has a low absorption coefficient for most x-rays.

The specimen was positioned eucentrically to ensure that it was coplanar with the EDS detector, the azimuth angle being approximately 45^{o} (see Fig. 65). A tilt angle of 30^{o} towards the EDS detector was employed during the analysis periods. This constant value was chosen because the x-ray path length through the specimen and therefore the magnitude of absorption and fluorescence effects are a function of tilt angle. Tilt angles other than 30^{o} gave poorer x-ray yields due to absorption in the specimen and/or beryllium holder.

Under the previously outlined pre-conditions, tapering foils were analysed as follows. A row of contamination spots was deposited under standard conditions (I = 2 x 10^{-10}A, deposition time = 30 seconds) with the foil tilted 30^{o} towards the detector. After photographing the separated spots to determine foil thickness the original 30^{o} tilt angle was regained and the liquid nitrogen anti-contamination trap primed ready for the x-ray analyses.

Individual spots were focussed and centred on the cathode ray image tube at high magnification in the STEM mode. Spot mode was depoloyed (stationary beam) and the x-ray spectrum recorded over a 40 second period; this time being considered sufficient to

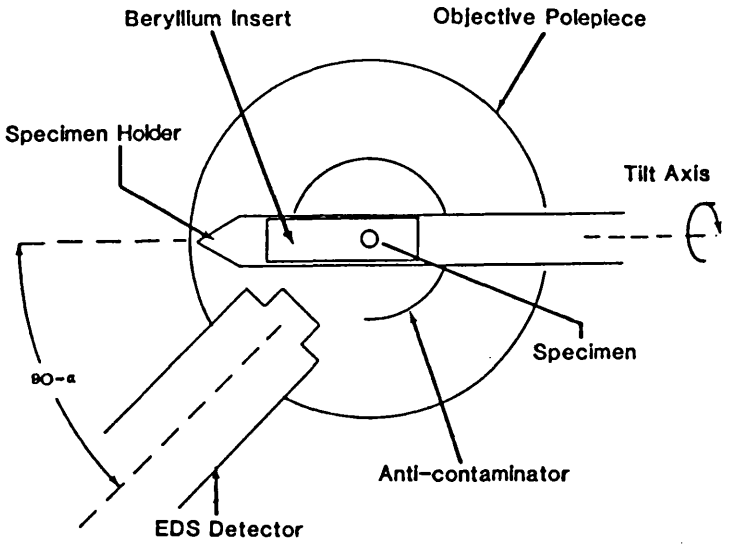

Fig. 65 Plan view of electron microscope column.
α = the azimuthal angle between specimen and detector.

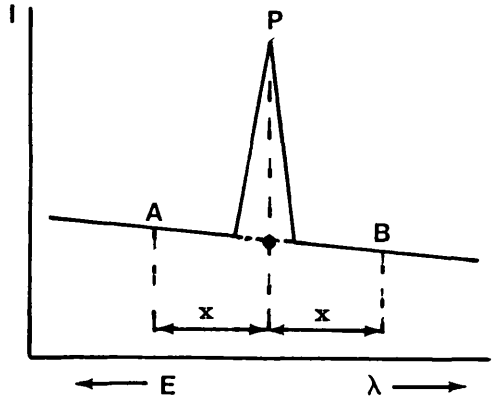

Background at $P = \frac{I_A + I_B}{2}$

Fig. 66 Background stripping from a characteristic peak.

produce statistically significant counts while at the same time minimising specimen drift. At least three spectra were obtained for each spot position, the contamination spot image being re-centred on the screen, if necessary, between analyses. The acceptable criterion for specimen drift was that the beam position after each analysis lay within the confines of the original spot perimeter i.e. a maximum lateral movement of approximately 70 nm. In practice the drift was usually much less and in most cases no discernable displacement was observed even at maximum (300K) magnification. This analysis procedure was repeated for all the other deposited spots.

At the end of each operating session the electron beam was centred on the specimen perforation and the 'hole count' recorded under the same conditions as the other spectra. This hole count, when present is due to extraneous x-rays from unwanted sources and causes distortion of the specimen spectra. Unwanted radiation can be produced by electrons interacting with the condenser apertures and from uncollimated electrons striking the specimen and its surroundings. The various sources of such radiation have been described by Goldstein and Williams (1977, 1978) and many ways of eliminating this unwanted effect have been investigated. These include coating the inside of the specimen chamber with a low atomic number material to reduce continuum radiation (Intensity $\propto Z^2$) as described by

Nicholson, Robertson and Chapman (1977) and/or introducing extra apertures into the condenser system to remove x-rays and uncollimated electrons. In the present study the manufacturers 'hard x-ray kit' was employed which basically comprised thick molybdenum (Z = 42) apertures inserted in the condenser system. This had the effect of reducing the hole count to a negligible level.

Background stripping

Energy windows to measure the background radiation level were set up, usually equidistant and close to the characteristic peaks. It was assumed that the background changed linearly over small energy ranges and hence to record the background below the characteristic peak at P (Fig. 66), the readings at A and B were averaged. This value was then subtracted from the total peak count to give the stripped value.

When the two background windows could not be placed equidistant from the characteristic peak, as for example with stainless steel analyses where K_β lines from one element were very close to K_α of the next element, an appropriate weighted mean of background values was used.

Statistical treatment

From a single (40 second) analysis the standard deviation of the counts in one channel is given by $\sigma = \sqrt{n}$ where n is the total number of counts in that channel. This is because a Poisson type variation governs the height distribution of each single channel, see

Fig. 67a. For more than one channel the standard deviation is $\sigma = \sqrt{N}$ where N is the total number of counts in all the channels used. However, when for example three separate counts are made, Fig. 67b, the standard deviation of the mean is the relevant measure of confidence. This, for three counts, is given by

$$SD = \frac{\sqrt{A+B+C}}{3} \qquad 6.14$$

Hence the statistical confidence in the mean improves with the number of readings taken.

The uncertainty in characteristic peak measurement and characteristic ratios was assessed using the following standard analysis.

For two characteristic peaks A and B with their accompanying backgrounds a, a′ and b, b′, where a and a′ are equidistant from A and similarly b and b′ are equidistant from B

$$I_{corrected} = I_A - \left(\frac{I_a + I_{a'}}{2}\right) \qquad 6.15$$

For any function

Y = function $(x_1\ x_2\ \ldots\ x_n)$ where all parameters are quoted with the same level of confidence

$$W_y = \left[\left(Wx_1\ \frac{dY}{dx_1}\right)^2 + \left(Wx_2\ \frac{dY}{dx_2}\right)^2 + \ldots + \left(Wx_n\ \frac{dY}{dx_n}\right)^2\right]^{\frac{1}{2}} \qquad 6.16$$

W_y = uncertainty in Y

Wx_1 = uncertainty in x_1 etc.

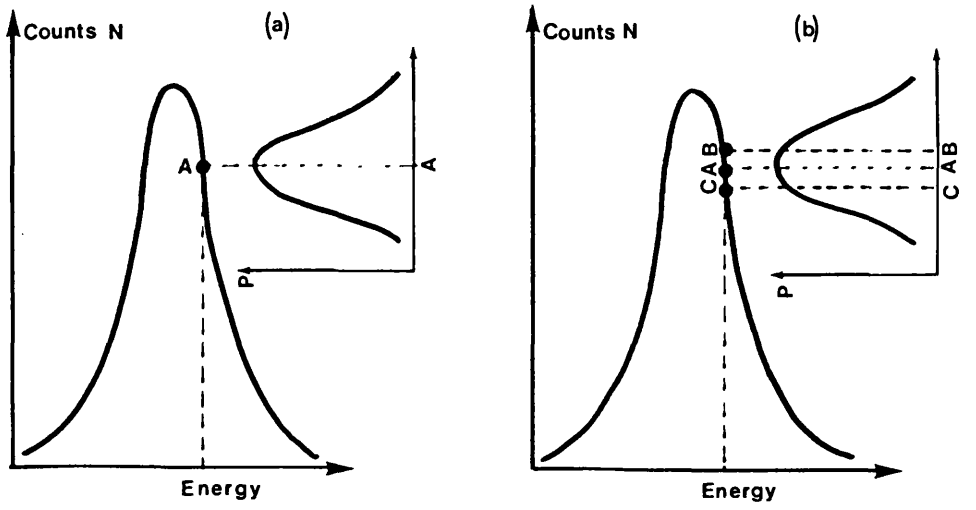

(a) The standard deviation $\sigma = \sqrt{N_A}$

(b) The standard deviation of the mean $\sigma_\mu = \frac{\sqrt{N_A + N_B + N_C}}{3}$

Fig. 67 The statistical confidence in a single x-ray count (a) and a multiple count, (b).

Therefore for the intensity of peak A defined by equation 6.15

$$SD_{I\ CORRECT} = \left[\left(SD_{I_A}\frac{dI_{CORRECTED}}{dI_A}\right)^2 + \left(SD_{I_a}\frac{dI_{CORRECTED}}{dI_a}\right)^2 + \left(SD_{Ia'}\frac{dI_{CORRECTED}}{dI_{a'}}\right)^2\right]^{\frac{1}{2}} \qquad 6.17$$

Similar treatments are applicable to peak B and to the ratio I_A/I_B. In cases where the two background measurements are not equidistant from the peak, equation 6.15 must initially be modified prior to the uncertainty analysis.

6.4 Reproducibility of x-ray measurements

6.4.1 Variable analysis positions

The x-ray yield may be affected by absorption in the beryllium specimen holder and if so the magnitude of such an effect would be a function of the analysis position.

To investigate the presence and magnitude of such an effect a specimen 'sandwich' was analysed. This consisted of a nickel grid coated by evaporation with a thin (30nm), uniform aluminium layer followed by a thin (25nm), uniform copper layer. A carbon film had initially been floated off a glass slide onto the grid to give support to the deposited metal films. For flat, uniformly deposited films, any variation in the CuKα/AlKα ratio reveals the extent of absorption in the beryllium holder. This is because AlKα is preferentially absorbed

by beryllium ($\frac{\mu}{\rho}^{AlK\alpha}_{Be}$ = 150.7, $\frac{\mu}{\rho}^{CuK\alpha}_{Be}$ = 1.2).

Figure 68a shows a photograph of the grid in position and tilted 30^{o} towards the detector while the schematic view below shows how the CuKα/AlKα ratio varied with analysis position. It can be seen that the upper left hand quadrant of the grid, which is most shielded by the specimen holder, suffered the greatest degree of AlKα absorption. In view of these results care was taken to perform all thin foil analyses on areas of specimen least affected by absorption in the beryllium specimen holder viz the lower right hand quadrant in Fig. 68b.

6.4.2 Variable analysis conditions

The variation of x-ray spectra with time was investigated using a Cu 4% - Al alloy (P89). The specimen was prepared by the electropolishing technique, the sample composition and electropolishing conditions being given in tables 1 and 2 respectively. Analyses were repeated at two minute intervals on the same area of foil, the count period being 40 seconds.

Figure 69 shows that no observable change in the CuKα or AlKα occurred during a single operating session but re-examination after a 24 hour period revealed that both counts were lower by approximately 6%. As no measurable change occurred in the AlKα/CuKα ratio it was concluded that the overnight reduction in count rate was not due to increased absorption in a growing surface film. Such a mechanism would result in the preferential absorption of the less energetic AlKα x-rays which would be reflected in

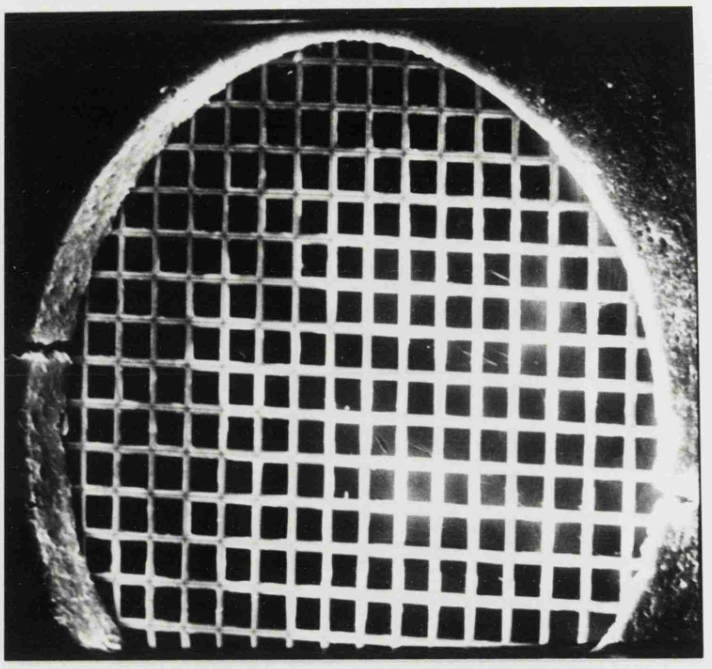

(a)

tilt direction

Mag. = x50

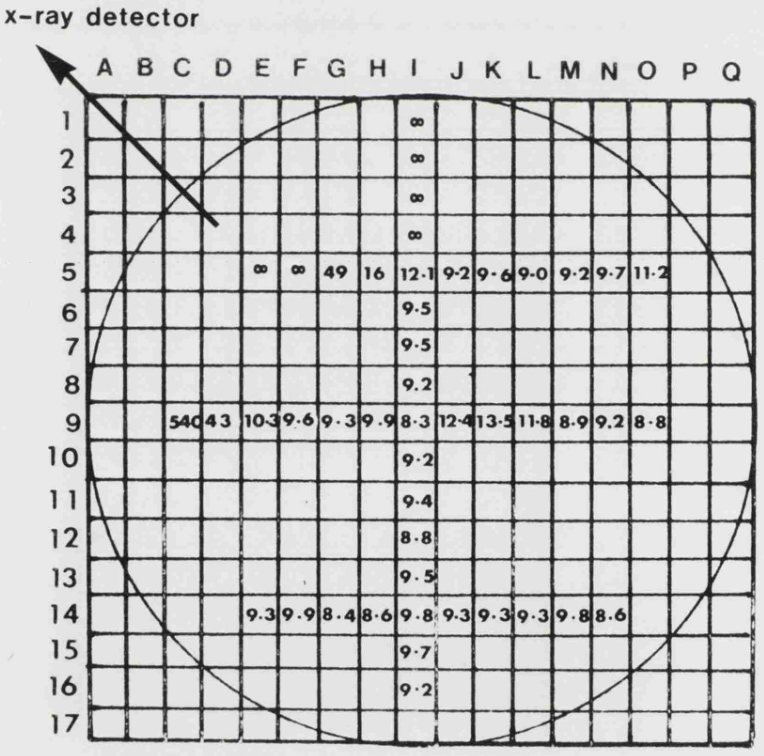

(b)

Fig. 68

(a) Cu- Al coated grid tilted towards the x-ray detector

(b) variation of CuK_α / AlK_α ratio with analysis position.

Fig. 69

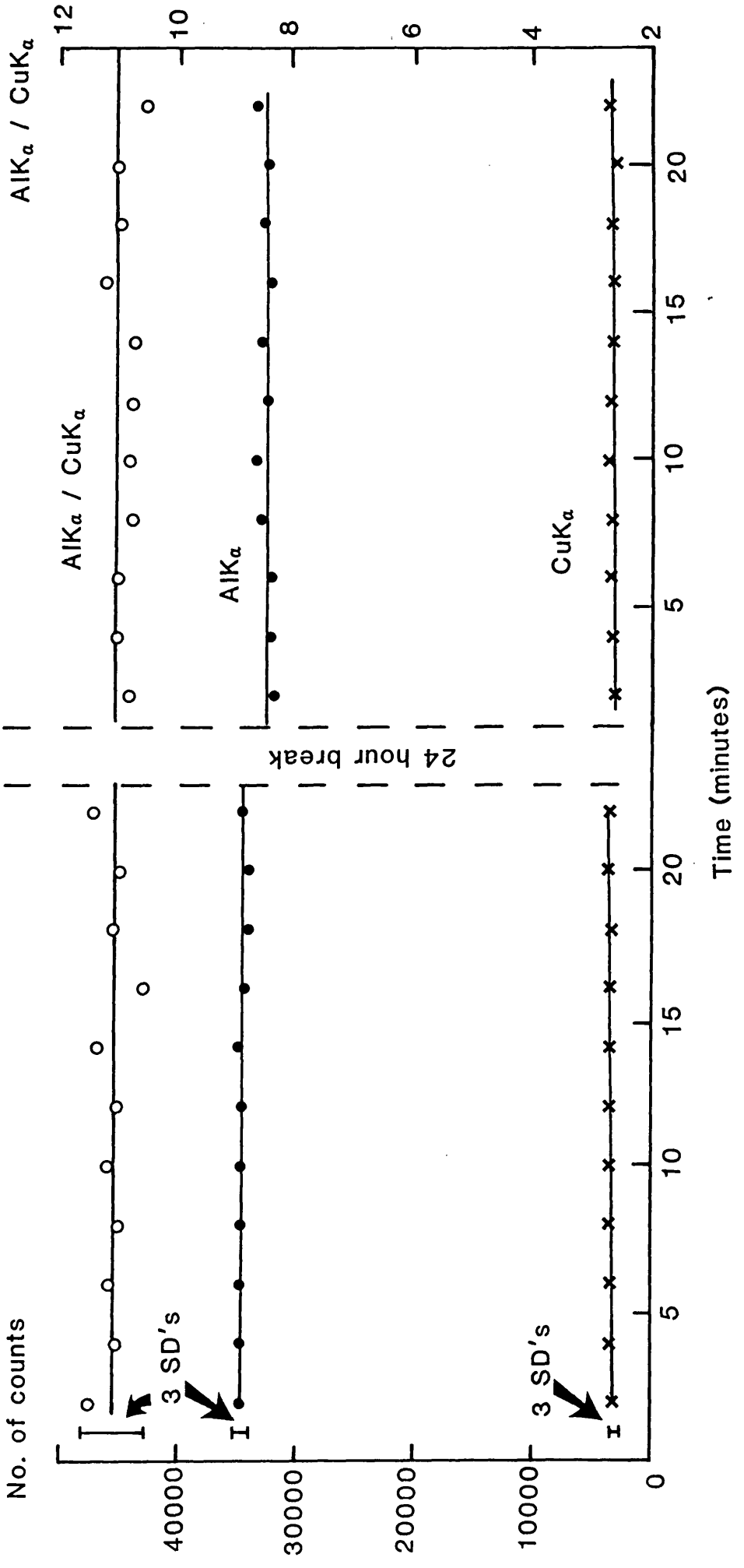

Fig. 69 Variation of x-ray yield with time for a Cu4%- Al specimen.

a reduced AlKα/CuKα ratio. Rather it was concluded that a small reduction in the specimen current had affected the generation of both characteristic x-rays equally.

The above experiment reveals both the insensitivity of characteristic ratios and the sensitivity of individual characteristic measurements to changes in operating conditions.

6.5 Effect of foil thickness on the x-ray yield from a copper specimen

The variation of characteristic and continuum spectra with thickness for a copper specimen was investigated. The specimen, composition given in table 1, was electro-polished using the conditions outlined in table 2. The beam direction thickness of the specimen when tilted 30^{o} towards the E.D.S. detector was measured at many points using the standardised contamination spot technique. The thickness values were 'corrected' using figure 48 to give the true metal thickness.

The analyses were carried out in the areas marked by the contamination spots; in each position at least three 40 second analyses being performed.

Figure 70 shows the variation of CuKα, CuLα, the low energy continuum and the high energy continuum with foil thickness. All curves appear to be approximately linear, the extrapolated CuKα and 10KeV continuum curves intercepting the origin while those of the CuLα and 1260eV continuum appear to have positive count intercepts at zero thickness. In practice no count is actually observed at the edge of the foil perforation and the apparent

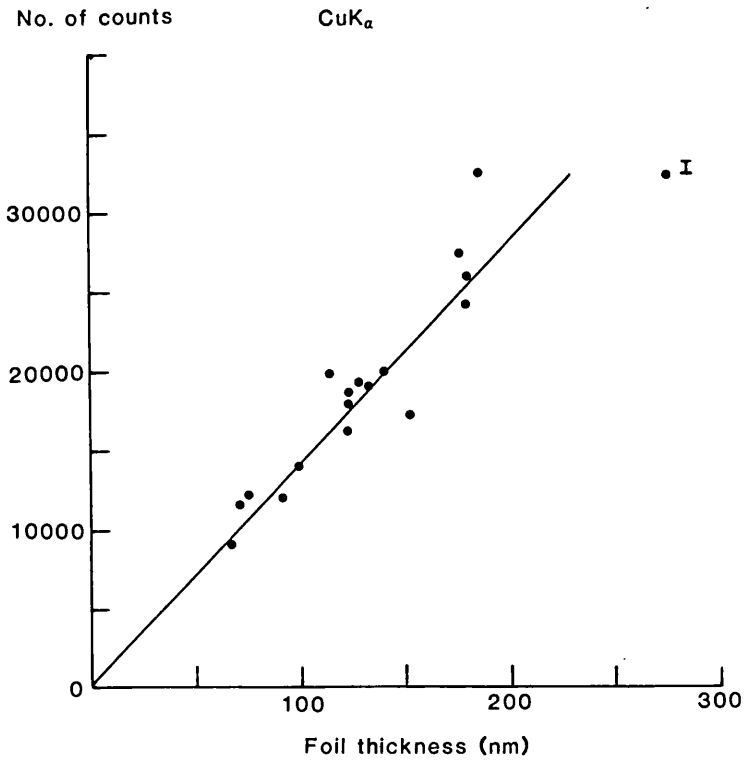

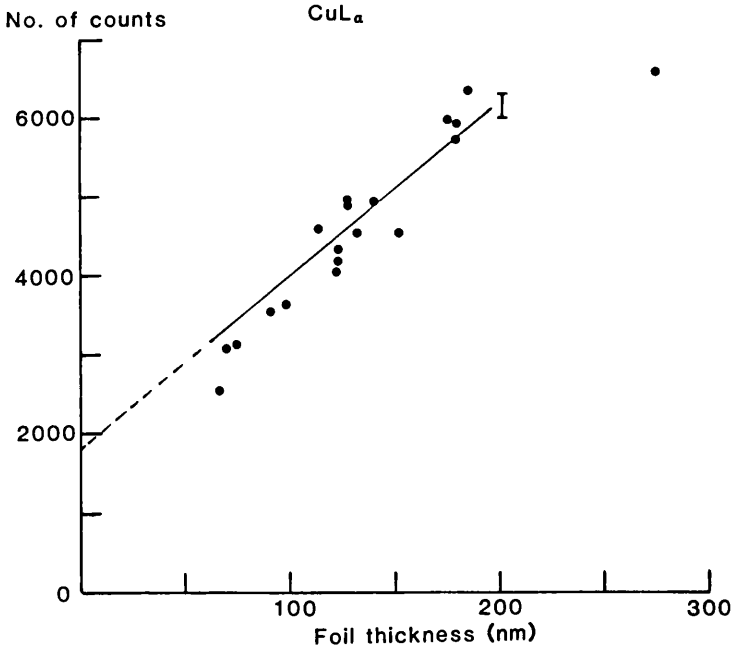

Fig. 70 Characteristic intensity variation with foil thickness for a copper specimen.
(Error bars= ±3SD's of the mean).

Fig. 70 ctd.

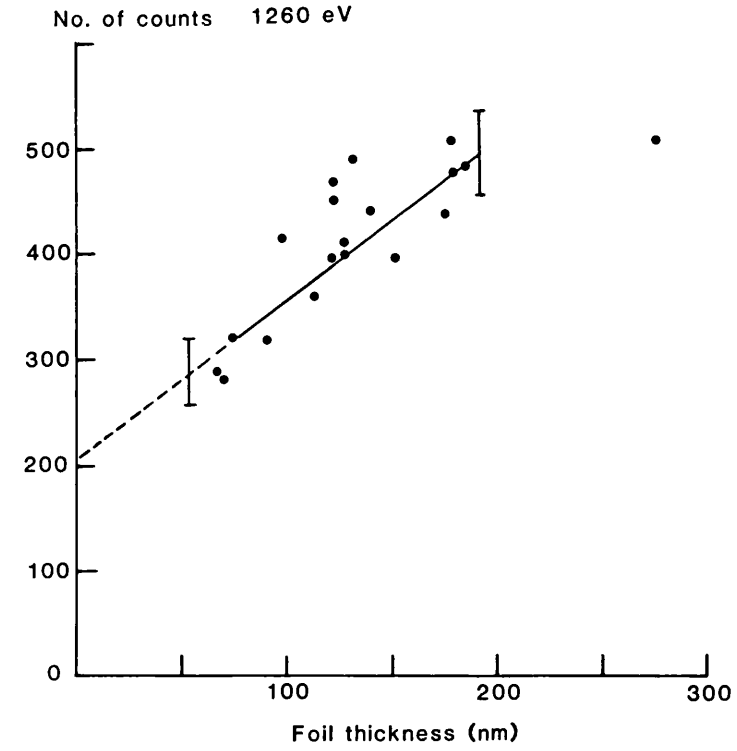

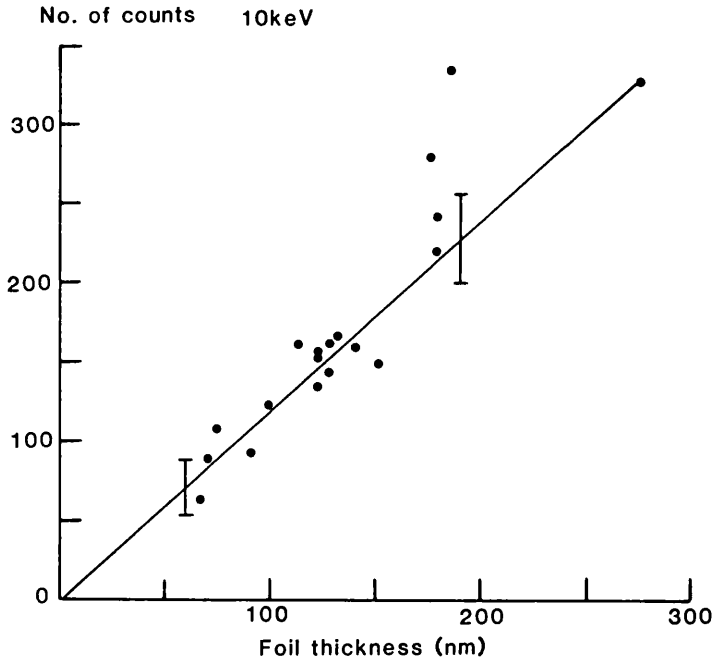

Fig. 70 ctd. Continuum intensity variation with foil thickness for a copper specimen.

extrapolated intercept is due to the increasing absorption of the low energy CuLα and 1260eV spectra in the specimen as foil thickness increases. Such an effect is much less pronounced for the higher energy CuKα and 10KeV spectra which have lower mass absorption coefficients

$$\left[\left(\frac{\mu}{\rho}\right)^{Cu}_{CuK\alpha} = 53.7,\ \left(\frac{\mu}{\rho}\right)^{Cu}_{CuL\alpha} = 1586,\ \left(\frac{\mu}{\rho}\right)^{Cu}_{1260eV} \approx 9000,\ \left(\frac{\mu}{\rho}\right)^{Cu}_{10KeV} \approx 200\right].$$

This absorption effect is discussed quantitatively in section 6.6 where the influence of thickness on characteristic and continuum ratios is discussed. It can be seen qualitatively in Fig. 71 which shows the spectra from a thin and thick area of a copper specimen. The vertical scale in the lower picture is 10x that of the top picture but it can be appreciated that the CuLα:CuKα ratio has diminished with increasing thickness.

The experimental scatter of the results in Fig. 70 is excessive and if the individual x-ray intensities were used as a measure of thickness large errors would result (up to ± 50nm). The systematic deviations, where CuKα, CuLα, 1260eV and 10keV all appear to show the same bias, are considered to arise in the x-ray generation process due to unstable conditions of specimen current. Non systematic deviations are considered to be due to absorption effects in a non uniformly tapering foil. This is discussed at the end of the next section.

Fig.71

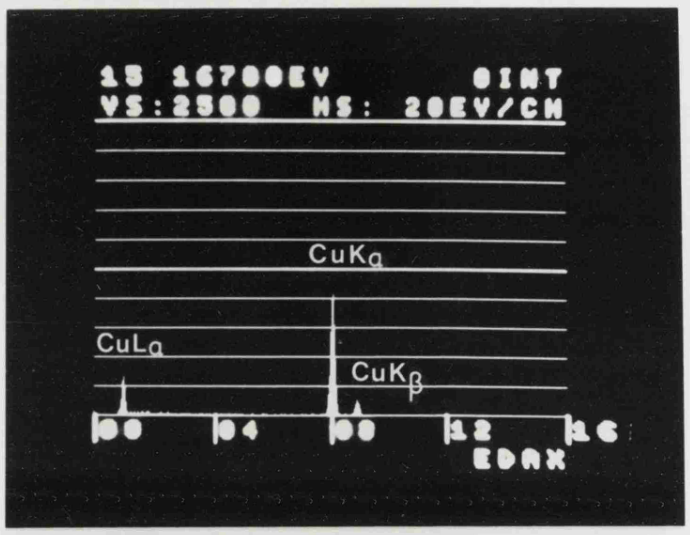

(a)

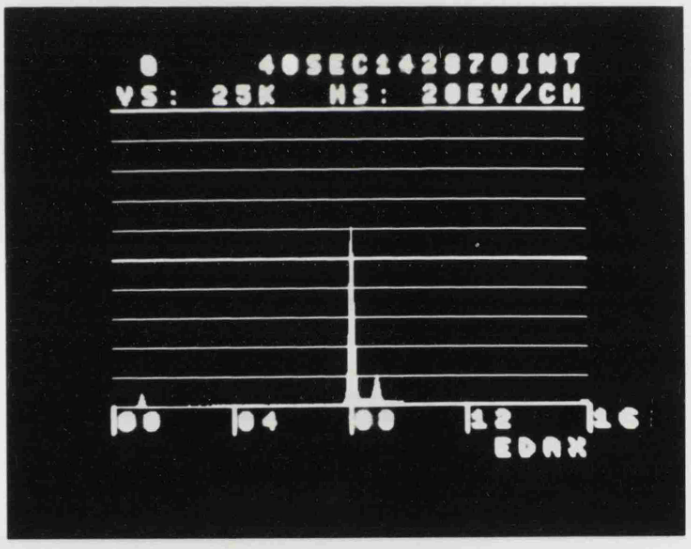

(b)

Fig. 71

X-ray spectra obtained from thin and thick regions of a copper foil.

(a) Thickness in beam direction, $h \ll 50nm$

(b) " " " h = 100nm.

6.6 Absorption effects in copper and their potential use in establishing foil thickness

Equation 6.13 which may be written more fully as:

$$f(\chi) = \frac{1 - \exp\left(-\frac{\mu}{\rho}\rho t \operatorname{cosec}\psi\right)}{\frac{\mu}{\rho}\rho t \operatorname{cosec}\psi}$$

predicts the theoretical effect on x-ray absorption of parameters such as foil density and thickness, the mass absorption coefficient and the x-ray take-off angle. Figure 72 is a plot of $f(\chi)$ data versus foil thickness for CuLα and CuKα characteristic lines. It can be seen that the theoretical absorption of CuLα changes significantly with thickness while the CuKα, with a much lower mass absorption coefficient, is relatively insensitive over the same range. It should therefore be theoretically possible to use the ratio of these characteristic lines as a thickness monitoring device.

In order to compare theoretical and experimental absorption results it is important that the parameters used in equation 6.13 are adequately defined. Unfortunately the equation has been derived from the geometrical conditions found in most electron probe microanalysers where the specimen is normal to the electron beam. In the TEM the specimen is tilted towards the detector to optimise x-ray detection and the take-off angle and foil thickness (in the beam direction) therefore differ from those used in the electron probe microanalysis situation.

The TEM geometry and the calculation of take-off angle can be appreciated by reference to Figs. 65 and 73. The

Fig. 72

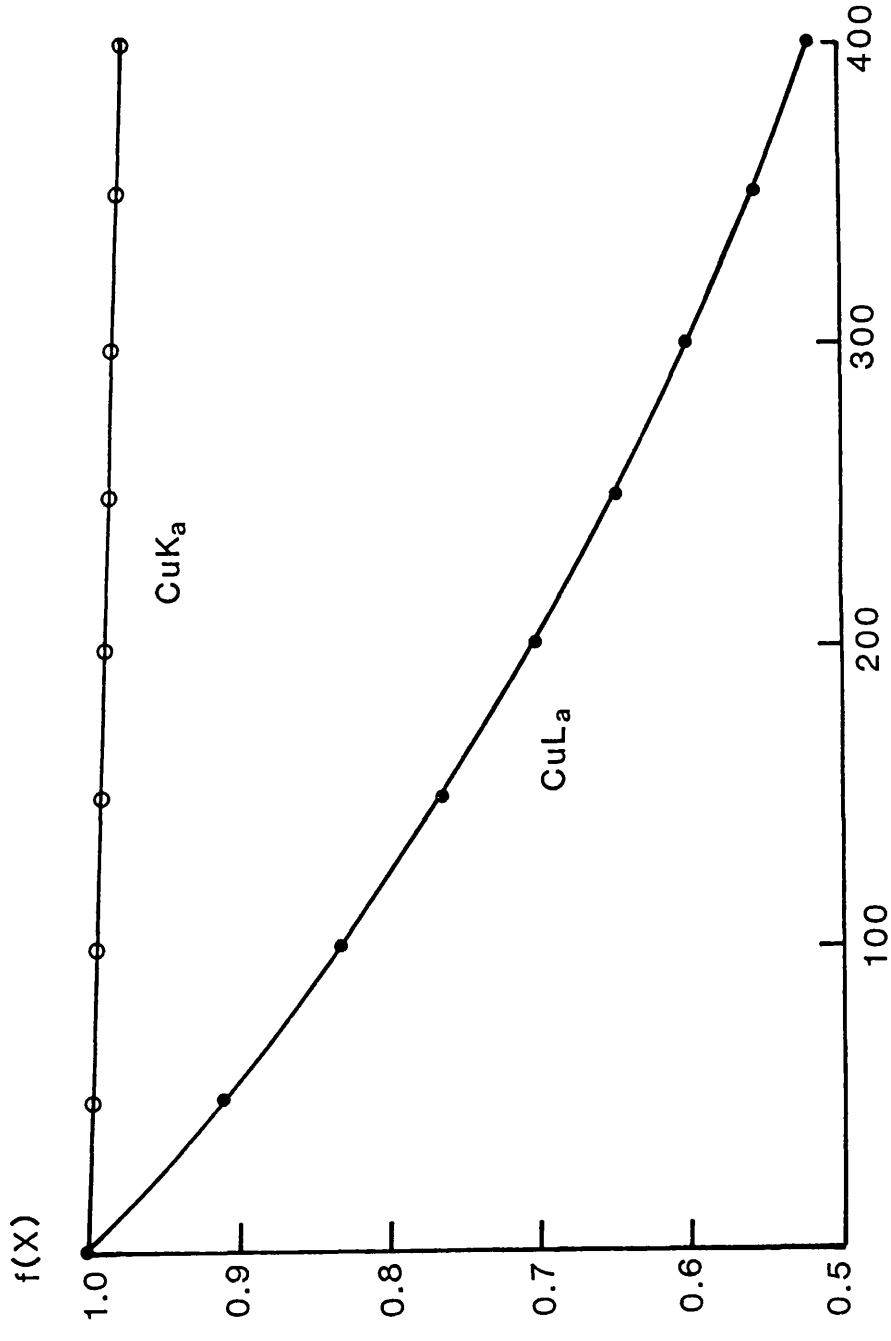

Fig. 72 Theoretical characteristic line absorption in a copper specimen.

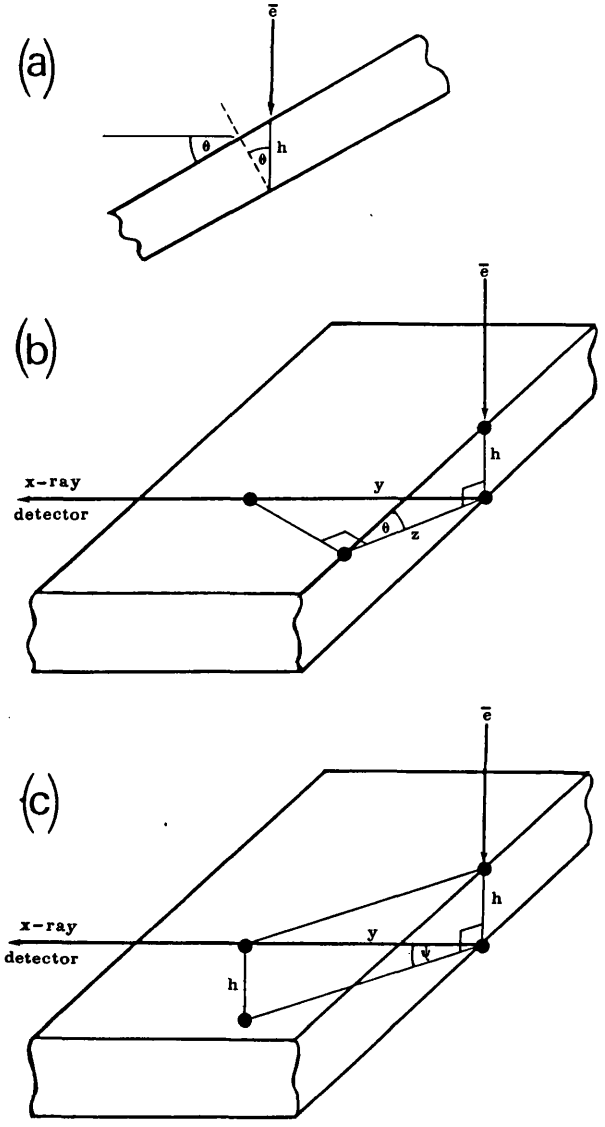

θ = the goniometer tilt angle.

h = thickness in the beam direction.

y = x-ray path length in the specimen

z = horizontal line perpendicular to tilt axis

< zy = the azimuth angle, α (45^{o}).

=> $y = z/\cos\alpha$, $z = h/\tan\theta$

$\therefore\ y = h/\tan\theta\cos\alpha$

$\tan\psi = \frac{h}{y}$ i.e. $\psi = \tan^{-1}\frac{h}{y}$

=> $\psi = \tan^{-1}(\tan\theta.\cos\alpha)$ 6.16

Figure. 73. Determination of the x-ray take-off angle

Fig. 73

correct thickness value to insert into f(χ) equations is 'h', the thickness in the beam direction. Additionally, the x-rays path length through the foil on their journey to the detector no longer equals t cosec ψ but is now h cot ψ as may be seen from Fig. 73(c). The correct equation for use with a tilted specimen is therefore:

$$f(\chi) = \frac{1 - \exp(- \frac{\mu}{\rho} \rho h \cot \psi)}{\frac{\mu}{\rho} \rho h \cot \psi} \qquad 6.18$$

Statham and Ball (1980) and Morris (1979) derive take-off angles using an equation at variance with the one employed in this study. Under close scrutiny it is revealed that values obtained from the two equations may be related by

$$\psi_{RAE} = \mathrm{Tan}^{-1} (\sin \psi_{BALL} . \sec \theta) \qquad 6.19$$

Ball et al's take-off angles have ambiguous physical meaning but are calculated to generate correct values of f(χ) when inserted in equation 6.13. Equation 6.18, based on measurable parameters, is used throughout this study. The importance of determining a correct value of take-off angle can be appreciated in Fig. 74 which reveals the theoretical effect of take-off angle on the CuLα/CuKα ratio obtained from a pure copper sample.

Using the characteristic and continuum results plotted earlier (Fig. 70) the CuLα/CuKα and 1260eV/10keV ratios were plotted as a function of thickness (Figs.75 and 76). In both instances the preferential absorption of one spectral line in the copper specimen leads to a significant

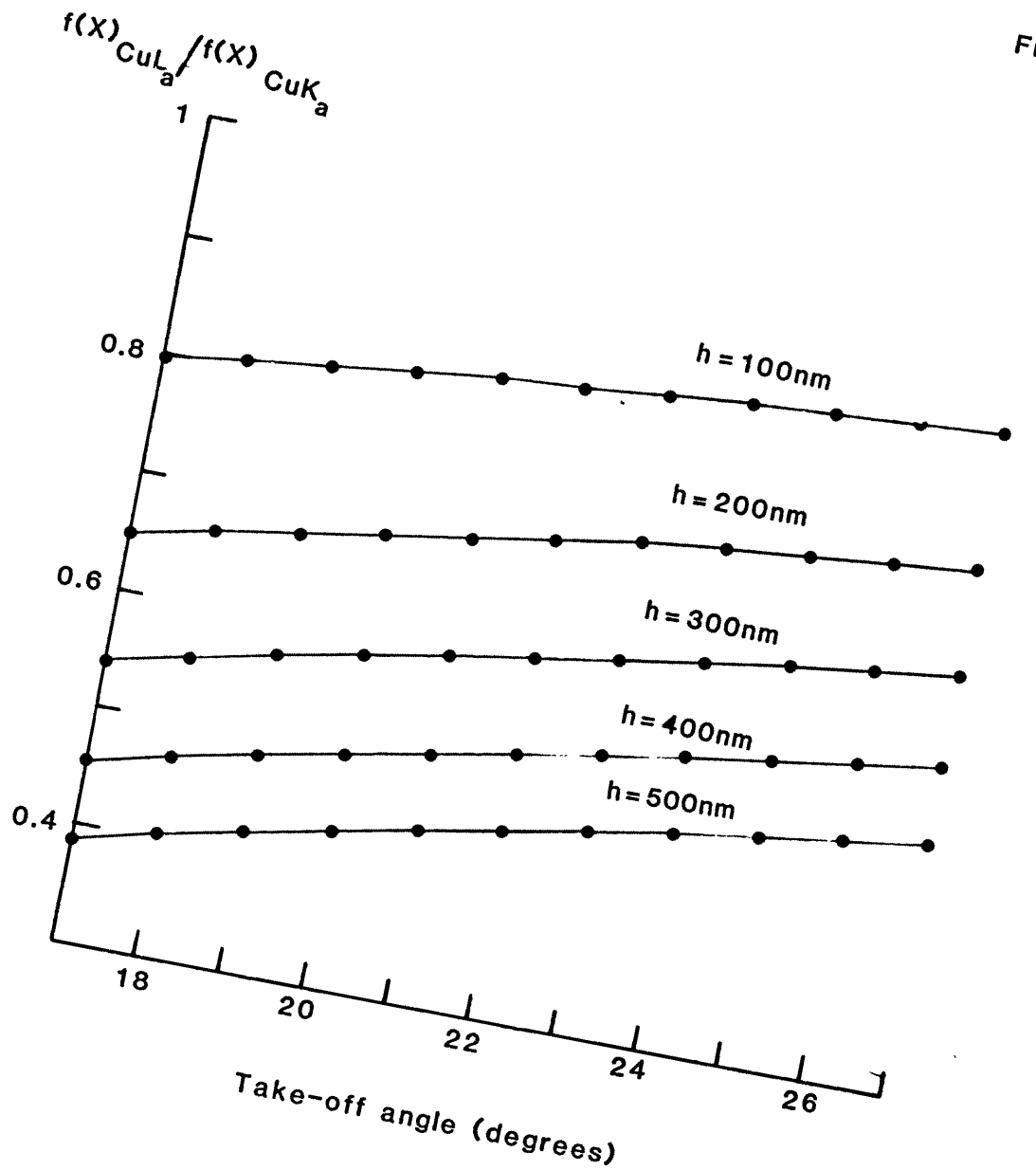

Fig. 74

Theoretical effect of take-off angle on the CuL_a / CuK_a ratio.

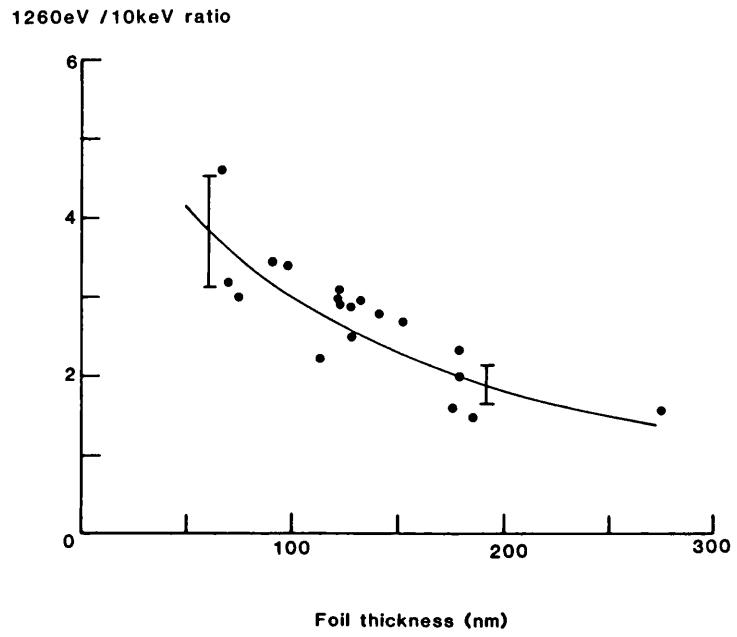

Fig. 75

The variation of the 1260eV /10keV continuum ratio with foil thickness. for a copper specimen.

(Error bars=±3SD's of the mean).

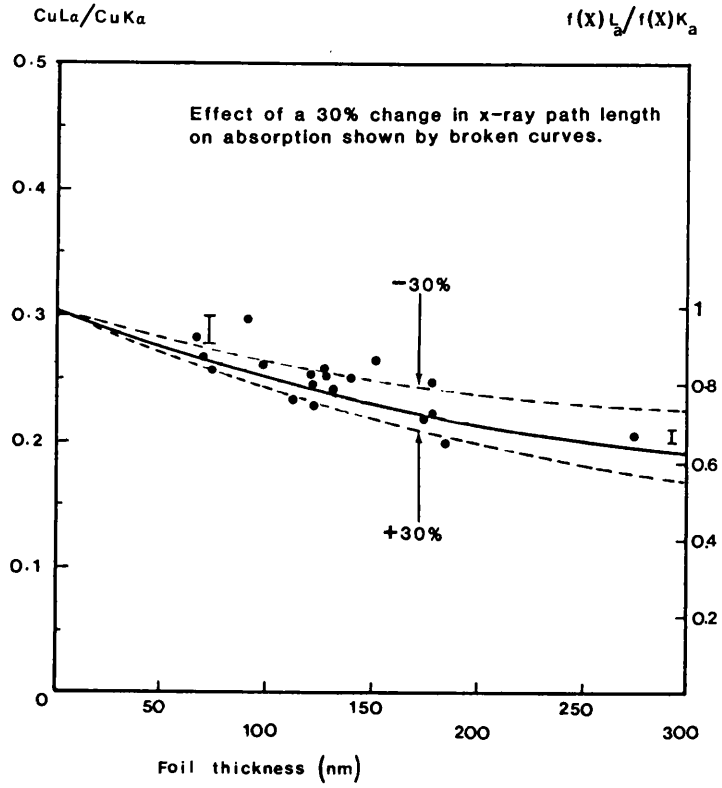

Fig. 76

The variation of CuL_α / CuK_α [• • •] and $f(\chi)_{CuL_\alpha}/f(\chi)_{CuK_\alpha}$ [——]

with foil thickness.

(Error bars=±3SD's of the mean).

variation in the ratio over the thickness range studied.

For the characteristic ratio plot, the effects of absorption were compensated for by multiplying the ratio by an inverse f(X) ratio viz: $(CuL\alpha/CuK\alpha) \times f(X)_{CuK\alpha}/f(X)_{CuL\alpha}$. This produces ratio values which one would obtain from an absorption free area of foil i.e. of zero thickness. These results are plotted in Fig. 77. The average value obtained (0.302) may be multiplied by $f(X)_{CuL\alpha}/f(X)_{CuK\alpha}$ values to produce the theoretical absorption curve for the system. This is shown superimposed on the experimental data in Fig.75.

The experimental characteristic trends are in close agreement with the theoretical predictions. No theoretical curve was predicted for the continuum results as mass absorption coefficients were not unambiguously known. Individual scatter on points is quite large. The systematic errors affecting individual spectra are removed by ratioing results. Non uniformity in the foil profile results in a non-linear relationship between foil thickness and x-ray path length. This could result in two foil regions of equal thickness giving different $CuL\alpha/CuK\alpha$ ratios. Indeed the surface profile cf the wedged foil used in this investigation was not perfectly smooth. The theoretical effect on the ratio of a ±30% change in x-ray path length, considered possible with the particular foil used, is shown by the broken lines in Fig. 75. It can be seen that most results are encompassed within these theoretical boundaries. To date no explanation has been found for

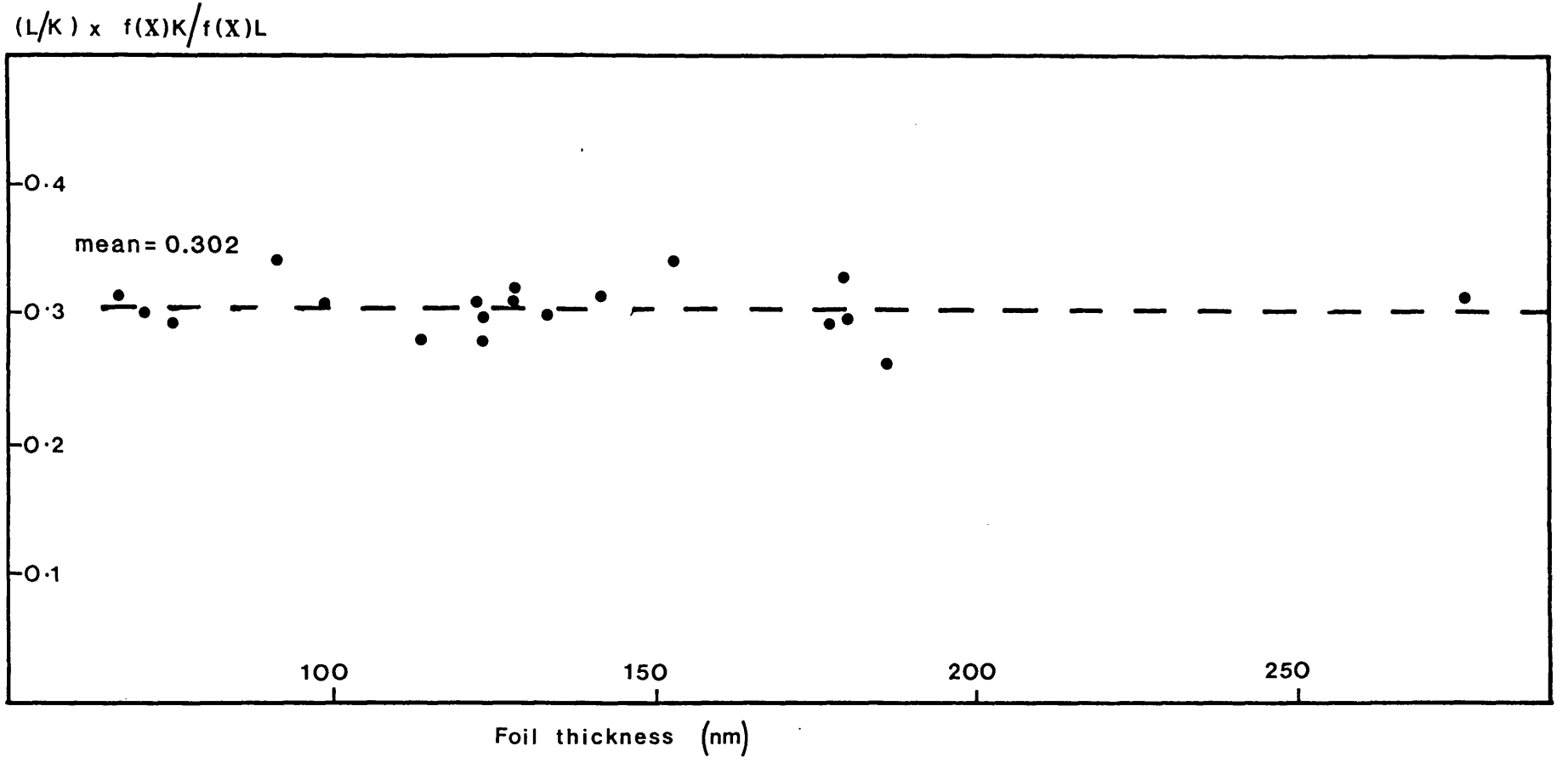

Fig. 77 CuL_α / CuK_α ratios corrected for absorption vs foil thickness.

Fig. 77

the few results lying outside these boundaries. Clearly the individual scatter of the ratio results will produce large potential errors in foil thickness (up to 100nm) if used for this purpose. The same would appear true for the continuum ratio results which also suffer from poor statistical confidence due to low count rates.

6.7 Fluorescence effects in thin stainless steel foils

It was mentioned in sections 1.2.4 and 6.1.4 that Lorimer et al (1977) and Nockolds et al (1980) respectively had encountered fluorescence effects in stainl ess steels. These effects were investigated for the 18.8 stainless steel used previously in this thesis. The individual mass absorption coefficients, see table 10, and the relative positioning of the elements in the periodic table suggest that chromium is likely to be fluoresced by FeKα and NiKα and that iron may be slightly fluoresced by NiKα. This does occur in bulk systems and it was considered that if the effect were present in thin films its variation with thickness could be used to monitor this parameter. Qualitatively one would expect from the relatively high absorption coefficients for NiKα and FeKα in chromium that CrKα would be preferentially fluoresced and that FeKα/CrKα and NiKα/CrKα ratios would therefore decrease as a function of foil thickness. Similarly one might expect some decrease in the NiKα/FeKα for the same reasons.

The variation of the characteristic and continuum radiation with thickness plotted in Fig. 78 reveals a general upward trend with increasing thickness. The

ABSORBER	EMITTER		
	Fe	Cr	Ni
Fe	71.4	113.0	379.6
Cr	474.2	88.2	310.7
Ni	90.0	142.3	58.9
18:8 stainless steel	145.4	110.9	341.5

Table 10. Mass absorption coefficients for Kα lines in stainless steel ($\frac{\mu}{\rho}$ = cm^2 g^{-1}).

Fig. 78

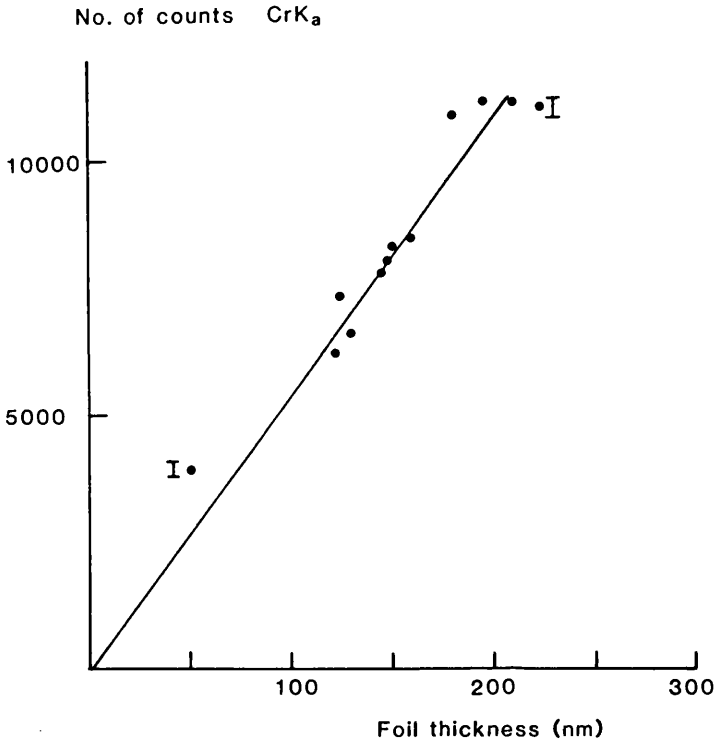

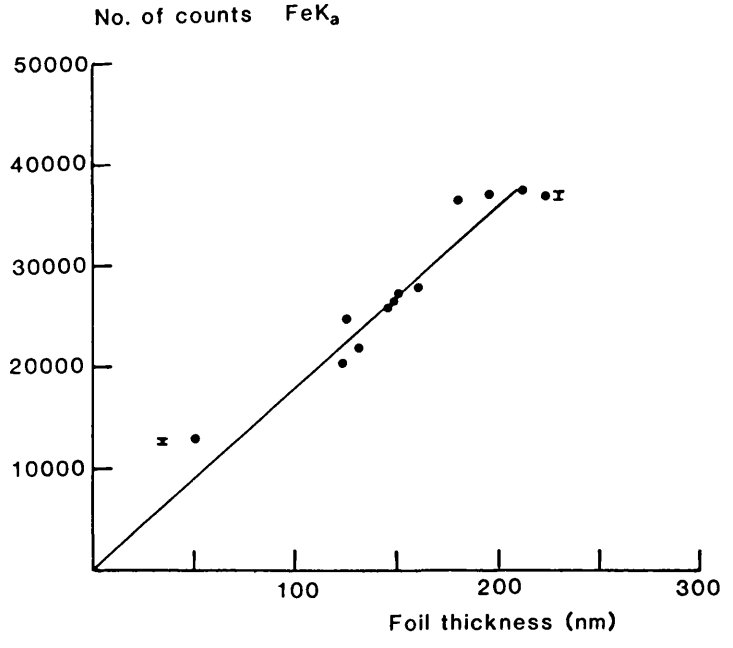

Fig. 78 Characteristic and continuum intensity variation with foil thickness for a stainless steel specimen. (Error bars= ±3S D's of the mean).

Fig. 78 ctd.

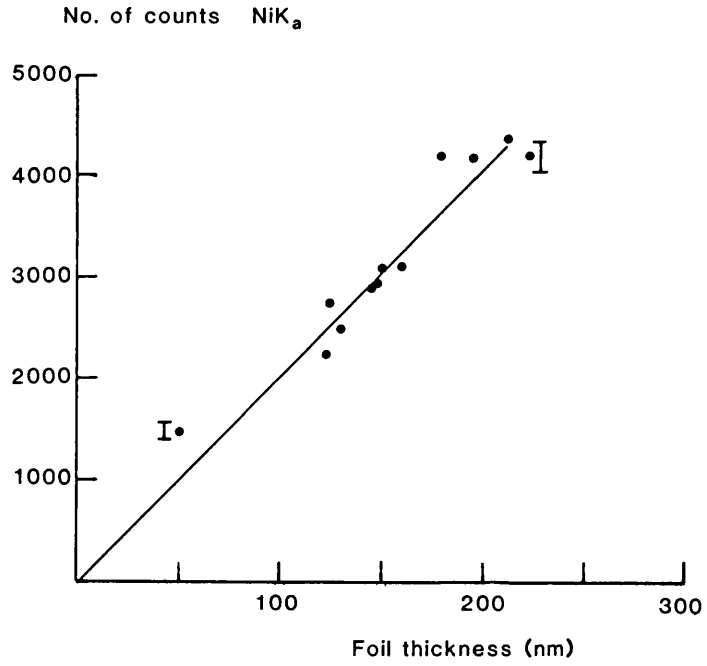

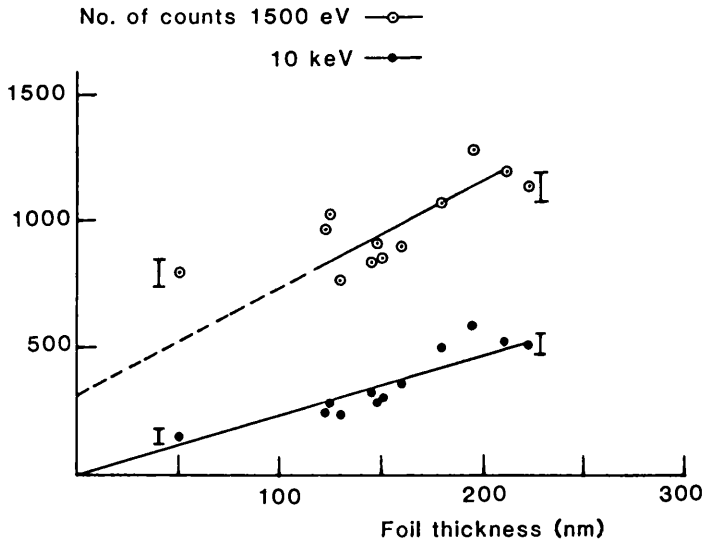

Fig. 78 ctd.

characteristic and high energy curves may be extrapolated to the origin while the low energy continuum curve is suppressed at high values of thickness, due to absorption and consequently appears to have a positive count intercept at zero thickness.

The characteristic and continuum ratios are plotted in Fig.79. No sign of preferential absorption or fluorescence is apparent in the characteristic ratio plots. The absorption coefficients given in table[10] indicate that preferential absorption of characteristic lines is not very pronounced in this system and that any ratio changes would therefore be due to fluorescence effects. Indeed the theoretical NiKα/CrKα ratio, which is most affected by absorption, is over 95% of its absorption free value when the foil thickness in the beam direction is 200nm.

Fluorescence effects are seen to be negligible in this system over the thickness range studied. Such effects may be more pronounced in Fe-Cr alloys with a lower chromium content although Lorimer et al observed fluorescence in foils containing up to 25wt% chromium. From this study it is concluded that the fluorescence effects in an 18.8 stainless steel are so small as to completely rule out their use as a method for measuring foil thickness.

The continuum ratio shows a discernible decline with increasing thickness. The count rate was quite low resulting in the large statistical error bars. If this correlation were used to calibrate thickness typical errors of approximately ±20nm could be expected. More counting periods could reduce this to acceptable levels

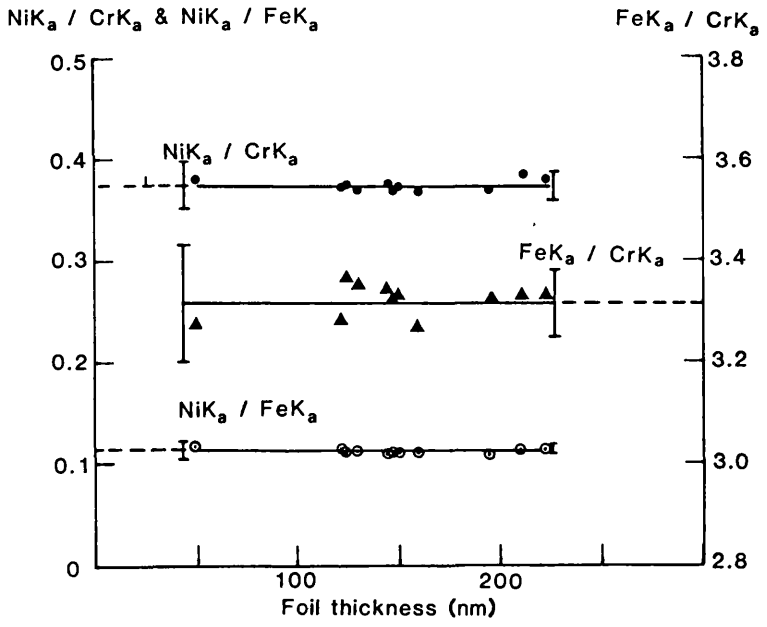

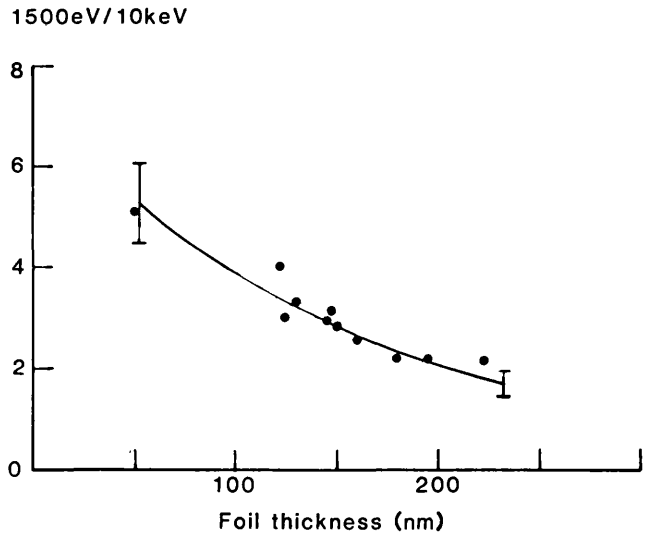

Fig. 79 Characteristic and continuum intensity ratios vs foil thickness for a stainless steel specimen. (All error bars=±3S D's of the mean).

although the experiment would be unduly long as a result. To reduce the error bars to half their size for example would require twelve forty second count periods. This would improve thickness uncertainty from ±20nm to approximately ±10nm.

6.8 Surface film effects in a Cu 4% - Al alloy

The x-ray spectra from a sample of the Cu4%-Al alloy designated P89 were analysed. Initially, a specimen of the solution treated alloy, composition given in table 1, was electropolished using the conditions outlined in table 2. The electropolished foil in this instance appeared to have a smoothly tapering wedge profile, see Fig. 80. The thickness values in this figure were obtained using the standardised contamination spot technique and corrected using the equation given in Fig. 47. Hence the values represent the thickness of the metal measured in the beam direction.

The x-ray spectra were measured in the manner outlined in section 6.3, individual energy windows recording CuKα and AlKα together with low and high energy continuum. The continuum measurements showed an approximately linear dependence on foil thickness, Fig. 81, as did the AlKα characteristic data (Fig. 82). However the CuKα intensity remained constant below h = 200 nm. This change in the relative proportions of CuKα and AlKα intensities may also be observed in Fig. 83. In Fig. 84(a) it can be seen that the change in ratio of the two characteristic lines with foil thickness is appreciable. The phenomenon is not due to absorption effects which would have the opposite

Fig. 80

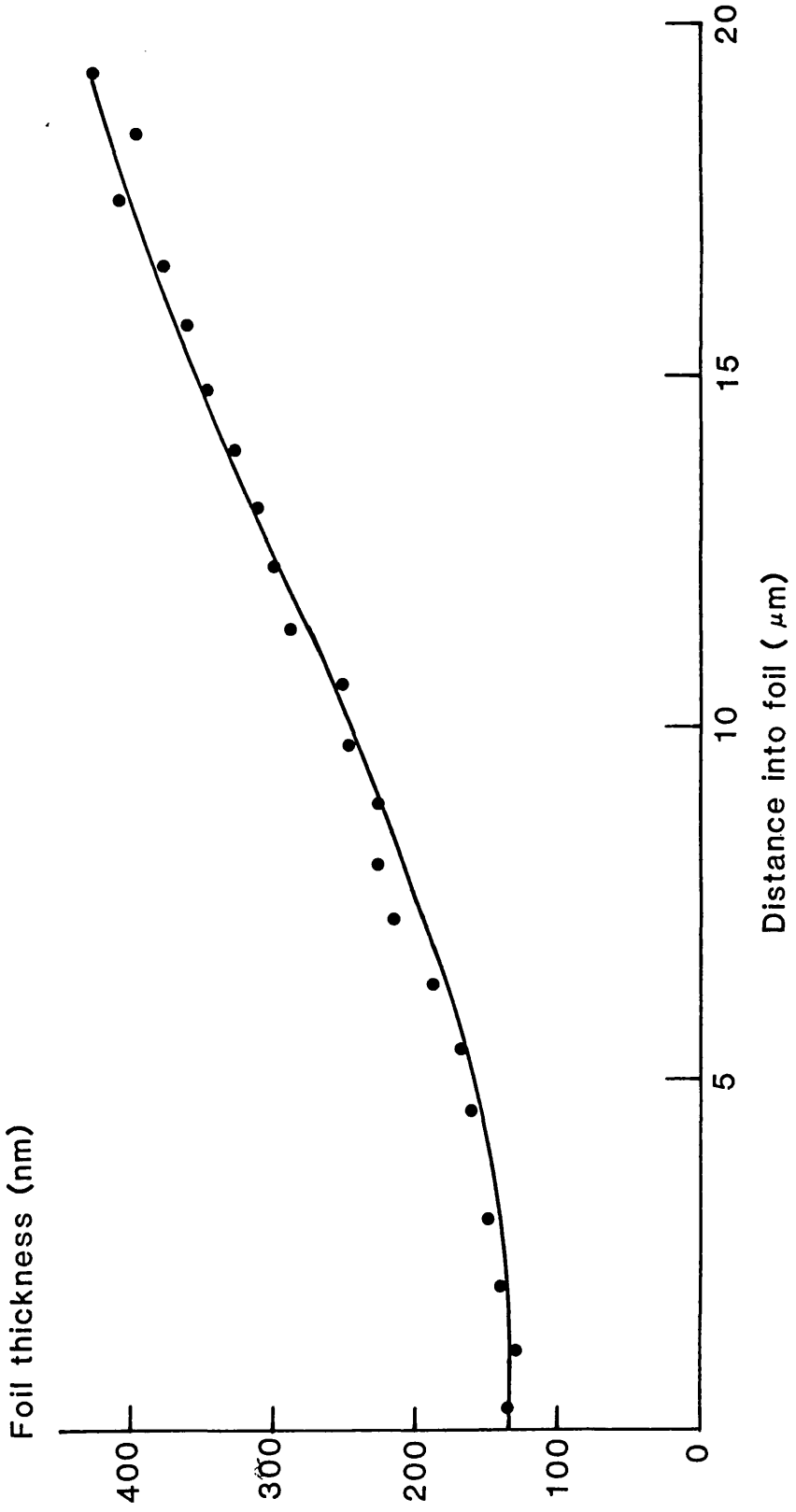

Fig. 80 Thickness profile for a Cu4%- Al alloy (P89) prepared by electropolishing.

Fig. 82 Characteristic intensity variation with foil thickness for a Cu4%- Al (P89) electropolished specimen.

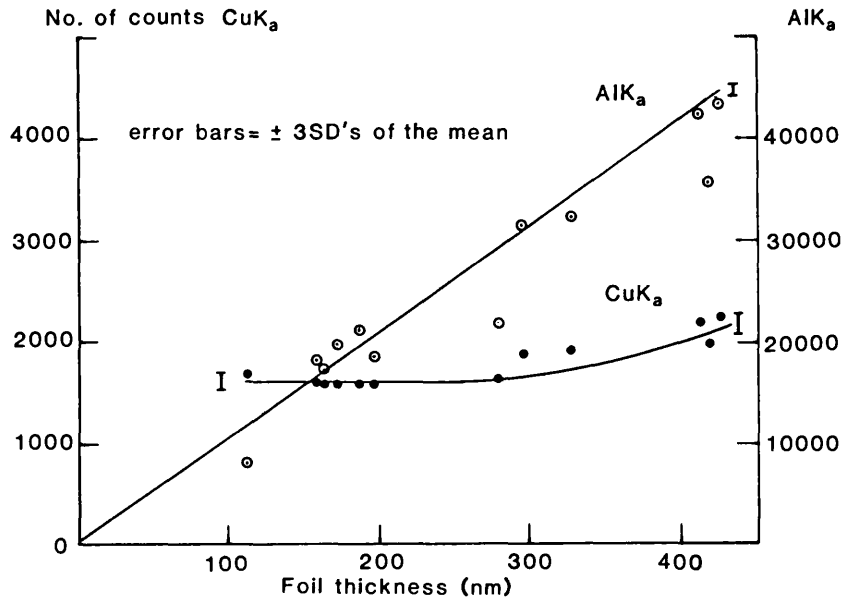

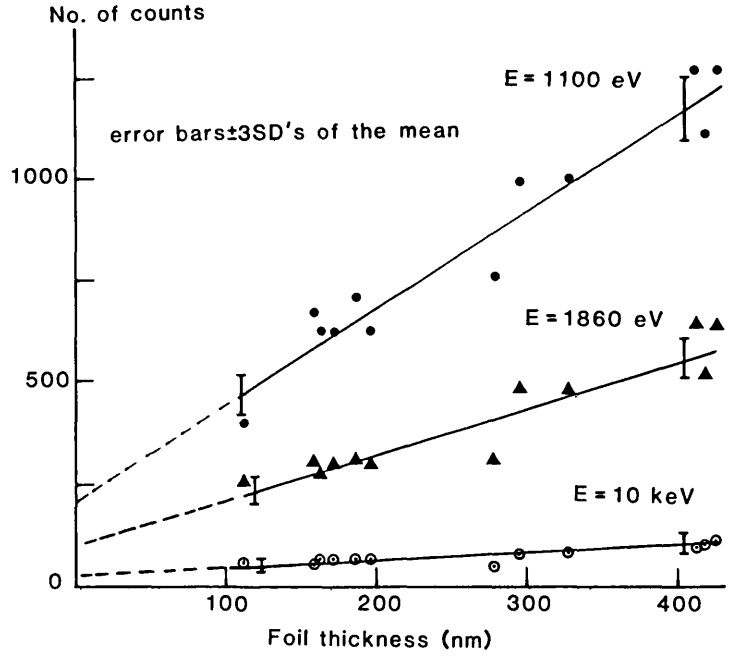

Fig. 81 Continuum intensity variation with foil thickness for a Cu4%- Al (P89) electropolished specimen.

Fig . 83

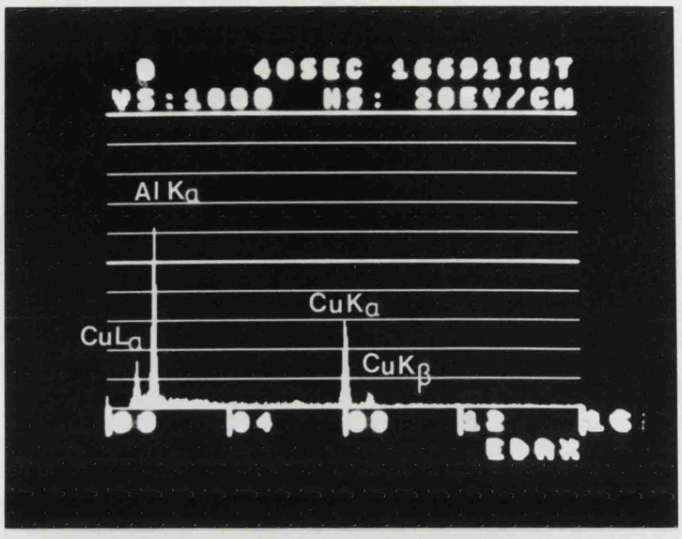

(a)

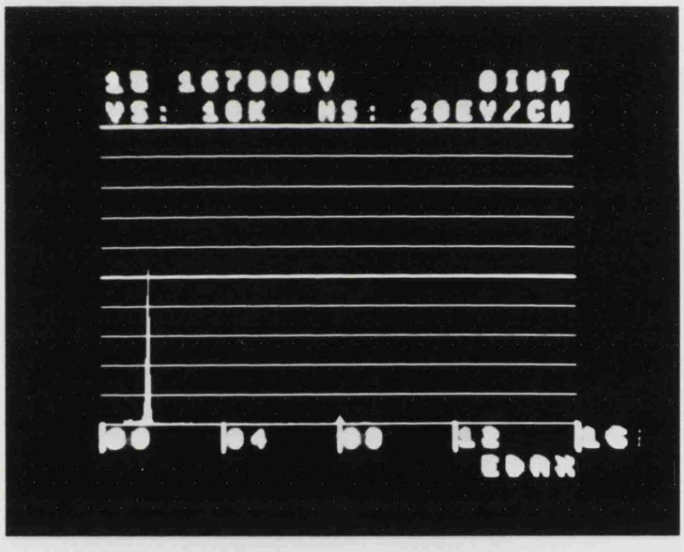

(b)

Fig. 83

X-ray spectra obtained from thin and thick regions of a Cu 4%- Al foil.

(a) Thickness in the beam direction, h = 110nm

(b) " " " " h = 320nm.

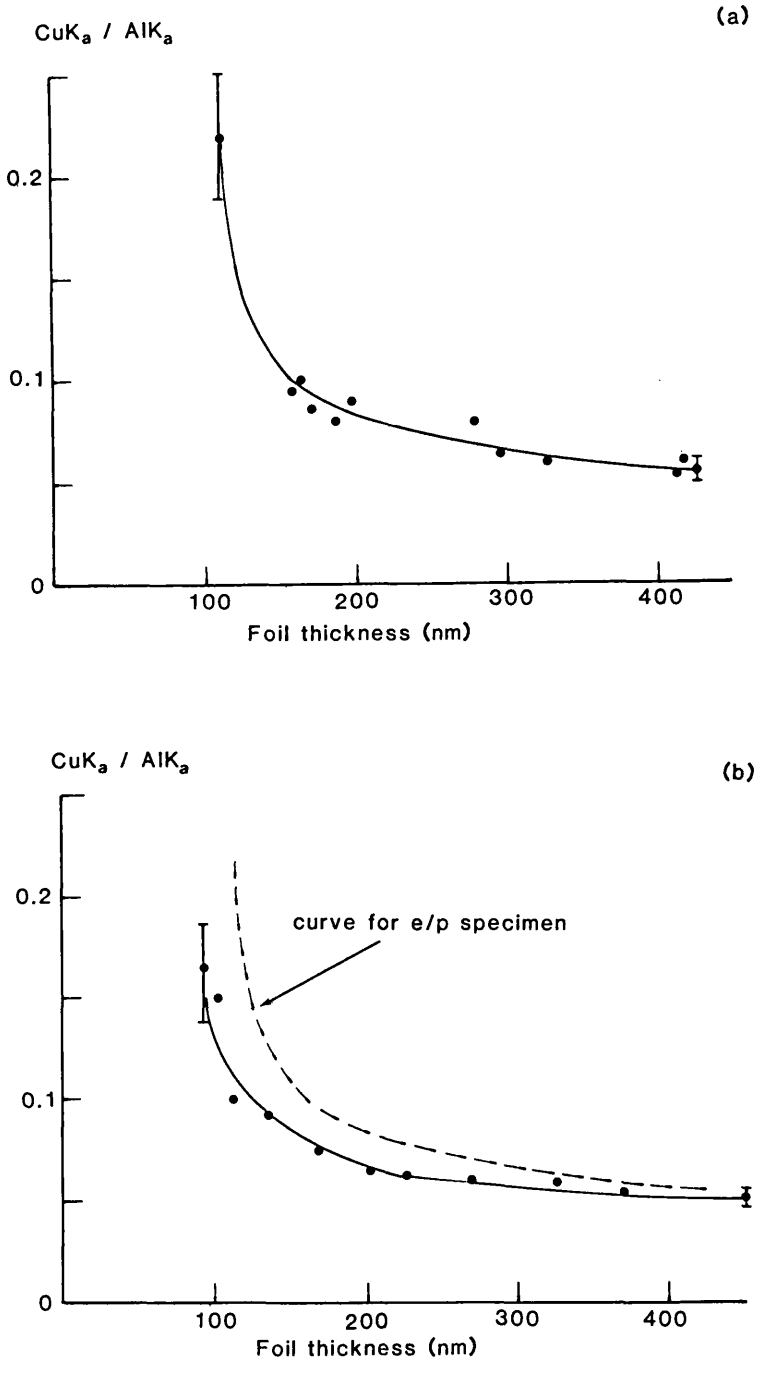

Fig. 84 CuK$_a$ / AlK$_a$ ratio vs foil thickness for Cu4%- Al (P89) specimens, (a) prepared by electropolishing (b) after ion beam "cleaning". (Error bars=±3SD's of the mean).

effect - preferential absorption of AlKα tending to raise the CuKα/AlKα ratio with increasing thickness. The changing ratio reflects a real change in the relative proportion of copper and aluminium present in the specimen. The levelling of the CuKα curve at 2000 counts and the intercept of the AlKα curve with the origin in Fig. 82 suggests that an enrichment of copper rather than a depletion of aluminium occurs.

In the study of copper specimens (section 6.5) CuKα counts of 2000 were obtained for foil thicknesses of 10 nm (see Fig. 70). The present study was conducted under the same experimental conditions and it can therefore be deduced that a thin (5nm thick) film of copper on each surface of the foil is sufficient to cause the changing ratio phenomenon.

Other workers (see section 1.2.4) have postulated the presence of thin surface films on electropolished materials. In the present study it was considered that the resultant variation in characteristic ratio s could serve as a foil thickness measuring device.

The electropolished specimen examined earlier was ion beam cleaned to test the tenacity of the surface copper film. After five hours of ion bombardment the increased size of the specimen perforation indicated that several microns of material had been removed. A repeat x-ray analysis experiment on this clean specimen revealed that the surface film of copper had been reduced but not completely eliminated. Figure 84b compares the new results with those obtained for the electropolished foil. The

results suggest that copper re-deposits on the clean surface of the foil during ion beam cleaning. A similar process appears to occur during the electropolishing routine.

Other workers investigating surface films similar in nature to those discussed above have had varying degrees of success in their removal. Pountney and Lorretto (1980) successfully removed the surface layer effects from an electropolished Cu4%-Al alloy by an ion beam sputtering process. The sputtering time required to remove the film (20 hours) indicated a surface film thickness of approximately 10nm. Thomson, Doig, Edington and Flewitt (1979) found that washing the specimen in chromic acid effectively removed the copper film from such alloys.

The main conclusions of the present investigation are four-fold. The ratio of the CuKα/AlKα intensities varies markedly with foil thicknesses in the 100-200nm range. The effect is due to a surface enriched film of copper formed during specimen production. The methods of production affects the degree of surface enrichment and the calibration of the phenomenon for use in foil thickness determinations is therefore impractical.

7. THE APPLICATION OF THE CONTAMINATION SPOT METHOD TO PRECIPITATE MEASUREMENTS IN Al-ALLOYS

The collaborating body in these studies (AUWE Portland) was most interested in assessing the effects of modifying elements on the behaviour of alloys of the Al-Cu 4% type. Smith and Scott (1979) and Love, Rae and Scott (1980) have shown that the strength of such alloys improved with minor additions of zinc, silver and magnesium to the composition. Whereas the precipitates in the basic Al-Cu 4% alloy adopted a {100} habit plane, Ag/Mg alloys showed preferential precipitation on {111} planes. The crystal structure of these precipitates is thought to be different (see Smith & Scott 1979) and it is suggested that the higher strength of such alloys is associated with a higher interfacial energy for the {111}-type precipitate.

To investigate such dependencies required knowledge of the precipitate populations lying on the {100} and {111} habit planes in these alloys. In the present study the precipitate populations of various age-hardenable alloys were calculated using the contamination spot technique to measure the thickness. This method was chosen as it measured the thickness in the beam direction, the correct parameter required to determine foil volume accurately.

7.1 Materials, specimen preparation and examination

Two alloys, one a basic Al-Cu 4% the other containing additions of silver and magnesium, were examined. The alloys were obtained from AUWE Portland in the forms of sand cast slabs. The compositions of the alloys, designated

by their cast numbers P89 and P91, are given in table 1. A third alloy, cast at Bath University and containing a higher Ag:Cu is also listed in table 1. This alloy, formed as a chill casting was identified as A1. All alloy compositions were determined by chemical analysis at AUWE.

The alloys were prepared for TEM examination using the electropolishing disc technique. The electropolishing conditions were the same as for aluminium specimens (see table 2).

Samples of P89 and P91 aged to peak hardness at 140°C and 170°C were examined in the TEM. As the peak aged material contained coherent precipitates the resultant strain fields degraded image contrast under Bragg conditions. The peripheral regions adjacent to the strain-affected zone provided the best contrast conditions for the precipitates (see Fig. 85). Having selected the most suitable area for examination, contamination spots were deposited under standardised conditions in these areas to form a grid pattern. The spacing between each spot was $\approx 3\mu m$. The specimen was then photographed at zero and 45° tilt to give the precipitate numbers and the foil thickness. An accompanying diffraction pattern provided information on the precipitation habit planes.

7.2 Examination of an Al-alloy with a high Ag:Cu ratio

It was mentioned earlier that additions of magnesium and silver caused preferential precipitation on {111} planes. In alloy P89 all precipitation occurred on {100}

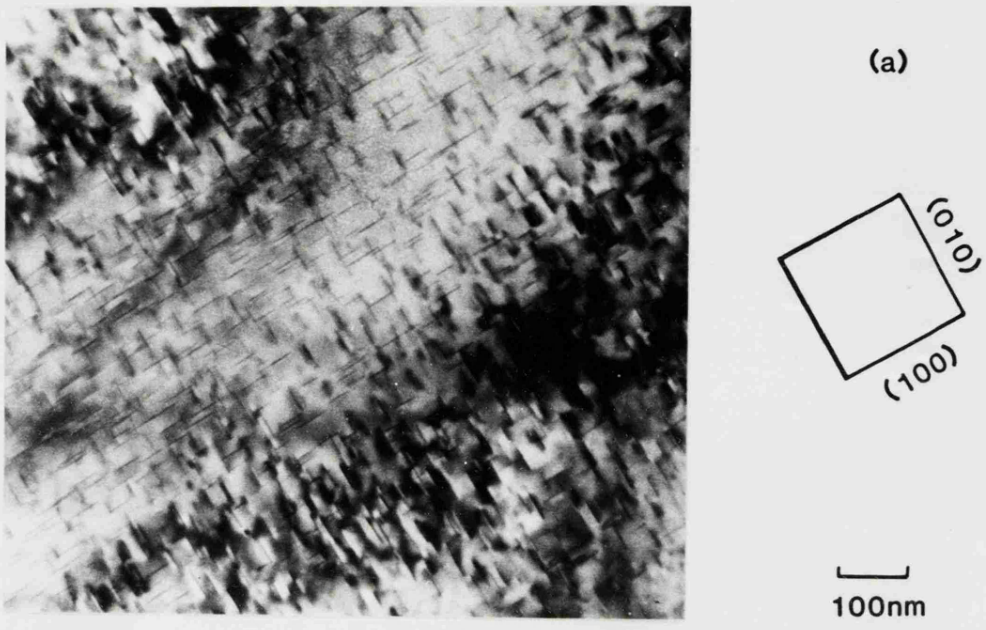

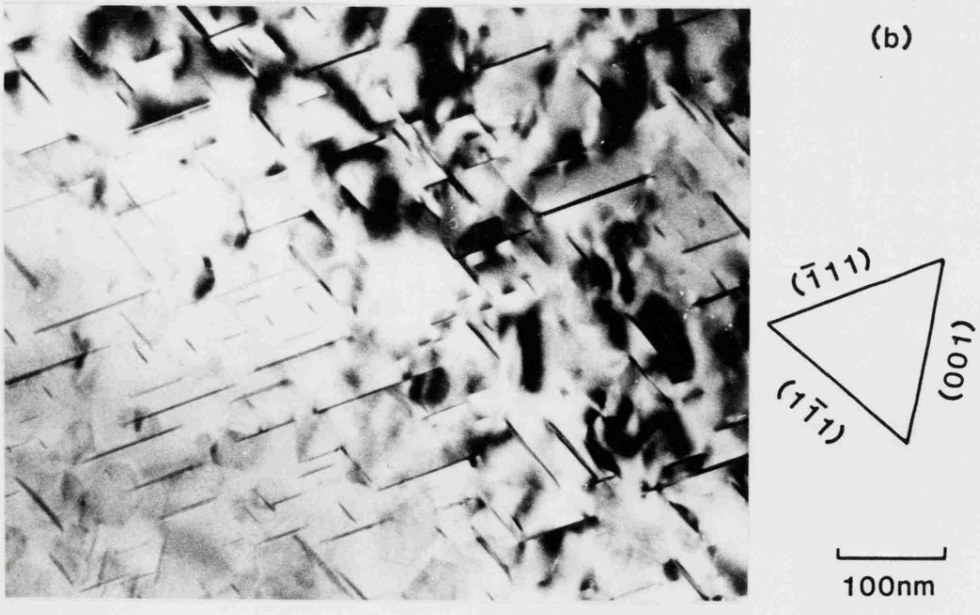

Fig. 85 Precipitation in peak aged aluminium alloys, (a) {100} type in alloy P89, (b) {111} type in alloy P91.

planes while P91 exhibited precipitation on both {100} and {111} planes. It was considered that an increased Ag/Cu ratio was responsible for this effect. This hypothesis was tested by further increasing the magnitude of this ratio and noting its effect on precipitation.

An alloy of P91 was modified to lower the copper content and raise the silver content while maintaining other elemental concentrations constant (see table 1 for alloy A1 composition).

The molten alloy was cast into a dry metal mould and upon removal was solution treated in an argon atmosphere for 44 hours at 530°C. On completing this treatment the alloy was quenched into water, sectioned into pieces and aged for various periods in an oil bath at 170°C. From hardness tests on the alloy the peak ageing time was determined. Samples were then prepared for TEM examination from this peak aged material. Conditions of electropolishing were as for aluminium (see table 2). Selected area micrographs of the precipitates were taken together with their corresponding diffraction patterns.

7.3 Results

In the alloy P89 the precipitates of the peak aged material formed exclusively on the {100} planes of the aluminium matrix. Alloy P89, with an increased silver content exhibited dual precipitation on {100} and {111} plane.

Analysis of the micrographs revealed the precise precipitate populations occupying each habit plane. On magnified prints, squares of a known size were drawn in the vicinity of the contamination spots and the number of

precipitates lying on a specific plane within were counted. These figures were then converted to precipitate population densities for the relevant habit plane by dividing by the volume of foil outlined by the square and multiplying by the appropriate number of planes - three in the case of {100} precipitates and four for {111} type.

Table 11 shows precipitate populations for the alloys P89 and P91 for different foil thicknesses and ageing temperatures. It can be seen that in some instances the precipitate population is abnormally high when measured in very thin regions of foil. The reason for this is not clear. Using uncorrected thickness values would result in a foil thickness overestimation for the reasons outlined in section 4. The effect of using such values would be the opposite of that shown in table 11; lower rather than higher population densities being expected in thin regions of foil. The possibility was considered of errors being introduced by the "top-bottom" effect (Fraser, Jones and Loretto 1977) where in the TEM mode the image was more representative of the microstructure of the bottom rather than the top regions of the foil but this effect would not be expected to cause significant errors with the foil thicknesses studied here.

An alternative simplistic approach to this problem is given in Fig. 87 which shows schematic cross-sections of foils 100nm and 200nm thick. The precipitates, which in these alloys are disc shaped and $\approx$50nm diameter, are shown as circles. It can be seen that doubling the foil thickness produces only a 67% increase in the number of precipitates, and hence a lowering of the apparent

Alloy, ageing temp. and habit plane			Uncorrected thickness, nm	Population based on uncorrected thickness	Corrected thickness, nm	Population based on corrected thickness
P89	140°C	{100}	145 188 199	2.9 2.34 1.9	97 132 141	4.35 3.33 2.68
	170°C	{100}	186 202 209 254 261 264 287	1.49 1.47 1.49 1.58 1.51 1.71 1.92	131 143 149 186 191 194 214	2.13 2.07 2.09 2.16 2.05 2.32 2.58
P91	140°C	{100}	222 273 320 357	.114 .097 .0865 .105	159 202 240 271	.158 .131 .115 .138
		{111}	273 320 357	1.0 .55 .504	202 240 271	1.35 .73 .665
	170°C	{100}	135 164	.286 .25	88.5 112	.436 .365
		{111}	135 164	1.19 .46	88.5 112	1.82 .67

Table 11. Precipitate populations ($x10^{-13} mm^{-3}$) of peak aged aluminium alloys for a range of foil thicknesses.

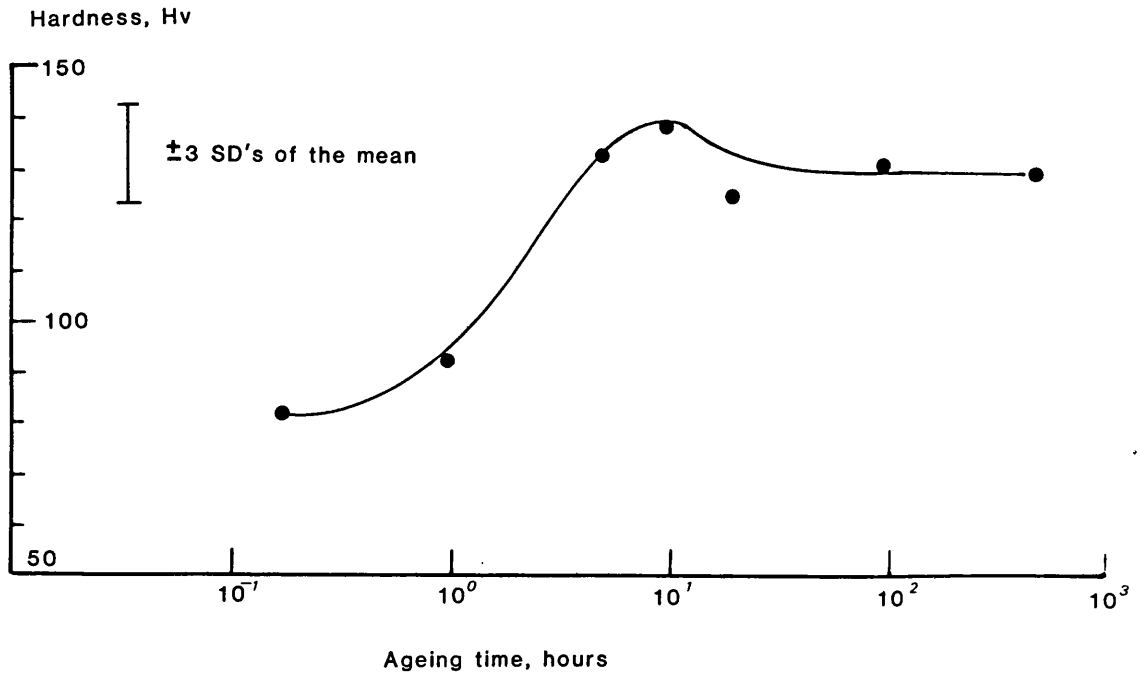

Fig. 86 Ageing characteristics of alloy A1, aged at 170 C.

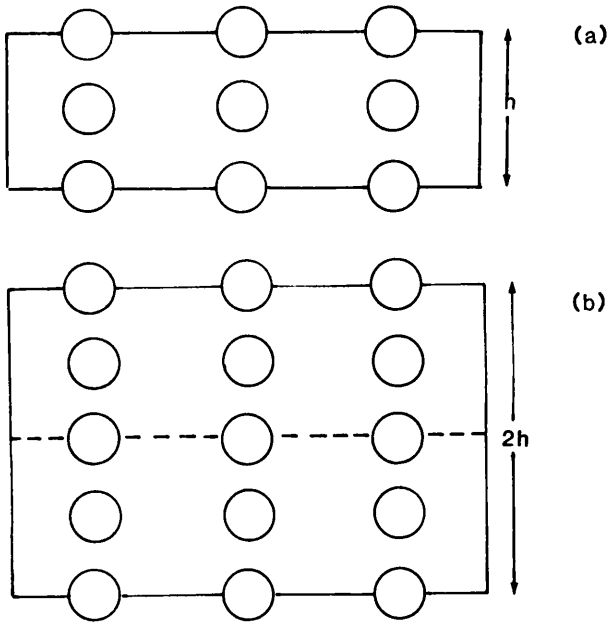

Population of (a) is 9 and of (b) is 15, ie an apparent decrease in ppt. population density accompanies increases in foil thickness.

Fig. 87 Schematic representation of precipitate population density dependence on foil thickness.

precipitate population density. In thicker regions, where foil thickness is many times greater than the precipitate diameters, this effect would be negligible.

It is concluded that more confidence may be placed in the population measurements obtained from thicker regions of foil. Although the precision is probably no better than ±25% certain trends appear evident. The precipitate populations of alloys aged at 140°C are generally higher (≈ 2x) than for those aged at 170°C. In alloy P91 ≈ 80% of the precipitates lie on {111} planes.

The ageing curve for alloy A1, with an increased silver and magnesium content is shown in Fig. 86. Peak ageing occurred in 10 hours at 170°C. No {100} type precipitation was found when peak aged specimens were examined in the TEM (Fig. 88). It is concluded that raising the level of silver and magnesium caused precipitation to occur solely on {111} planes.

A model has been proposed by Taylor, Parker and Polmear (1978) to account for the increasing tendency of {111} precipitation that occurs when small additions of silver and magnesium are made to an Al-Cu4% alloy. These workers proposed that the prior formation of Mg_3Ag on {111} matrix planes modified the precipitation sequence in Al-Cu alloys causing the copper containing phases to precipitate out on {111} rather than {100} planes.

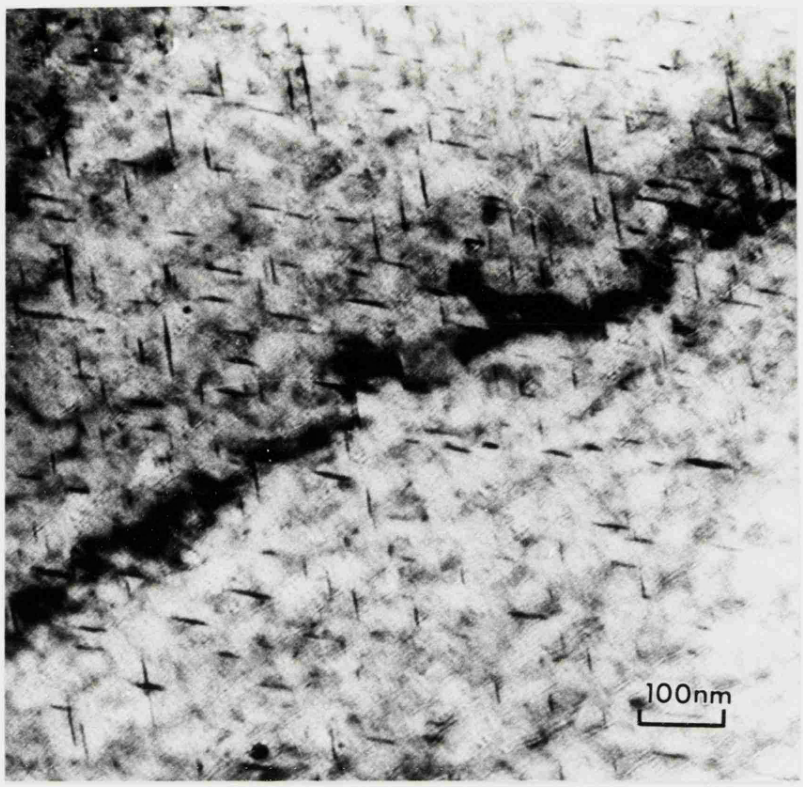

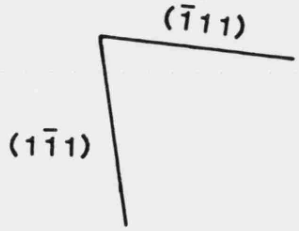

Fig. 88 {111} precipitation in peak aged alloy A1.

8. CONCLUSIONS AND FUTURE WORK

The wedge-shaped profiles of electropolished and ion-beam thinned TEM specimens dictate the use of techniques which will measure foil thickness on a local scale. The parameter required to measure defect populations in thin foils is the foil thickness in the beam direction. Such information is also needed in microanalysis studies, where the path length through the specimen of emergent x-rays is required in quantitative work.

Many methods for measuring foil thickness are unsuitable for general use. For example, those involving analysis of bend or extinction contours may be applied only to certain regions of crystalline foils, such as thin areas adjacent to the central perforation of an electropolished specimen. Furthermore, exact Bragg diffracting conditions and the extinction distance of the diffracting planes are needed to determine thickness accurately.

In the present study several methods for determining foil thickness in the beam direction were investigated. Each was considered to be applicable to a range of materials and each, save for the crystallographic technique, was capable of determining foil thickness on a local scale.

One study involved relating foil thickness to the projected widths of defects such as slip plane traces. If the foil normal and electron beam are not initially

parallel, perhaps because of foil buckling, large errors (>100%) may be introduced into foil thickness values. The crystallographic method investigated here overcame this problem and, by devising a graphical approach, fault inclination and width can be determined very accurately, to ∿ 3%. Since with the fault aligned parallel with the electron beam the metal foil thickness is equal to the fault width, the thickness estimate is also accurate to ∿3%. For stainless steel and copper slip traces were usually analysed. In aluminium, however, the persistence of such faults is less and grain boundaries were sometimes substituted in their place. For coherent defects, such as stacking faults, it was shown that under certain imaging conditions the outermost fringe contrast approached background intensity, rendering it effectively invisible and causing an underestimation of foil thickness. Dark-field and weak-beam imaging were shown to reduce such errors and imaging under different conditions, as in the tilting fault experiment, may show up any erroneous results.

The contamination spot technique is easily applied to a variety of materials over a large range of thicknesses. Its use does not depend on the presence of defects nor on diffraction phenomena and is therefore potentially useful in non-metallic and biological studies. However, the method was shown to overestimate the true metal thickness. The main cause of the overestimation was an aureole of contaminant surrounding the central spot which caused a displacement in the

apparent spot-substrate interface away from the true value. The magnitude was found to depend on the spot size and morphology and on the nature and thickness of the substrate, largest overestimates occurring in thick regions of dense materials. By optimising and standardising the conditions of specimen preparation and spot deposition the degree of overestimation was minimised and the reproducibility of the method was found to be very good. The method may be readily calibrated by a more absolute technique (for example a crystallographic method) to give values of metal thickness accurate to better than ± 10nm. Some further work suggests itself as a result of this study. At present the relationship between the degree of overestimation by the contamination spot method and the specimen mass thickness is only qualitatively known. A greater understanding of this could render experimental calibration of the technique unnecessary.

The convergent beam diffraction technique was shown to measure the actual thickness of metal in the beam direction. The method is free from any systematic errors in magnification and image contrast that can affect other techniques. When two-beam conditions were established the uncertainty in the thickness values obtained from the graphical method was better than ± 3%. In practice, however, perfect two-beam conditions are never achieved and for small deviation parameters or large interplanar spacings (i.e. low order relecting planes) multiple beam effects become pronounced. As a

consequence the linearity of the $\left(\frac{s}{n}\right)^2$ v n^{-2} curves is not guaranteed and choosing the correct curve for low order reflections can become a subjective exercise. The need to use only high order reflecting planes is therefore emphasised. Another problem with the method was the difficulty in determining the correct starting value of n_1 when the foil thickness was near to an integer multiple of the extinction distance, i.e. $t = 1\xi_g$, $2\xi_g$ etc. When using high order planes with large extinction distances this problem is not encountered in the normal range of TEM thicknesses. Further difficulties may arise due to anomalous absorption which causes displacement of the fringes in the diffracted disc relative to the $s = 0$ position. Fortunately the effect on maxima and minima is approximately equal in magnitude and opposite in sense and, by analysing both light and dark fringes, the effects may be nullified.

The convergent beam technique is generally limited to defect-free regions of crystalline material. A further stipulation is that the interplanar spacing of the operating plane be known. Thus it cannot at present be used in precipitate studies or on foils with unknown interplanar spacings. Possible future work on the determination of the effects of lattice strain on the diffracted intensity profile would be useful and could make the technique more widely applicable.

In the x-ray studies it was found that both characteristic and continuum x-radiation intensities were a function of foil thickness. The relationship was approximately linear when absorption was negligible. Individual scatter however was quite high, due mainly to small fluctuations in the specimen current. It is recommended that in future a metal standard might be used to remove ambiguity, the standard being inserted prior to analysis of the specimen in order to enable the beam current to be adjusted to give a constant x-ray count rate. The stability of the beam current could also be monitored during the course of the experiment by reference to the standard. The ratios of the characteristic and continuum x-ray intensities were insensitive to changes in specimen current, since both these intensity values are affected equally. The results for copper show that measured ratios closely follow theoretical predictions with CuLα/CuKα falling quite markedly with increasing thickness. Again, scatter on individual results is quite high and is attributed to a non-uniformly tapering foil, resulting in a non-linear relationship between x-ray path length and foil thickness. The errors in measuring foil thickness using characteristic intensities and characteristic intensity ratios are as high as 100nm. Using continuum radiation the errors are even larger due to the lower count rates and resulting higher statistical scatter.

X-ray fluorescence was not found to be significant in the thin foils, even with stainless steel where in conventional electron-probe microanalysis of bulk specimens the effects are known to be large. This is in contrast to the work of Lorimer et al (1977) but in agreement with recent results obtained by Tixier (1981). Clearly, further work needs to be done in order to resolve the disagreement.

Thin surface films were shown to be present on some foils by their effect on the ratio of characteristic lines with varying foil thickness. The level of the effect depended on the initial surface preparation which is difficult to assess quantitatively. It is possible that very thin metallic films of a known thickness could be vacuum deposited onto TEM specimens to provide a more controlled version of this phenomena. Thus, for example a thin copper film could be deposited onto aluminium foils and the resulting characteristic ratios used as a measure of thickness. A final conclusion of the x-ray study is that measured x-ray intensities (and ratios) can be sensitive to the position of the electron beam on the specimen. This is due to the fact that certain areas of the specimen are shielded from the x-ray detector by the beryllium specimen holder. Low energy x-rays such as AlKα are absorbed in this holder and it was shown that in some analysis positions complete absorption of AlKα occurred. It is therefore important to check that such an effect is not present during the analysis.

In the applied study of precipitate populations the changing modes of precipitation were quantitatively assessed using the contamination spot technique to measure the foil thickness. The results indicate that when precipitate diameters are of the same magnitude as the foil thickness, estimation of precipitate populations can be in error even if foil dimensions are accurately known.

Finally, it must be said that the variety of methods available and used for determining thin foil thickness is clear evidence that no single technique has been found universally applicable to all studies.

REFERENCES

ACKERMANN, I. (1948), Ann. Phys., 6, 19.

ALLEN, S.M., (1981), Phil.Mag.A. (1981), 43, No. 2, 325.

BELL, W.L. & THOMAS, G. (1972) Electron Microscopy and Structure of Materials, University of California Press, Berkeley. 23.

BELL, W.L. & THOMAS, G. (1969), Twenty-Seventh Annual EMSA Meeting, 158.

BENDER, B.A., WILLIAMS, D.B. & NOTIS, M.R., (1980), Journal of the American Ceramic Society, 63, No. 3-4, 149.

BENTLEY, J. & KENIK, E.A., (1976), Thirty-Fourth Annual EMSA Meeting, 426.

BLAKE, R.G., JOSTSONS, A., KELLY, P.M. & NAPIER, J.G., (1978), Phil.Mag., A, 37, 1.

CASTAING, R. & DESCAMPS, J. (1955), J.Phys.Rad., 16, 304.

CHEN, L.J. & THOMAS, G., (1974), Phys.Stat.Sol., (a), 25, 193.

CLAREBROUGH, L.M. & HEAD, A.K., (1976), Phil.Mag., 33, No.3, 557.

CLIFF, G. & LORIMER, G.W., (1972), Proc.Fifth.Eur.Cong. Electron Microsc., Manchester, Inst. of Phys.London. 140.

COCKAYNE, D.J.H., GOODMAN, P., MILLS, J.C. & MOODIE, A.F., (1967), Rev.Sci.Instrum., 38, 1097.

CROCKER, A.G. & BEVIS, M. (1964), Phys.Stat.Sol., 6, 151.

CUNDY, S.L., Ph.D.Thesis, Cambridge (1967); through Rossouw & Whelan (1978).

DOIG, P. & FLEWITT, P.E.J., (1977), J.Microscopy, 110, 107.

DRAZIN, M.P. & OTTE, H.M., (1963), Phys.Stat.Sol., 3, 824.

EADES, J.A. & RACKHAM, G.M. (1977), Optik, 47, 227.

EASTERLING, K.E., (1977), J.Mat.Sci., 12, 857.

EDINGTON, J.W., (1975), Practical Electron Microscopy in Materials Science, Monograph Three. The Macmillan Press Ltd., London.

EGERTON, R.F., (1975), Phil.Mag., 31, 199. Through Rossouw & Whelan 1978.

FORMBY, C.L., (1966), Phil.Mag., 13, 621.

FRAZER, H.L., JONES, I.P. & LORETTO, M.H., (1977), Phil. Mag., 35, 159.

GOLDSTEIN, J.I. and WILLIAMS, D.B., (1977), Scanning Electron Microscopy, 1, 651.

GOLDSTEIN, J.I. & WILLIAMS, D.B., (1978), Scanning Electron Microscopy, 1, 427.

GOODMAN, P., (1980), Scanning Electron Microscopy, 53.

GOODMAN, P. & LEHMPFUHL, G., (1967), Acta.Cryst., 22 14.

HALL, E.L. & VANDER SANDE, J.B., (1975), Phil.Mag., 32, 1289.

HALL, T.A., (1971), Physical Techniques in Biological Research, 2nd Ed., editor G.Oster, N.Y. Academic Press, 1A, 157.

HEIMENDAHL, VON, M. (1964), J.Appl.Phys., 35, No. 2, 457.

HEIMENDAHL, VON, M. (1973), Micron, 4, 111.

HEINRICH, K.F.J., (1966), The Electron Microprobe. Edited by T.D.McKinley, K.F.J.Heinrich & D.B.Wittry. Wiley & Sons, N.Y. 1966.

HIRSCH, P.B., HOWIE, A., NICHOLSON, R.B., PASHLEY, D.W. & WHELAN, M.J., (1965), Electron Microscopy of Thin Crystals, Butterworths, London.

HIRSCH, P.B. & HUMPHRIES, C.J., (1968), Proc.IV. Europ. Regional Conf. Electron Microscopy., Rome 1, 49.

HOWIE, A., (1963), Proc.Roy.Soc., A271 268, through Rossouw and Whelan (1978).

HOWIE, A. &BASINSKI, Z.S., (1968), Phil.Mag., 17, 1039.

JACOBS, M.H. & BABOROVSKA, MRS. J., (1972), Proc.Fifth. Eur.Cong. Electron Microsc., Manchester, Inst.Phys.London, 136.

JONES, I.P. & LORETTO, M.H., (1981), Journal of Microscopy, 124, pt. 1, 3.

JOY, D.C. & MAHER, D.M., (1975), 33rd Ann.Proc.EMSA., Editor G.W.Bailey, Las Vegas, Nevada, 242.

KAWANISHI, H., SHIOZAWA, S., ISHINO, S & MISHIMA, Y., (1973), J.Inst. Metals., 101, 93.

KELLY, P.M., JOSTSONS, A., BLAKE, R.G. & NAPIER, J.G., (1975a), Phys.Stat.Sol., (a), 31, 771.

KELLY, P.M., (1975b), Phys.Stat.Sol., (a), 32, 529.

KRAMERS, H.A., (1923), Phil.Mag., 46 836.

LOVE, G., RAE, D.A. & SCOTT, V.D., (1980), Electron Microscopy, 1, 208.

LEROUX, J., (1961), Adv.X-ray Anal., 5, 153.

LORIMER, G.W., CLIFF, G. & CLARK, J.N. (1976), Developments in Electron Microscopy and Analysis, Ed. J.A.Venables, 153.

LORIMER, G.W., AL-SALMAN, S.A. & CLIFF, G., (1977), EMAG 1977, Inst.Phys.Conf.Ser. No. 36, 369.

MacGILLAVRY, C.H., (1940), Physica, 7, No. 4 329.

MEDVED, D.B. & POPPA, H., (1962), J.Appl.Phys., 33 1759.

MORRIS, P.L., (1979), Alcan Labs. Ltd., Banbury, Tech. File R-79/24.

MORRIS, P.L., DAVIES, N.C., TREVERTON, J.A., (1977), EMAG 1977, Ed., D.Misell, Inst.Phys.Conf.Ser. No 36, 377.

MORRIS, P.L. & LAMB, H.J., (1978), J.Phys.D.App.Phys., 11, L75. (and reply by K.J.Sawley ibid L76).

NIEDRIG, N., (1978), Scanning Electron Microscopy, 1, 841, SEM Inc., AMF O'Hare, 1L 60666, USA.

NICHOLSON, W.A.P., ROBERTSON, B.W. & CHAPMAN, J.N. (1977), EMAG 1977, Ed. D.Misell, Inst. Phys. Conf. Ser. No. 36, 373.

NOCKOLDS, C., NASIR, M.J., CLIFF, G. & LORIMER, G.W., (1980) EMAG 1979, Ed., T.Mulvey, Inst.Phys.Conf. Ser. No. 52, 417.

OTTE, H.M., DASH, J. & SCHAAKE, H.F., (1964), Phys.Stat. Sol. 5, 527.

PHILIBERT, J. & TIXIER, R., (1975), Physical Aspects of Electron Microscopy & Microbeam Analysis. Eds. B.M.Siegal & D.R. Beaman. Wiley 1975, 333.

POUNTNEY, J.M. & LORETTO, M.H., (1980), Electron Microscopy, 3, 180.

RADI, G., (1968), Z.Phys., 213, 244, through Rossouw & Whelan, (1978).

RAE, D.A., SCOTT, V.D. & LOVE, G., (1981), Quantitative Microanalysis with High Spatial Resolution, UMIST Manchester, 57.

REED, S.J.B. (1975), Electron Microprobe Analysis, Cambridge Univ. Press.

ROSSOUW, C.J. & WHELAN, M.J., (1978), Phys.Stat.Sol. (a) 45, 277.

RUSS, J.C., (1977), X-ray Spectrometry, 6, No. 1, 37.

SABATTIER, in Introduction to Photographic Theory, (1980), B.H.Carroll, John Wiley & Sons. N.Y.

SALTER, W.J.M., (1970), A Manual of Quantitative Electron Probe Microanalysis, Structural Publications Ltd., London.

SAWLEY, K.J., CLIFF, G. & HOWARTH, C.W., (1977), J.Phys. D., 10, 1883.

SELLER, J.R. & COWLEY, J.M., (1973), Proc. 6th SEM Symposium, Ed. O.Johari & I.Corvin, 244.

SIEMS, R., DELAVIGNETTE, P. & AMELINCKX, S. (1962), Phys. Stat. Sol., 2, 421.

SKALICKY, P. & DEGISCHER, P., (1968), Z.Angew. Phys., 25, 217.

SMITH, A.F. & SCOTT, V.D., (1979), Final report for M.O.D., REFERENCE ER3/9/4/2112/029 AUWE.

STATHAM, P.J. & BALL, M.D., (1980). Proc.Annu.Conf.Microbeam Anal. Soc. 165.

TAYLOR, J.A., PARKER, B.A. & POLMEAR, I.J., (1978), Metal. Sci., 12, 478.

THOMAS, G. & GORINGE, M.J., (1976), Transmission Electron Microscopy of Materials. John Wiley & Sons, N.Y.

THOMPSON, M.N. & CHEN, C.W., (1979), Philips Bulletin EM112 - 1979/1.

THOMPSON, M.N., DOIG, P. EDINGTON, J.W. & FLEWITT, P.E.J., (1977), Phil. Mag. 35, 1537.

TIXIER, R., THOMAS, B. and BOURGEOT, J., (1981). Quantitative microanalysis with High Spatial Resolution, UMIST, Manchester, 15.

TOLANSKY, S., (1948), Multiple-Beam Interferometry of Surfaces and Films. Oxford Univ. Press. London 187.

TOLANSKY, S., (1955), An Introduction to Interferometry. Longmans Green & Co Ltd., London 223.

TOLANSKY, S., (1960), Surface Microtopography. Interscience Publ., London, 296.

VERNON, W.H., WORMWELL, F. & NURSE, T.J., (1939), Journal of the Chemical Society, 621.

VERNON, W.H., WORMWELL, F. & NURSE, T.J., (1944). J. Iron & Steel Inst., (London), 150, No. 2, 81.

VIGEHOLM, B. & LINDBO, J., (1969), Trans.Met.Soc.AIME. 245, 883.

VINGSBO, O., (1970), Septième Congrès International de Microscopie Électronique, Grenoble, 325.

WALL, J.S., (1980), Scanning Electron Microscopy, SEM Inc., AMF O'Hare (Chicago), IL 60666.

WENTZEL, G., (1927), Zeit.Phys., 43, 524.

ZALUZEC, N.J. & FRASER, H.L., (1978), Analytical Electron Microscopy, Report of a specialist Workshop, Cornell Univ. Press., N.Y.

GRUNDY, P.J. & JONES, G.A., (1976), Electron Microscopy in the Study of Materials, London, Arnold 18.